Coded Illumination for Multidimensional Quantitative Phase Imaging

Michael Chen
Laura Waller, Ed.

Electrical Engineering and Computer Sciences
University of California at Berkeley

Technical Report No. UCB/EECS-2020-37
http://www2.eecs.berkeley.edu/Pubs/TechRpts/2020/EECS-2020-37.html

May 1, 2020

Coded Illumination for Multidimensional Quantitative Phase Microscopy

by

Michael Chen

A dissertation submitted in partial satisfaction of the

requirements for the degree of

Doctor of Philosophy

in

Engineering – Electrical Engineering and Computer Sciences

in the

Graduate Division

of the

University of California, Berkeley

Committee in charge:

Ted Van Duzer Associate Professor Laura Waller, Chair
Associate Professor Shimon Michael Lustig
Associate Professor Xavier Darzacq

Spring 2019

Coded Illumination for Multidimensional Quantitative Phase Microscopy

Abstract

Coded Illumination for Multidimensional Quantitative Phase Imaging

by

Michael Chen

Doctor of Philosophy in Electrical Engineering and Computer Sciences

University of California, Berkeley

Ted Van Duzer Associate Professor Laura Waller, Chair

Phase contrast microscopy reveals transparent objects under optical microscopes, and has been widely used for biomedical imaging. Combining specially-designed optics and computational post-processing of the raw acquisitions, quantitative phase imaging (QPI) can convert qualitative phase contrast into physical quantities, such as optical phase delay or refractive index (RI) of the object. A common way to achieve QPI is by creating interference between the scattered light from the object and a reference wave, using coherent illumination. However, the method suffers from low resolution and strong speckle noise, and it is difficult to implement interferometry in off-the-shelf microscopes. In this work, we develop QPI methods for commercial microscopes, with coded illumination. Using a programmable light source (*e.g.* an LED array) that generates partially coherent illumination, many multidimensional QPI techniques can be implemented on a commercially-available microscope without the drawbacks mentioned above. First, differential phase contrast (DPC) microscopy using wavelength-multiplexing is presented, which achieves real-time QPI up to the incoherent resolution limit. Second, quantitative phase and system aberrations are simultaneously encoded in the measurements by alternating between spatially coherent and spatially partial coherent illumination. Absorption and phase of the object, as well as the spatially varying aberrations, can then be resolved computationally. Third, a through-focus DPC microscopy is proposed in order to extend QPI to 3D. The 3D RI of the object is recovered after performing a 3D deconvolution. Finally, most of the existing 3D QPI methods, including 3D DPC, work under the weakly scattering assumption. Hence, they fail to reconstruct accurate RI when multiply scattered light dominates in the captured data. To mitigate artifacts and obtain accurate information of multiple-scattering objects, a new light scattering model is introduced along with an algorithm that solves the non-linear phase retrieval problem. The multiple-scattering model outperforms the traditional weakly scattering models while requiring similar computation cost. As a result, high resolution Giga-voxel 3D phase imaging with multiple-scattering objects is achieved.

For my grandparents, Ze Chien Wu and Jia Lin Wang

Contents

List of Figures

Acknowledgments

It has been a wonderful journey since the start date of my PhD program five years ago. I feel lucky to be a member in the Waller Lab, where I have accomplished many cool projects. Without all the help from people I met along my academic career, none of these works would have been possible. First, I would like to thank my advisor, Prof. Laura Waller, who led me into the field of computational imaging. She gave me a lot of freedom to explore potential research topics, and has always encouraged me to challenge myself upon new opportunities. I learned many important things under her constructive guidance and the awesome lab environment she built. I enjoyed having great conversations with my Qual committees, Prof. David Attwood, Prof. Shimon Michael Lustig, and Prof. Xavier Darzacq, and appreciate their suggestions that pointed me toward a right direction. Especially, I am grateful to Miki for having me as a GSI of EE123, in which I gained many new experiences and was inspired by the passion he has about everything. I would also like to thank all the members, visiting scholars and alumni from the Waller Lab. In particular, Prof. Ziji Liu and Prof. Lei Tian prepared me to get my hands dirty on computational microscopy, and Jingshan Zhong taught me how to do optimization. My awesome peers, Li-Hao Yeh and Nick Antipa, surprised me so many times with their cool ideas and showed me how research can be done in different ways. I hit the jackpot by meeting Zachary F. Phillips, with whom we figured out multiple projects, won a fellowship, and founded a startup to help out research organizations around the world. It was exciting to work with my other co-authors and collaborators at Berkeley, including Hsiou-Yuan Liu, Emrah Bostan, Shwetadwip Chowdhury, David Ren, Regina Eckert, Michael Kellman, and Nicole Repina. My PhD study wouldn't be as productive without their supports. Although it didn't become my main research focus, I acknowledge Stefano Marchesini and Dula Parkinson for useful discussions and allowed me to try out computational imaging methods with hard X-rays using the Advanced Light Source facility. I genuinely thank Kristina Monakhova, Henry Pinkard, and Gautam Gunjala for proofreading my dissertation and providing feedback.

Prof. Yi-Hsin Lin and Prof. Chyong-Hua Chen had great influences on my early research career, and encouraged me to apply for a PhD program. I would also like to credit my previous labmate Hung-Shan Chen, who is always an amazing friend and shared his spirit of entrepreneurship.

All of the great experiences I had at Berkeley wouldn't happen without my loving family. As an only child, I am so lucky to have all my cousins accompany every stage in my life. They play many roles from my perspective, such as instructors, friends and cheerleaders, and always get my back. At the same time, I am thankful that my uncles and aunts view me as their own son and support my decisions. My mom, Yu-Chang Wu, is the real wonder woman in my world. I sincerely appreciate her selfless efforts and countless times spent on me, and enjoyed every moment we shared laughs and tears together. Finally, I would like to thank my wife, Kan-Yun Tu, for being my best partner. She treats my life as important as hers, and has always been taking care of me. Now, I am ready to start the next chapter in our lives and looking forward to the unknown ahead of us.

Chapter 1

Introduction

1.1 Optical Microscopy

Optical microscopes have been used for centuries to explore features at resolutions near the wavelength of the light scattered by the objects. Nowadays, people rely on these tools in many applications, such as wafer metrology and inspection in semiconductor industry, phase contrast and fluorescence microscopy for biological research, and diseases diagnosis with histology. Due to the diffraction of light and the finite wavelength (hundreds of nanometers), optical microscopy has limited contrast, resolution and depth-of-field (DoF), which prevent us from directly perceiving complete information of the sample. However, it is possible to manipulate the contrast, break the diffraction limit and achieve multidimensional imaging by modifying the imaging system and digitally processing the acquired measurements. By adding a phase mask or installing polarization optics, Zernike phase contrast (PhC) [1] and differential interference contrast (DIC) [2] microscopy convert the phase delay into intensity contrast, which is extremely useful when imaging transparent objects. To resolve features smaller than the diffraction limit, super-resolution fluorescence imaging techniques (*i.e.* PALM [3, 4], STORM [5], and SIM [6]) recover high frequency content of targeted objects via image processing. Light field microscopy [7] uses a microlens array to encode light signal outside the original DoF, and achieves 3D imaging computationally from single 2D capture. The above examples show how computational imaging, the image restoration framework that jointly designs the optics and post-processing algorithms, enables applications that couldn't be realized by tweaking hardware or software alone. Sharing the same spirit, this dissertation provides several practical computational microscopy methods to reveal multidimensional quantitative phase information of broad types of objects.

Although the quality of optical components have drastically improved over time, due to improved materials and optical designs, the basic design of microscope systems remains similar to the original, as shown in Fig. 1.1. An optical microscope consists of a light source, illumination path, objective lens, and magnifying optical system, in that order. This generic design is a natural result of the physics of light scattering and wave propagation. In

order to further improve the image quality or enable new capabilities on a microscope, it is important to understand the theory behind the image formation process. In the following subsections, we separate the imaging process into two parts: interactions with the sample (light scattering), and imaging system components. We describe mathematically the propagation of light from the source, through the sample, to the image plane at the end of the microscope. This work focuses on partially coherent imaging, which uses a different image formation model than incoherent imaging (*e.g. fluorescence microscopy*).

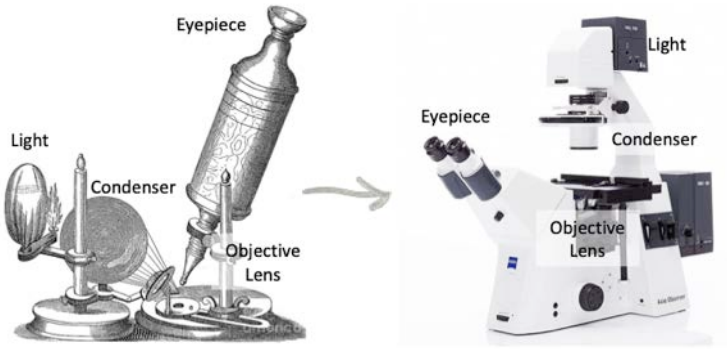

Figure 1.1: Evolution of optical microscopes since 1600s. (Left) Robert Hook's microscope [8]. (Right) Modern ZEISS Axio Observer 3 inverted microscope.

Light scattering

When light encounters change of refractive index (RI) in space, diffraction and reflection phenomena result in light scattering from its original propagation direction. The physical model of light scattering below helps us understand how light interact with an arbitrary 3D object. Based on scalar wave theory, any coherent steady-state electromagnetic field obeys the Helmholtz equation [9]. In an environment with uniform background RI, propagation of the incident field ($\boldsymbol{U}_{\text{in}}$) in free-space is described by a homogeneous Helmholtz equation:

$$\nabla^2 \boldsymbol{U}_{\text{in}}(\boldsymbol{r}) + k_o^2 n_{\text{b}}^2 \boldsymbol{U}_{\text{in}}(\boldsymbol{r}) = 0, \tag{1.1}$$

where ∇^2 is the Laplacian operator, $\boldsymbol{r}$ represents the 3D spatial coordinates, $k_o = \frac{2\pi}{\lambda}$ is the wave number, λ is the wavelength of the incident field, and n_{b} is a constant background RI of the homogeneous medium distributed in the 3D space. When there exists an object with spatially-varying RI, $\boldsymbol{n}(\boldsymbol{r})$, as shown in Fig. 1.2, perturbation of the incident field within the object causes scattered light in all direction and the total complex field, $\boldsymbol{U}_{\text{tot}}$, in 3D satisfies the following equation:

$$\nabla^2 \boldsymbol{U}_{\text{tot}}(\boldsymbol{r}) + k_o^2 \boldsymbol{n}^2(\boldsymbol{r}) \boldsymbol{U}_{\text{tot}}(\boldsymbol{r}) = 0. \tag{1.2}$$

To solve this differential equation, we move the second term in Eq. (1.2) to the right hand side of the equation, add a common term, $k_o^2 n_{\text{b}}^2 \boldsymbol{U}_{\text{tot}}$, on both sides, and subtract Eq. (1.1).

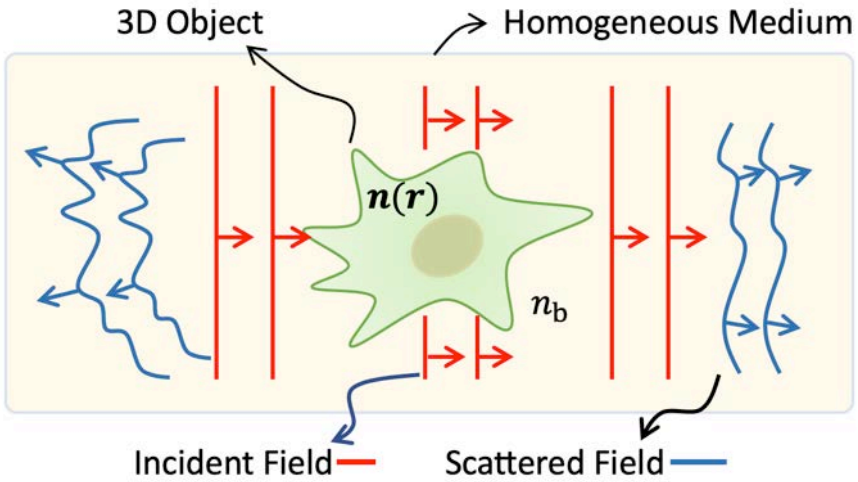

Figure 1.2: Illustration of 3D light scattering. Light is scattered in all directions by an object with an inhomogeneous refractive index (RI) distribution.

As a result, the reorganized formula becomes an inhomogeneous Helmholtz equation:

$$\nabla^2 \boldsymbol{U}_{\text{scat}}(\boldsymbol{r}) + k_o^2 n_{\text{b}}^2 \boldsymbol{U}_{\text{scat}}(\boldsymbol{r}) = \boldsymbol{V}(\boldsymbol{r}) \boldsymbol{U}_{\text{tot}}(\boldsymbol{r}), \tag{1.3}$$

where $\boldsymbol{U}_{\text{scat}}$ denotes the field scattered by the object under the coherent incident field and $\boldsymbol{V} = k_o^2 \left(n_{\text{b}}^2 - \boldsymbol{n}^2\right)$ is the scattering potential. From Eq. (1.3), the product of scattering potential and total field serve as multiple coherent contrast sources that emit the scattered field from the object. Each point source generates a spherical wave, $\boldsymbol{G}(\boldsymbol{r}) = -e^{\mathrm{i}k_o n_{\text{b}} \|\boldsymbol{r}\|_2} / (4\pi \|\boldsymbol{r}\|_2)$, which is the solution (Green's function) to a special inhomogeneous Helmholtz equation:

$$\nabla^2 \boldsymbol{G}(\boldsymbol{r}) + k_o^2 n_{\text{b}}^2 \boldsymbol{G}(\boldsymbol{r}) = \boldsymbol{\delta}(\boldsymbol{r}). \tag{1.4}$$

Therefore, the convolution result between those contrast sources and the Green's function gives rise to the scattered field. With the definitions of 3D convolution operator $\otimes_{\text{3D}}$, the total field can be written as the solution of the Lippmann-Schwinger equation [10]:

$$\boldsymbol{U}_{\text{tot}}(\boldsymbol{r}) = \boldsymbol{U}_{\text{in}}(\boldsymbol{r}) + \boldsymbol{U}_{\text{scat}}(\boldsymbol{r}) = \boldsymbol{U}_{\text{in}}(\boldsymbol{r}) + \boldsymbol{G}(\boldsymbol{r}) \otimes_{\text{3D}} \Big(\boldsymbol{V}(\boldsymbol{r}) \boldsymbol{U}_{\text{tot}}(\boldsymbol{r}) \Big). \tag{1.5}$$

In consequence, the time-independent total field is an interference result between the incident field and the scattered field, and it is non-linearly related to the 3D object represented by the scattering potential. If the incident field is composed of multiple mutually temporally or spatially incoherent modes, applying Eq. (1.5) on each mode independently extends the light scattering model to the partially coherent regime.

Several weakly scattering assumptions can be made to construct linear relationships between the scattering potential and measurable properties of the total field. For example,

simplified light scattering models have been derived based on the 1st Born (single scattering) and Rytov (smoothly varying phase) approximations [11]:

$$\boldsymbol{U}_{\text{tot}}^{\text{1st Born}}(\boldsymbol{r}) = \boldsymbol{U}_{\text{in}}(\boldsymbol{r}) + \boldsymbol{G}(\boldsymbol{r}) \otimes_{\text{3D}} \Big(\boldsymbol{V}(\boldsymbol{r})\boldsymbol{U}_{\text{in}}(\boldsymbol{r})\Big), \text{ and} \tag{1.6}$$

$$\boldsymbol{\Phi}_{\text{tot}}^{\text{Rytov}}(\boldsymbol{r}) = \boldsymbol{G}(\boldsymbol{r}) \otimes_{\text{3D}} \Big(\boldsymbol{V}(\boldsymbol{r})\boldsymbol{U}_{\text{in}}(\boldsymbol{r})\Big), \tag{1.7}$$

where $\boldsymbol{\Phi}_{\text{tot}}^{\text{Rytov}}$ is the complex phase, $\boldsymbol{U}_{\text{in}} \ln(\boldsymbol{U}_{\text{tot}}^{\text{Rytov}}/\boldsymbol{U}_{\text{in}})$. Although weakly scattering models make the inverse problems (Sec. 1.3) more tractable, they fail to provide an accurate scattered field when imaging multiple-scattering objects. In this work, we aim to efficiently account for the multiple-scattering effects while retaining computational efficiency, by adopting scattering models for scenarios between Eq. (1.5) and Eq. (1.6). Detailed discussion and implementation can be found in Chapter 5.

Optical microscope imaging system model

Optical microscopes include two composite convex lenses (the objective lens and the tube lens) and a pupil aperture. The two lenses are separated by a distance that equals the sum of their focal lengths. In consequence, a $4f$ imaging condition is satisfied between the front focal plane (FFP) of the objective lens and the back focal plane (BFP) of the tube lens, where FFP (or BFP) is the plane one focal length in front of (or behind) the lens. With a pupil between the lenses, the imaging system magnifies the object field and achieves a spatially-invariant resolution across the field-of-view (FoV), as shown in Fig. 1.3.

To analyze the magnification and resolution analytically, Fourier optics can be applied. A convex lens optically generates the 2D spatial Fourier transform of the complex field at FFP and projects the output on the BFP [9]. Mathematically, the transformation can be written as [12]:

$$\boldsymbol{U}_{\text{BFP}}(\boldsymbol{\rho}_{\text{BFP}}) \approx \chi \iint \boldsymbol{U}_{\text{FFP}}(\boldsymbol{\rho}_{\text{FFP}}) e^{-\mathrm{i}\frac{2\pi n_{\text{b}}}{\lambda R}\boldsymbol{\rho}_{\text{BFP}}\cdot\boldsymbol{\rho}_{\text{FFP}}} \mathrm{d}^2\boldsymbol{\rho}_{\text{FFP}} = \chi\mathcal{F}\{\boldsymbol{U}_{\text{FFP}}(\boldsymbol{\rho}_{\text{FFP}})\}|_{\boldsymbol{u}=\frac{n_{\text{b}}\boldsymbol{\rho}_{\text{BFP}}}{\lambda R}}, \tag{1.8}$$

where $\boldsymbol{U}_{\text{FFP}}$ and $\boldsymbol{U}_{\text{BFP}}$ are coherent complex fields at the FFP and BFP, respectively. $\boldsymbol{\rho}_{\text{FFP}}$ and $\boldsymbol{\rho}_{\text{BFP}}$ are 2D spatial coordinates at the FFP and BFP, respectively. $\mathcal{F}\{\cdot\}$ denotes Fourier transform operator, $\boldsymbol{u}$ is 2D spatial frequency coordinate, χ is a complex scalar, and R is the radial propagating distance from the FFP of the objective lens (or tube lens) to the objective lens (or tube lens). Note that the spatial frequency spectrum of the input field is mapped to the scaled spatial coordinates at the objective's BFP with a scaling factor $\frac{\lambda R}{n_{\text{b}}}$.

When imaging an object under the microscope, *non-evanescent* forward scattering components [9, 11], $\boldsymbol{U}_{\text{object}}$, of the total field in Eq. (1.5) propagates through the microscope and forms the imaged field, $\boldsymbol{U}_{\text{image}}$. Using Eq. (1.8), the $4f$ system equivalently performs a Fourier transform twice on the object field with a low-pass filter determined by the pupil, $\boldsymbol{P}$.

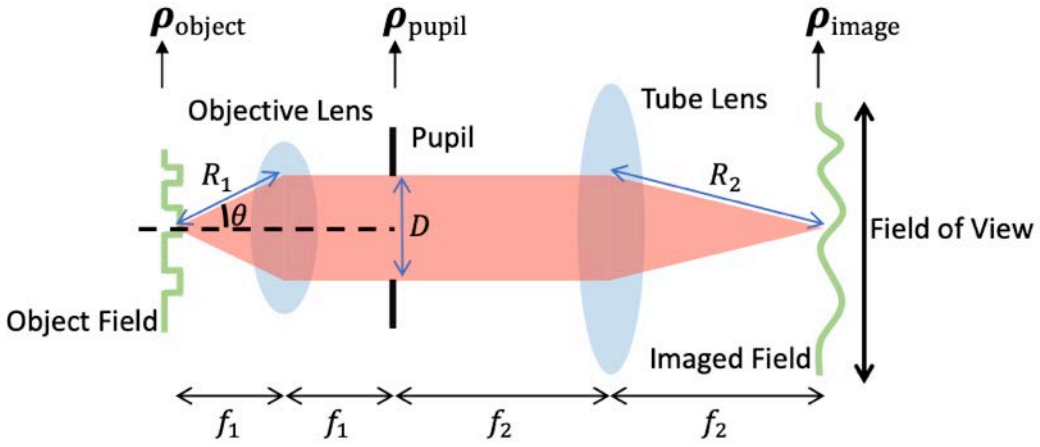

Figure 1.3: Imaging system of an microscope is known as a magnifying $4f$ system, composed of an objective lens, a pupil aperture, and a tube lens. f_1 and f_2 are the focal lengths of the two lenses, respectively. Axes of coordinates at each plane are shown on top.

Neglecting the constant, χ, the optical imaging process is expressed as the following:

$$\boldsymbol{U}_{\text{image}}(\boldsymbol{\rho}_{\text{image}}) = \boldsymbol{U}_{\text{image}}(\frac{-R_1}{R_2}\boldsymbol{\rho}_{\text{object}}) = \mathcal{F}\Big\{\boldsymbol{P}(\boldsymbol{\rho}_{\text{pupil}})\mathcal{F}\{\boldsymbol{U}_{\text{object}}(\boldsymbol{\rho}_{\text{object}})\}\Big\}. \tag{1.9}$$

Since the pupil has a finite diameter, D, the cut-off frequency of the imaging system is $\frac{n_{\text{b}}D}{2\lambda R_1}$. Replacing $\frac{n_{\text{b}}D}{2R_1}$ with $n_{\text{b}}\sin\theta$ (the numerical aperture (NA) of the objective lens), the diffraction-limited resolution of the microscope with coherent illumination becomes $\frac{\lambda}{\text{NA}_{\text{obj}}}$ (*i.e.* Abbe's resolution limit [13]). It is possible to maintain the quantitative information of the object while improving the resolution beyond this limit by using partially coherent illumination, followed by digital signal processing on the acquired images (see Sections 1.2 and 1.3). Meanwhile, the magnification of the microscope is $\approx \frac{-f_2}{f_1}$, which only depends on the ratio between the two focal lengths. To defocus the microscope, the objective lens is moved toward or away from the object. Assuming that the defocus distance is Δf, the relationship between the imaged field and the defocused imaged field obeys the Angular Spectrum propagation [9]:

$$\boldsymbol{U}_{\text{image}}(\boldsymbol{\rho}_{\text{image}}; \Delta f) = \mathcal{F}^{-1}\Big\{e^{\text{i}2\pi\Delta f\sqrt{\left(\frac{n_{\text{b}}}{\lambda}\right)^2 - \|\boldsymbol{u}\|_2^2}}\mathcal{F}\{\boldsymbol{U}_{\text{image}}(\boldsymbol{\rho}_{\text{image}}; 0)\}\Big\}. \tag{1.10}$$

Conceptually, we can treat defocus as introducing a specific radially-symmetric phase aberration at the pupil plane (spatial frequency domain). More discussion about system aberrations is in Chapter 3. With the basic knowledge of light scattering and the imaging system mentioned above, we are ready to explore quantitative phase imaging (QPI).

1.2 Quantitative Phase Imaging

Standard optical microscopes use incoherent illumination (*e.g.* LEDs or halogen lamps) for better spatial resolution, higher light throughput and reduction of speckle artifacts, as compared to coherent illumination (*e.g.* lasers). However, the human visual system and optical sensors have integration time much longer than the oscillation frequency of light, which is slightly below 1 petahertz in the visible spectrum. Hence, only absorption information is directly visible under conventional illumination settings, not phase, which is a critical drawback for imaging transparent samples such as biological cells. Many imaging techniques have been proposed to visualize the phase delay of light as it passes through a transparent sample. PhC and DIC render phase effects visible; however, a single image is not quantitative, cannot separate absorption and phase effects, and does not provide physical information about the sample. In contrast to *qualitative* phase imaging methods, *quantitative* phase imaging (QPI) methods recover the phase delay caused by the sample, decoupled from absorption.

2D QPI

Since only the energy of photons can be directly measured and the oscillation frequency of visible light is much higher than the integration time of state-of-the-art image sensors, what we have access to from the sensor is the time-averaged power or intensity. Hence, phase information is either eliminated or coupled with the absorption of the object. There are many methods computationally recover the complex field from intensity measurements; here, we review several common approaches to realize QPI.

Phase-Shifting Interferometry

To extract the phase of the imaged field, $\boldsymbol{U}_{\text{image}}$ in Eq. (1.9), interferometric methods may add a known reference field, $\boldsymbol{U}_{\text{ref}}$. Decoupling the real values amplitude ($\boldsymbol{A}$) and phase ($\boldsymbol{\phi}$) in the complex field, *i.e.* $\boldsymbol{U} = \boldsymbol{A}e^{\mathrm{i}\boldsymbol{\phi}}$, the phase contrast is reflected on the captured intensity, $\boldsymbol{I}$, as expressed below:

$$\begin{aligned}\boldsymbol{I}(\boldsymbol{\rho}) &= |\boldsymbol{U}_{\text{ref}}(\boldsymbol{\rho}) + \boldsymbol{U}_{\text{image}}(\boldsymbol{\rho})|^2 \\ &= |\boldsymbol{U}_{\text{ref}}(\boldsymbol{\rho})|^2 + |\boldsymbol{U}_{\text{image}}(\boldsymbol{\rho})|^2 + \boldsymbol{U}^*_{\text{ref}}(\boldsymbol{\rho})\boldsymbol{U}_{\text{image}}(\boldsymbol{\rho}) + \boldsymbol{U}_{\text{ref}}(\boldsymbol{\rho})\boldsymbol{U}^*_{\text{image}}(\boldsymbol{\rho}) \\ &= \boldsymbol{A}^2_{\text{ref}}(\boldsymbol{\rho}) + \boldsymbol{A}^2_{\text{image}}(\boldsymbol{\rho}) + 2\boldsymbol{A}_{\text{ref}}(\boldsymbol{\rho})\boldsymbol{A}_{\text{image}}(\boldsymbol{\rho})\cos\Big(\boldsymbol{\phi}_{\text{image}}(\boldsymbol{\rho}) - \boldsymbol{\phi}_{\text{ref}}(\boldsymbol{\rho})\Big),\end{aligned} \tag{1.11}$$

where $*$ is the complex conjugate operation. Assuming that the reference field is an on-axis plane wave that has constant amplitude, $\boldsymbol{A}_{\text{ref}} = A_{\text{ref}}$, and constant phase, $\boldsymbol{\phi}_{\text{ref}} = \phi_{\text{ref}}$, across the FoV, the amplitude and phase of the imaged field can be recovered analytically. Based

on Eq. (1.11), phase retrieval is accomplished via the following formulae:

$$\begin{aligned}\boldsymbol{A}_{\text{image}}(\boldsymbol{\rho}) &= \sqrt{\frac{\boldsymbol{I}_0(\boldsymbol{\rho}) + \boldsymbol{I}_\pi(\boldsymbol{\rho}) - 2A_{\text{ref}}^2}{2}}, \text{ and} \\ \boldsymbol{\phi}_{\text{image}}(\boldsymbol{\rho}) &= \tan^{-1}\Big(\frac{\boldsymbol{I}_{\frac{\pi}{2}}(\boldsymbol{\rho}) - \boldsymbol{I}_{\frac{3\pi}{2}}(\boldsymbol{\rho})}{\boldsymbol{I}_0(\boldsymbol{\rho}) - \boldsymbol{I}_\pi(\boldsymbol{\rho})}\Big),\end{aligned} \tag{1.12}$$

where 4 intensity images, $\boldsymbol{I}_{\phi_{\text{ref}}}$, are captured with the phase of the reference field, $\phi_{\text{ref}} \in [0, \frac{\pi}{2}, \pi, \frac{3\pi}{2}]$. Although it looks trivial from math to perform the phase-shifting interferometry [14], the system is physically challenging to build. The incident field passing through the object and the reference field need to be generated from the same quasi-monochromatic source in order to observe interference effect. Since the light source has relatively long coherence length, unwanted scattering along the beam path creates speckle noise. In addition, a precise piezoelectric mirror or spatial light modulator is required to achieve sub-wavelength phase stepping.

Off-Axis Interferometry

When an off-axis plane wave, *i.e.* $\boldsymbol{U}_{\text{ref}} = A_{\text{ref}} e^{\mathrm{i}2\pi \boldsymbol{u}_{\text{ref}} \cdot \boldsymbol{\rho}}$, is used as the reference field, the Fourier transform of the measured intensity can be derived using the convolution and cross-correlation properties. And the spatial frequency spectrum of intensity in Eq. (1.11) becomes:

$$\tilde{\boldsymbol{I}}(\boldsymbol{u}) = A_{\text{ref}}^2 \boldsymbol{\delta}(\boldsymbol{u}) + \tilde{\boldsymbol{U}}_{\text{image}}(\boldsymbol{u}) \star \tilde{\boldsymbol{U}}_{\text{image}}(\boldsymbol{u}) + \tilde{\boldsymbol{U}}_{\text{image}} \star \boldsymbol{\delta}(\boldsymbol{u} - \boldsymbol{u}_{\text{ref}}) + \tilde{\boldsymbol{U}}_{\text{image}}^* \star \boldsymbol{\delta}(\boldsymbol{u} + \boldsymbol{u}_{\text{ref}}). \tag{1.13}$$

Here, $\tilde{x} = \mathcal{F}\{x\}$ represents the Fourier transform of x, $\star$ is the cross-correlation operator. The first two terms in Eq. (1.13) are not modulated by the reference field while the spectra of $\boldsymbol{U}_{\text{image}}$ and $\boldsymbol{U}_{\text{image}}^*$ are shifted in opposite directions due to the modulation. In Sec. 1.1, it is observed that the spatial frequency of the imaged field is band-limited due to the finite aperture size at pupil plane and the Nyquist spatial frequency at the image plane is $\frac{\text{NA}_{\text{obj}} f_1}{\lambda f_2}$. This implies that all the terms in Eq. (1.13) are also band-limited. If the angle of the oblique incident field is large enough, individual term can be separated in Fourier space without overlapping with each other. Hence, digitally *demodulating* the interference intensity with the reference field and applying a low-pass filter to the spectrum results in the complex imaged field. Mathematically, when $\|\boldsymbol{u}_{\text{ref}}\|_2^2 > \frac{3\text{NA}_{\text{obj}} f_1}{\lambda f_2}$, the phase retrieval operations using off-axis interferometry [15] is equivalent to the following expression:

$$\boldsymbol{U}_{\text{image}}(\boldsymbol{\rho}) = \mathcal{F}^{-1}\Big\{\boldsymbol{P}^*(\boldsymbol{u})\mathcal{F}\{\boldsymbol{U}_{\text{ref}}(\boldsymbol{\rho})\boldsymbol{I}(\boldsymbol{\rho})\}\Big\}/A_{\text{ref}}^2. \tag{1.14}$$

While the technique allows us to reconstruct the amplitude and phase from single intensity capture and enables high temporal resolution QPI, it sacrifices the FoV from dense image sampling to prevent spectrum overlapping. Besides, off-axis interferometry shares the same drawbacks as mentioned in Sec 1.2.

Transport of Intensity Equation (TIE)

Phase information also appears in intensity measurements when the imaged field is defocused. The Transport of Intensity Equation (TIE) [16] describes how intensity changes through-focus with relation to the phase of the complex-field:

$$k_o \frac{\partial}{\partial z} \boldsymbol{I}(\boldsymbol{\rho}, z) = -\nabla_{\boldsymbol{\rho}} \boldsymbol{I}(\boldsymbol{\rho}, z) \nabla_{\boldsymbol{\rho}} \boldsymbol{\phi}_{\text{image}}(\boldsymbol{\rho}, z), \tag{1.15}$$

where $\nabla_{\boldsymbol{\rho}}$ is the 2D gradient operator over $\boldsymbol{\rho}$, and z is the axial dimension perpendicular to $\boldsymbol{\rho}$. With intensity measurements at multiple focus positions, the phase is recovered by solving the second-order differential equation [17, 18]. Unlike the interference methods above, Eq. 1.15 is robust under temporally partial coherent illumination, which helps reduce speckle noise and eliminate interference between the object and undesired scattered field due to system imperfectness. However, using spatially coherent illumination still limits the spatial resolution below $\frac{\lambda}{\text{NA}_{\text{obj}}}$. Alternatively, many 2D QPI techniques have been proposed to use spatially partial coherent illumination and manipulate the dispersion of the light source or the aberrations at the pupil plane to retrieve quantitative phase with higher resolution [19, 20, 21, 22, 23, 24]. Although some of these methods work well, they require expensive hardware and precise alignment, which makes them hard to implement on common microscopes.

Fourier Ptychographic Microscopy (FPM)

Fourier Ptychographic Microscopy (FPM) [25] achieves high resolution QPI with illumination coding, requiring no moving parts. In addition, system calibration was easily done computationally [26, 27], which makes it easier to apply to off-the-shelf imaging systems. By scanning the angles of incidence on-axis to off-axis and recording the corresponding intensities, different spatial frequency content of the object field is encoded in each measurement. Mathematically, the forward imaging model from the object plane to the image plane is similar to Eq. (1.9) except for an additional phase modulation from the illumination field, $e^{\text{i}2\pi \boldsymbol{u}_{\text{illu}} \cdot \boldsymbol{\rho}}$:

$$\boldsymbol{I}(\boldsymbol{\rho}, \boldsymbol{u}_{\text{illu}}) = \left| \mathcal{F}^{-1} \left\{ \boldsymbol{P}(\boldsymbol{u}) \mathcal{F}\{ e^{\text{i}2\pi \boldsymbol{u}_{\text{illu}} \cdot \boldsymbol{\rho}} \boldsymbol{U}_{\text{object}}(\boldsymbol{\rho}) \} \right\} \right|^2. \tag{1.16}$$

Unlike the interferometry cases, the frequency spectrum of the complex field is always overlapped with itself in the spectrum of intensity without a reference field. As a result, there is no analytic solution for phase using FPM. In order to perform phase retrieval, the complex field is found iteratively by solving a non-linear optimization problem (see Sec. 1.3). Once the phase of each measurement is resolved, the imaged fields are *demodulated* and stitched together in the spatial frequency domain. The final resolution attainable is $\frac{\lambda}{\text{NA}_{\text{illu}} + \text{NA}_{\text{obj}}}$, where $\text{NA}_{\text{illu}} = \lambda \boldsymbol{u}_{\text{illu,max}}$ is the NA corresponds to the most oblique illumination. While FPM has benefits of high resolution, long DoF, and wide FoV due to use of a low magnification objective lens, it requires many measurements for single phase image reconstruction, which limits the temporal resolution [28].

Differential Phase Contrast (DPC)

Differential Phase Contrast (DPC) [29, 30, 31, 32] is another partially coherent QPI technique that uses asymmetric illumination to shift the sample's spectrum in Fourier space, revealing linear phase information in a weakly scattering object. While raw DPC measurements provide phase contrast which is similar to DIC contrast, the DPC method provides a linearization of the image formation model which can be inverted using a single-step deconvolution process (see Sec. 1.3) [30, 32, 33]. Based on Rytov weakly scattering object assumption, the forward model of DPC is derived in Appendix A.1.

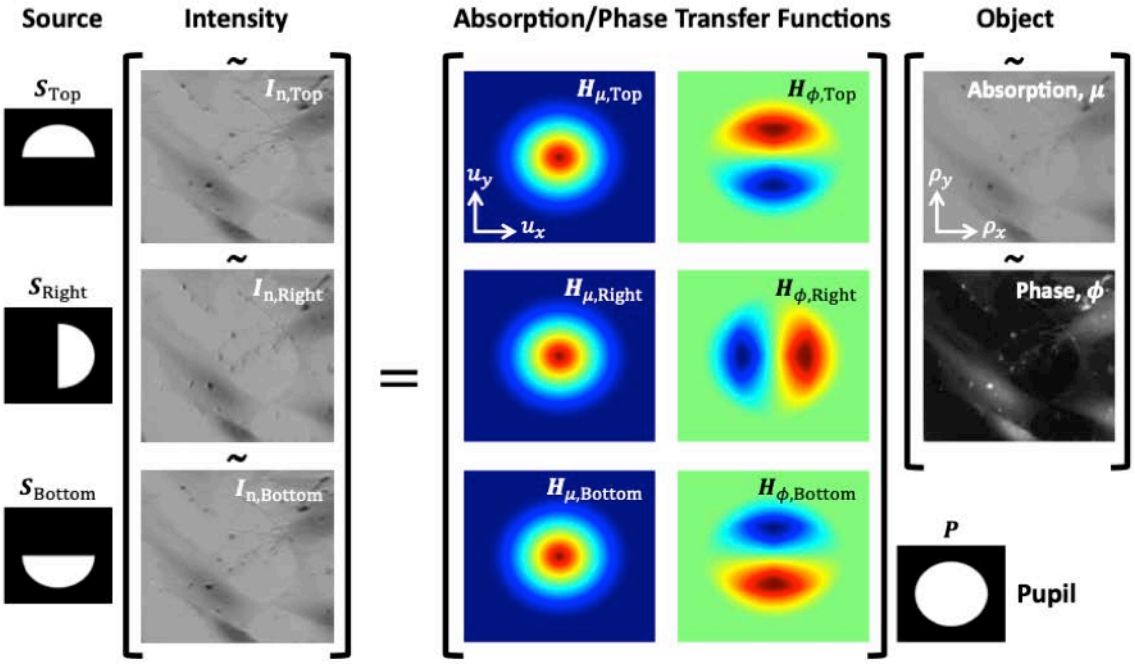

Figure 1.4: Under weakly scattering assumption, a linear relationship between DPC intensity and object's absorption and phase. The forward model of DPC QPI can be visualized as matrix-vector multiplication.

The spatial frequency spectrum of DPC intensities can be written as:

$$\tilde{\boldsymbol{I}}_{\text{n}}(\boldsymbol{u}) = \boldsymbol{H}_{\mu}(\boldsymbol{u})\tilde{\boldsymbol{\mu}}(\boldsymbol{u}) + \text{i}\boldsymbol{H}_{\phi}(\boldsymbol{u})\tilde{\boldsymbol{\phi}}(\boldsymbol{u}), \tag{1.17}$$

where $\boldsymbol{I}_{\text{n}}$ is the normalized intensity, $\boldsymbol{\mu}$ and $\boldsymbol{\phi}$ are the absorption and phase of the object, and $\boldsymbol{H}_{\mu}$ and $\boldsymbol{H}_{\phi}$ are the transfer functions for absorption and phase that can be calculated

using the source shape, $\boldsymbol{S}$, and the pupil function, $\boldsymbol{P}$, in spatial frequency coordinates:

$$\begin{aligned}\boldsymbol{H}_{\mu}(\boldsymbol{u}) &= \Big[\boldsymbol{P}(\boldsymbol{u}) \star \Big(\boldsymbol{P}(\boldsymbol{u})\boldsymbol{S}(\boldsymbol{u})\Big) + \Big(\boldsymbol{P}(\boldsymbol{u})\boldsymbol{S}(\boldsymbol{u})\Big) \star \boldsymbol{P}(\boldsymbol{u})\Big]\,, \text{ and} \\ \boldsymbol{H}_{\phi}(\boldsymbol{u}) &= \Big[\boldsymbol{P}(\boldsymbol{u}) \star \Big(\boldsymbol{P}(\boldsymbol{u})\boldsymbol{S}(\boldsymbol{u})\Big) - \Big(\boldsymbol{P}(\boldsymbol{u})\boldsymbol{S}(\boldsymbol{u})\Big) \star \boldsymbol{P}(\boldsymbol{u})\Big]\,.\end{aligned} \tag{1.18}$$

Figure 1.4 illustrates the linear imaging model. With as few as 3 DPC intensity measurements using different source patterns (*e.g.* top, right, bottom half-circles), DPC QPI recovers both absorption and phase with resolution up to the incoherent resolution limit, *i.e.* $\frac{\lambda}{2\mathrm{NA}_{\mathrm{obj}}}$. In Chapter 2 and 3, we explore a single-shot real-time DPC method via wavelength multiplexing, and an algorithm to digitally calibrate the spatially-varying system aberrations from images under both spatially coherent and DPC illuminations.

3D QPI

When the sample is thicker than the microscope's DoF, we require 3D imaging methods. 2D phase measures *integrated* optical path delay through the sample, so RI and thickness are coupled. This ambiguity between shape and index is naturally removed in 3D QPI, which recovers the 3D RI distribution. Traditionally, 3D phase imaging is achieved tomographically by capturing 2D projections at many angles [34, 35, 36]. In some cases, a ray-based model is sufficient, *e.g.* low resolution X-ray tomography[34, 37, 38]. However, as diffraction effects become prominent in optical microscopy, a *diffraction* tomography model [35, 39] is needed. Generally, this assumes knowledge of the *complex-field* at each angle, requiring a two-step reconstruction: 2D phase retrieval using methods mentioned in Sec. 1.2, followed by tomography to recover 3D RI. As in the 2D case, a linear relationship between the 3D scattering potential and measured fields can be developed based on the weakly scattering assumption. The 1st Born and Rytov models in Eq. (1.6) and (1.7) have a common convolution term, and the Fourier transform of the term is:

$$\mathcal{F}\Big\{\boldsymbol{G}(\boldsymbol{\rho}, z) \otimes_{3\mathrm{D}} \Big(\boldsymbol{V}(\boldsymbol{\rho}, z)\boldsymbol{U}_{\mathrm{in}}(\boldsymbol{\rho}, z)\Big)\Big\} = \tilde{\boldsymbol{G}}(\boldsymbol{u}, \eta)\Big(\tilde{\boldsymbol{V}}(\boldsymbol{u}, \eta) \otimes_{3\mathrm{D}} \tilde{\boldsymbol{U}}_{\mathrm{in}}(\boldsymbol{u}, \eta)\Big), \tag{1.19}$$

where η is the axial spatial frequency coordinate. Similar to the 2D case, the spatial frequency spectrum of the scattering potential experiences a shift when the object is illuminated using plane waves. Let $\boldsymbol{U}_{\mathrm{in}}(\boldsymbol{\rho}, z) = e^{\mathrm{i}2\pi(\boldsymbol{u}_{\mathrm{in}}\cdot\boldsymbol{\rho} + \eta_{\mathrm{in}} z)}$ be the incident field, where $\|\boldsymbol{u}_{\mathrm{in}}\|_2^2 + \eta_{\mathrm{in}}^2 = \frac{n_{\mathrm{b}}^2}{\lambda^2}$. The shifted spectrum can be expressed as:

$$\tilde{\boldsymbol{V}}(\boldsymbol{u}, \eta) \otimes_{3\mathrm{D}} \tilde{\boldsymbol{U}}_{\mathrm{in}}(\boldsymbol{u}, \eta) = \tilde{\boldsymbol{V}}(\boldsymbol{u} - \boldsymbol{u}_{\mathrm{in}}, \eta - \eta_{\mathrm{in}}). \tag{1.20}$$

To further simplify Eq. (1.19), we can use the Fourier representation of the Green's function:

$$\tilde{\boldsymbol{G}}(\boldsymbol{u}, z) = \iint \boldsymbol{G}(\boldsymbol{\rho}, z) e^{-\mathrm{i}2\pi(\boldsymbol{u}\cdot\boldsymbol{\rho})} \mathrm{d}^2\boldsymbol{\rho} = \frac{-\mathrm{i}e^{\mathrm{i}2\pi|z|\boldsymbol{\Gamma}(\boldsymbol{u})}}{4\pi\boldsymbol{\Gamma}(\boldsymbol{u})}\,, \tag{1.21}$$

where $\boldsymbol{\Gamma}(\boldsymbol{u}) = \sqrt{(n_\mathrm{b}/\lambda)^2 - \|\boldsymbol{u}\|_2^2}$. If a transmission microscope is considered, where only the field between the object and the objective lens is captured, *i.e.* $|z| = z$, the 3D Fourier transform of $\boldsymbol{G}$ becomes:

$$\tilde{\boldsymbol{G}}(\boldsymbol{u}, \eta) = \frac{-\mathrm{i}\boldsymbol{\delta}(\eta - \boldsymbol{\Gamma}(\boldsymbol{u}))}{4\pi\boldsymbol{\Gamma}(\boldsymbol{u})} \ . \tag{1.22}$$

As a result, the Green's function kernel effectively samples on a 2D hemisphere, known as the Ewald sphere [11, 40] of radius $\frac{n_\mathrm{b}}{\lambda}$, in the 3D shifted spectrum of scattering potential. Due to the limited pupil size, the imaged field only retains part of the information on the Ewald sphere after the scattered field propagates through the microscope. From Eq. (1.6), (1.7), (1.9) and (1.19)–(1.22), the 2D QPI result is related to the 3D object under the weakly scattering assumption in the following way:

$$\tilde{\boldsymbol{U}}^{\mathrm{1stBorn}}_{\mathrm{scat,image}}(\boldsymbol{u}), \tilde{\boldsymbol{\Phi}}^{\mathrm{Rytov}}_{\mathrm{image}}(\boldsymbol{u}) = \frac{-\mathrm{i}\boldsymbol{P}(\boldsymbol{u})\tilde{\boldsymbol{V}}(\boldsymbol{u} - \boldsymbol{u}_\mathrm{in}, \boldsymbol{\Gamma}(\boldsymbol{u}) - \boldsymbol{\Gamma}(\boldsymbol{u}_\mathrm{in}))}{4\pi\boldsymbol{\Gamma}(\boldsymbol{u})}. \tag{1.23}$$

Figure 1.5 visualizes the above relationship between the spatial frequency spectra of the weakly-scattered fields and the object. Only a portion of the scattered light marked by solid lines on the Ewald spheres can be measured at the image plane due to the finite NA of the objective lens. By scanning the illumination angles, different parts of the spatial frequency spectrum are recovered. As a result, the highest lateral resolution achieves $\lambda/(2\mathrm{NA}_\mathrm{obj})$ as $\eta = 0$, and the highest axial resolution becomes $\lambda/(n_\mathrm{b} - \sqrt{n_\mathrm{b}^2 - \mathrm{NA}_\mathrm{obj}^2})$ when $\|\boldsymbol{u}\|_2 = \mathrm{NA}_\mathrm{obj}/\lambda$. After phase retrieval, a 3D inverse Fourier transform reveals the scattering potential in real space. Finally, the computations below convert $\boldsymbol{V}$ into 3D RI:

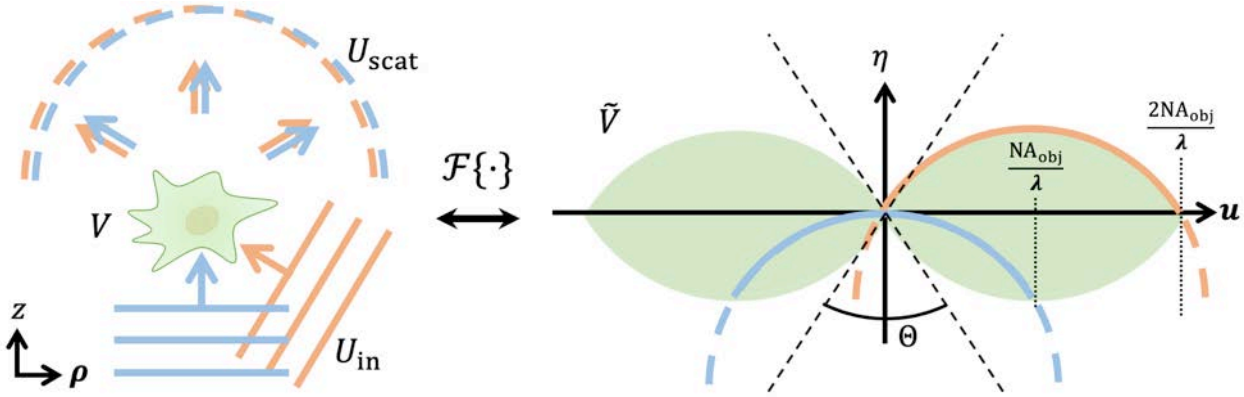

Figure 1.5: Weakly scattering models map the information of the scattered fields using different plane wave illuminations onto different spheres in the 3D spatial frequency spectrum of the object. Combining all possible angles of incidence within the NA of the objective lens, the measurable region (colored in green) forms a donut shape in Fourier space.

$$\boldsymbol{n}(\boldsymbol{r}) = \sqrt{\frac{n_{\mathrm{b}}^2 - \boldsymbol{V}_{\mathrm{Re}}(\boldsymbol{r})/k_o^2 + \sqrt{(n_{\mathrm{b}}^2 - \boldsymbol{V}_{\mathrm{Re}}(\boldsymbol{r})/k_o^2)^2 + \boldsymbol{V}_{\mathrm{Im}}^2(\boldsymbol{r})/k_o^4}}{2}} + \mathrm{i}\sqrt{\frac{\boldsymbol{V}_{\mathrm{Re}}(\boldsymbol{r})/k_o^2 - n_{\mathrm{b}}^2 + \sqrt{(n_{\mathrm{b}}^2 - \boldsymbol{V}_{\mathrm{Re}}(\boldsymbol{r})/k_o^2)^2 + \boldsymbol{V}_{\mathrm{Im}}^2(\boldsymbol{r})/k_o^4}}{2}}, \tag{1.24}$$

where $\boldsymbol{V}_{\mathrm{Re}}$ and $\boldsymbol{V}_{\mathrm{Im}}$ are the real and imaginary parts of $\boldsymbol{V}$, respectively. This builds the foundation of Optical Diffraction Tomography (ODT) and enables many bio-imaging applications [**Chowdhury2017:SI3DODT**, 35, 41]. However, an area indicated by the cone angle Θ around the origin in object's spectrum is missing, which causes anisotropic resolution and distorted shape in the final reconstruction. In addition, the 2D phase projection reconstructions may contain artifacts that propagate to the 3D reconstruction. Global reconstruction methods that relate all the measurements to the final estimate, without an intermediate 2D phase retrieval step, can be more robust to experimental errors [42, 43]. In Chapter 4, quantitative DPC microscopy is extended to 3D, which eliminates the need of interferometry. With a proposed 3D deconvolution algorithm, the RI of thick objects is directly reconstructed from through-focus intensity measurements. At the same time, prior knowledge of the objects is enforced in the algorithm to mitigate the missing cone artifacts. On the other hand, multiple-scattering phenomenon occurs when RI contrast of the object increases, and breaks the linear model in Eq. (1.23). To tackle this problem, an efficient and accurate multiple-scattering 3D QPI method with intensity-only measurements is proposed in Chapter 5 and compared against the other weakly and multiple-scattering models.

1.3 Phase Retrieval by Solving Inverse Problems

Although the forward model varies in Sec. 1.2 among different QPI methods, all of them can potentially be solved by the same algorithm. This is due to the fact that phase retrieval essentially solves an inverse problem, given the data acquired at the image plane. Hence, all post-processing computations in QPI can be posed as trying to find the optimal solution of the following type of optimization problem and objective function:

$$\boldsymbol{o}^\star = \arg\min_{\boldsymbol{o}} \sum_{m=1}^{M} \left\| \boldsymbol{I}_m - \mathcal{H}_m(\boldsymbol{o}) \right\|_2^2 + \mathcal{R}(\boldsymbol{o}). \tag{1.25}$$

Here, the total number of measurements is M, each of the captured intensity images is denoted as $\boldsymbol{I}_m$, $\boldsymbol{o}$ is the 2D complex field or 3D RI of the object, and $\mathcal{H}_m$ represents a known forward model for specific QPI method. The ℓ_2 norm in the objective function, or data fidelity term, measures the difference between the noisy measurements and the predictions based on the estimated object. Therefore, a solution is found after the minimization process. Often, the inverse problem is ill-posed because of low Signal-to-Noise Ratio (SNR) and lack

of information. In those cases, we can incorporate a regularization term $\mathcal{R}$, which imposes *a priori* knowledge about the object to mitigate reconstruction artifacts. In addition, more than one variable can be optimized in Eq. (4.11) to improve the phase retrieval results. For example, it is possible to computationally correct errors in system alignments and image aberrations from the imperfect measurements [26, 27]. In Chapter 3, a self-calibration algorithm with 4 DPC measurements is achieved using a similar idea. A few common algorithms for solving such optimization problems are reviewed below and used in the Chapter 2–5.

Least-Squares method

When the forward model is linear with an ℓ_2 or Tikhonov regularization, *i.e.* $\mathcal{R}(o) = \gamma_o \|o\|_2^2$, there exists an analytic solution in Eq. (4.11). For instance, with regularization parameters γ_μ and γ_ϕ for absorption and phase, the quantitative DPC forward model in Eq. (1.17) turns Eq. (4.11) into:

$$\boldsymbol{\mu}^\star, \boldsymbol{\phi}^\star = \arg\min_{\boldsymbol{\mu},\boldsymbol{\phi}} \sum_{m=1}^{M} \left\| \tilde{\boldsymbol{I}}_{\mathrm{n},m} - \boldsymbol{H}_\mu \tilde{\boldsymbol{\mu}} - \boldsymbol{H}_\phi \tilde{\boldsymbol{\phi}} \right\|_2^2 + \gamma_\mu \left\| \tilde{\boldsymbol{\mu}} \right\|_2^2 + \gamma_\phi \left\| \tilde{\boldsymbol{\phi}} \right\|_2^2, \tag{1.26}$$

which leads to a global optimal solution using the least-squares method [32, 33]:

$$\tilde{\boldsymbol{\mu}}^\star = \frac{\left(\sum_m |\tilde{\boldsymbol{H}}_{\phi,m}|^2 + \gamma_\phi\right) \sum_m \left(\tilde{\boldsymbol{H}}^*_{\mu,m} \tilde{\boldsymbol{I}}_{\mathrm{n},m}\right) - \sum_m \left(\tilde{\boldsymbol{H}}^*_{\mu,m} \tilde{\boldsymbol{H}}_{\phi,m}\right) \sum_m \left(\tilde{\boldsymbol{H}}^*_{\phi,m} \tilde{\boldsymbol{I}}_{\mathrm{n},m}\right)}{\left(\sum_m |\tilde{\boldsymbol{H}}_{\mu,m}|^2 + \gamma_\mu\right)\left(\sum_m |\tilde{\boldsymbol{H}}_{\phi,m}|^2 + \gamma_\phi\right) - \sum_m \left(\tilde{\boldsymbol{H}}_{\mu,m} \tilde{\boldsymbol{H}}^*_{\phi,m}\right) \sum_m \left(\tilde{\boldsymbol{H}}^*_{\mu,m} \tilde{\boldsymbol{H}}_{\phi,m}\right)}, \tag{1.27}$$

$$\tilde{\boldsymbol{\phi}}^\star = \frac{-\mathrm{i}\left[\left(\sum_m |\tilde{\boldsymbol{H}}_{\mu,m}|^2 + \gamma_\mu\right) \sum_m \left(\tilde{\boldsymbol{H}}^*_{\phi,m} \tilde{\boldsymbol{I}}_{\mathrm{n},m}\right) - \sum_m \left(\tilde{\boldsymbol{H}}_{\mu,m} \tilde{\boldsymbol{H}}^*_{\phi,m}\right) \sum_m \left(\tilde{\boldsymbol{H}}^*_{\mu,m} \tilde{\boldsymbol{I}}_{\mathrm{n},m}\right)\right]}{\left(\sum_m |\tilde{\boldsymbol{H}}_{\mu,m}|^2 + \gamma_\mu\right)\left(\sum_m |\tilde{\boldsymbol{H}}_{\phi,m}|^2 + \gamma_\phi\right) - \sum_m \left(\tilde{\boldsymbol{H}}_{\mu,m} \tilde{\boldsymbol{H}}^*_{\phi,m}\right) \sum_m \left(\tilde{\boldsymbol{H}}^*_{\mu,m} \tilde{\boldsymbol{H}}_{\phi,m}\right)}. \tag{1.28}$$

Since no iteration is involved and the Fourier transform operations are efficiently computed with the Fast Fourier Transform (FFT), solutions using Eq. 1.27 and 1.28 are suitable for real-time applications. However, this simple regularization method works only when SNR is high and it is not robust to situations where some absorption and phase information are missing in the measurements.

Alternating Direction Method of Multipliers (ADMM)

For 3D QPI on conventional optical microscopes, only a limited range of angles pass through the optical system, set by the NA, which results in anisotropic resolution in the axial dimension. Direct 3D phase retrieval with Tikhonov regularization causes artifacts from high-frequency noise and underestimated halo effects (see Chapter 4). *A priori* knowledge of the

sample can be incorporated to achieve realistic 3D reconstructions. For example, we can control the background RI surrounding the object such that $n_\mathrm{b} \leq \boldsymbol{n}(\boldsymbol{r})$ or $n_\mathrm{b} \geq \boldsymbol{n}(\boldsymbol{r})$, $\forall \boldsymbol{r}$. If the types of materials within the volume of interest is sparse, the object can be assumed piece-wise smooth. In order to make adding priors straightforward, the inverse problem can be formulated as a constrained optimization problem:

$$\min \quad \frac{1}{2}\left\|\mathbf{A}\boldsymbol{x}-\boldsymbol{b}\right\|_2^2 + \mathcal{I}_\Omega(\boldsymbol{z}_1) + \tau\left\|\boldsymbol{z}_2\right\|_1, \text{ subject to } [\mathbf{I}^\mathrm{T} \ \mathbf{D}^\mathrm{T}]^\mathrm{T}\boldsymbol{x} = [\boldsymbol{z}_1^\mathrm{T} \ \boldsymbol{z}_2^\mathrm{T}]^\mathrm{T}, \tag{1.29}$$

where $\mathbf{A}$ is a block-diagonal convolution matrix composed of transfer functions, $\boldsymbol{x}$ is the vectorized scattering potential to be recovered, $\boldsymbol{b}$ is a vectorized concatenated 3D intensity stack, $\mathbf{I}$ represents the identity matrix, $\mathbf{D}$ is discrete derivative matrix in all three dimensions, T denotes matrix transpose and τ is a regularization parameter. Here, two prior terms, $\mathcal{I}_\Omega(\boldsymbol{z}_1)$ and $\|\boldsymbol{z}_2\|_1$, are applied. $\mathcal{I}_\Omega(\boldsymbol{z}_1)$ is either a positive or negative indicator function and $\|\boldsymbol{z}_2\|_1$ implements an anisotropic total variation (TV) regularizer.

Alternating Direction Method of Multipliers (ADMM) [44] provides an efficient way to solve this non-smooth convex inverse problem. First, we need to find the augmented Lagrangian $\mathcal{L}$ of Eq. (1.29),

$$\mathcal{L}(x, z_1, z_2, y) = \frac{1}{2}\left\|\mathbf{A}\boldsymbol{x}-\boldsymbol{b}\right\|_2^2 + \mathcal{I}_\Omega(\boldsymbol{z}_1) + \tau\left\|\boldsymbol{z}_2\right\|_1 + \frac{\beta}{2}\left\|[\mathbf{I}^\mathrm{T} \ \mathbf{D}^\mathrm{T}]^\mathrm{T}\boldsymbol{x} - [\boldsymbol{z}_1^\mathrm{T} \ \boldsymbol{z}_2^\mathrm{T}]^\mathrm{T} + \frac{\boldsymbol{y}}{\beta}\right\|_2^2, \tag{1.30}$$

which adds a quadratic function corresponding to the constraints with a tuning penalty parameter, $\beta > 0$, and Lagrange multiplier, $\boldsymbol{y}$. The ADMM form of the 3D deconvolution problem can be written as the following iterative algorithm, containing alternating minimization of the unconstrained $\mathcal{L}$ followed by a dual update:

$$\boldsymbol{x}_{k+1} = \arg\min_{\boldsymbol{x}} \quad \mathcal{L}(\boldsymbol{x}, \boldsymbol{z}_{1,k}, \boldsymbol{z}_{2,k}, \boldsymbol{y}_k) \tag{1.31a}$$

$$\boldsymbol{z}_{1,k+1} = \arg\min_{\boldsymbol{z}_1} \quad \mathcal{L}(\boldsymbol{x}_{k+1}, \boldsymbol{z}_1, \boldsymbol{z}_{2,k}, \boldsymbol{y}_k) \tag{1.31b}$$

$$\boldsymbol{z}_{2,k+1} = \arg\min_{\boldsymbol{z}_2} \quad \mathcal{L}(\boldsymbol{x}_{k+1}, \boldsymbol{z}_{1,k+1}, \boldsymbol{z}_2, \boldsymbol{y}_k) \tag{1.31c}$$

$$\boldsymbol{y}_{k+1} = \boldsymbol{y}_k + \beta\left([\mathbf{I}^\mathrm{T} \ \mathbf{D}^\mathrm{T}]^\mathrm{T}\boldsymbol{x}_{k+1} - [\boldsymbol{z}_{1,k+1}^\mathrm{T} \ \boldsymbol{z}_{2,k+1}^\mathrm{T}]^\mathrm{T}\right), \tag{1.31d}$$

where k indicates the iteration number, and $z_{1,0}$, $z_{2,0}$, and y_0 are set to 0 initially. Equation (1.31) is equivalent to the generalized LASSO problem [44] with a positive/negative constraint. Hence, each sub-minimization can be solved efficiently, where (1.31a) finds a pseudo-inverse solution of $\boldsymbol{x}$, (1.31b) is the element-wise Euclidean norm projection onto the set Ω, and (1.31c) implements element-wise soft-thresholding with a threshold value $\frac{\tau}{\beta}$. When the forward model is not linear or more constraints are added, the ADMM algorithm needs more memory for storing the splitting variables and the Lagrange multiplier. Therefore, alternative memory efficient algorithms are preferred, especially in 3D QPI.

Proximal Gradient Descent Method

Unlike DPC microscopy, most of the forward models of 2D and 3D QPI methods are nonlinear. Therefore, the least-squares algorithm does not apply and the memory requirement becomes too high to make ADMM practical. The most generic algorithm for solving Eq. (4.11) is then proximal gradient descent, which is also an iterative method. Assume the regularization function $\mathcal{R}$ is non-smooth or non-differentiable, such as the TV norm. Each iteration of the algorithm splits into two steps; In k^{th} iteration, a gradient descent update with a step size α is first performed using the Wirtinger derivative [45] of the data fidelity term, *i.e.*

$$\boldsymbol{o^k} = \boldsymbol{o^k} - \alpha \sum_m^M \Big(\frac{\partial \mathcal{H}_m(\boldsymbol{o})}{\partial \boldsymbol{o}} \Big)^{\mathrm{H}} \Big(\mathcal{H}_m(\boldsymbol{o}) - \boldsymbol{I}_m \Big), \tag{1.32}$$

where H represents Hermitian transpose. This process refines the estimation of the object such that it ensures a better prediction of the intensity images. In order to account for the regularization term, a proximal operator is applied to the updated object, in which another optimization problem is solved:

$$\boldsymbol{o}^{k+1} = \mathbf{prox}_{\tau\mathcal{R}}(\boldsymbol{o}^k) = \underset{\boldsymbol{z}\in\Omega}{\arg\min}\ \tau\mathcal{R}(\boldsymbol{z}) + \frac{1}{2}\Big\|\boldsymbol{z} - \boldsymbol{o}^k\Big\|_2^2 . \tag{1.33}$$

Here, the regularization parameter τ is a constant adjusting the confidence level of the imposed priors, and Ω constrains the bounds of potential solutions. And usually there exists efficient computational methods to implement this proximal step [44, 46, 47]. By repeating Eq. 1.32 and 1.33 several times, phase or RI values converge to a local minimum. Although an initial guess using linear models, *e.g.* DPC QPI, can help reconstructions start close to the global optimum [28], initialization with zero phase is often robust enough to find an accurate solution as demonstrated in Chapter 5. Adopting Nesterov's acceleration scheme between the iterations, the convergence rate improves from *sublinear* result of $O(1/k)$ to the optimal result of $O(1/k^2)$ for first order methods. Combining proximal gradient descent and Nesterov's acceleration is also known as the Fast Iterative Shrinkage-Thresholding Algorithm (FISTA) [48].

1.4 Coded Illumination Using an LED Array

In Sec. 1.2, we learn that it is possible to achieve 2D/3D QPI by purely controlling the patterns of a light source [25, 32]. Most of these QPI methods share several benefits, including high resolution compared to interferometry using coherent light, fast image acquisition without moving parts, and high compatibility with off-the-shelf optical microscopy systems.

Since multiple measurements under various illumination settings are required to recover quantitative phase, coded illumination techniques require a programmable light source.

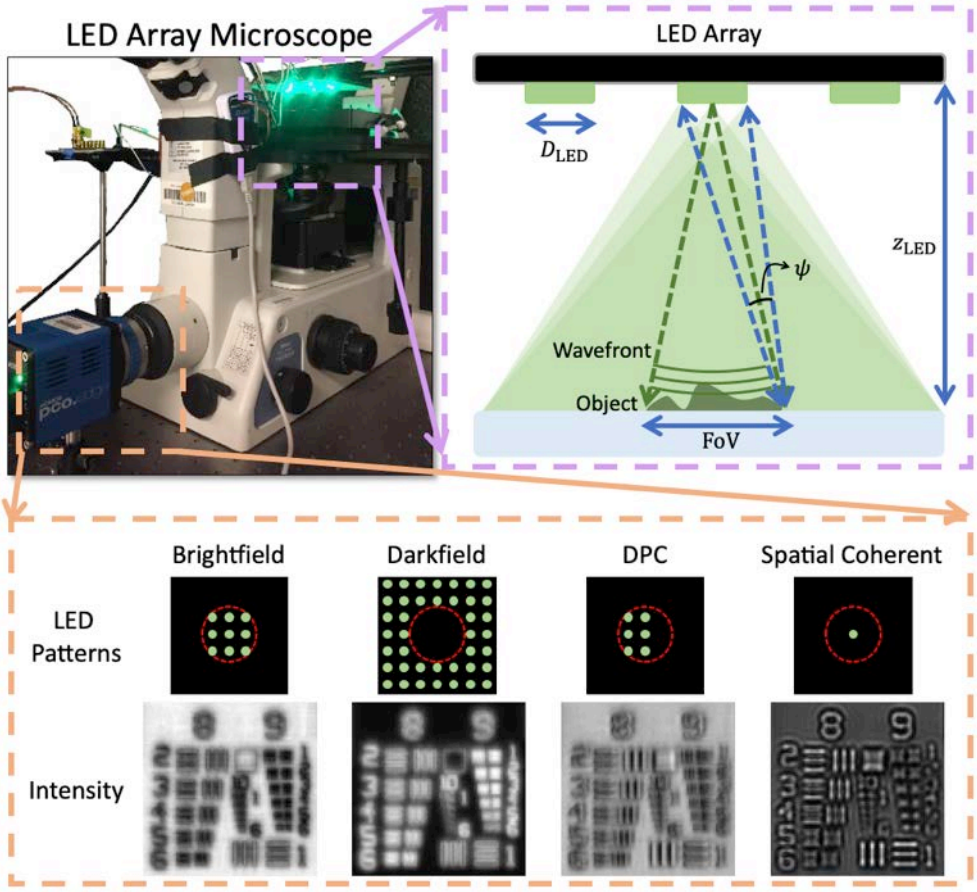

Figure 1.6: LED array microscope replaces conventional illumination path with a programmable LED array in a distance (z_{LED}) from the object plane. When the ratio between FoV and the z_{LED} is small enough, each LED acts as a spatially coherent light source. And simply switching the illumination patterns provide various kinds of image contrast, such as brightfield, darkfield, DPC, and spatial coherent diffraction.

There are many devices that enable light manipulation, such as Galvo mirrors, Digital Micromirror Devices (DMD), and phase Spatial Light Modulators (SLM). However, the expensive costs and bulky relay optics make them sub-optimal. In addition, limited tunable range or small panel size prevents them from generating high angle oblique illuminations, which is critical for reconstructing accurate and high resolution phase results, without adding another $4f$ system on top of the microscope. In the following Chapters, an LED array microscope in Fig. 1.6 is used to serve as the active illumination device. It has been demonstrated that different image contrasts, including brightfield, darkfield, DPC, can be generated with coded LED patterns without additional optics [49, 50]. By placing the planar array several *cm* away from the object plane on a Nikon TE300 inverted microscope, oblique illuminations up

to 0.8NA or 53° can be produced in a compact system. Many QPI methods require spatially coherent light sources to reveal phase contrast [16, 35, 51, 15], and forward models were developed under Köhler illumination that decomposes the illumination into multiple mutually coherent or incoherent plane waves at the object plane for uniform contrast across the FoV[25, 32, 52]. In order to adapt those QPI techniques, the arrangement of the LED array should be carefully designed. A schematic of the illuminating module is drawn in Fig. 1.6, where D_{LED} is the physical size of the LED and z_{LED} denotes the distance between the object plane and the array. Each point on the LED emits a spherical wave that is incoherent with others. Based on the Van Cittert–Zernike theorem [53, 54], the far-field of a single LED source is considered spatially coherent when each position in the FoV has a cone of acceptance, $\psi \approx D_{\text{LED}}/z_{\text{LED}}$, smaller than λ/FoV. Given an LED with fixed size and central wavelength as well as a specified FoV, the array distance should be adjusted as:

$$z_{\text{LED}} > \frac{D_{\text{LED}} \times \text{FoV}}{\lambda}. \tag{1.34}$$

In this work, each LED is about $300\mu m$ wide and has a central wavelength of $0.514\mu m$, and the FoV ranges from tens of μm to over a hundred μm by using objective lenses with various magnifications and an sCMOS camera (PCO.edge 5.5, $6.5\mu m$ pixel size). Hence, the LED array is placed $40 \sim 70mm$ away when spatial coherence is required. In addition, the light propagates sufficiently far (compared to the FoV) that the wavefront close to the object plane becomes flat like a plane wave. Thanks to fast switching electronics, source patterns alternate within a small fraction of the exposure time, which enables camera-limited data acquisition rates. All properties mentioned above imply that almost all QPI leveraging coded illumination can be realized on the low-cost microscope.

1.5 Dissertation Outline

So far we have reviewed the basic knowledge of optical microscopy and underlying physics, and introduced the LED array microscope that servers as a convenient platform to develop novel QPI techniques using coded illumination. In the following chapters, detailed derivation, discussion, analysis, and experimental results of the proposed multidimensional QPI methods are presented. We will demonstrate that computational microscopy can be both practical and powerful, hoping to attract more people to integrate QPI on their microscopes and push science forward. From 2D phase imaging to 3D phase tomography, the rest of the thesis is organized as follows:

- Chapter 2 implements DPC QPI with color-multiplexing for real-time multi-contrast imaging. Most of the QPI methods, including conventional DPC, require multiple measurements to achieve reliable phase retrieval. This sacrifices the temporal resolution, which limits their applications in imaging moving objects. However, images formed under different illumination patterns can be encoded and decoded simultaneously with

an RGB LED array and a color camera. As a result, the proposed color-multiplexed DPC provides camera-limited frame rate and minimizes motion blur.

- Chapter 3 shows an illumination design composing both spatially coherent and partially coherent light, and develops an algorithm to jointly estimate absorption, phase and system aberrations. Since only 4 measurements are required, temporal changes in quantitative phase and pupil aberrations can be resolved. At the same time, spatially-varying aberrations are calibrated by separately processing multiple regions within the whole FoV.

- Chapter 4 demonstrates an intuitive way to gather 3D phase contrast using DPC for 3D RI recovery. When spatially partial coherent illumination is used, the DoF becomes narrow and out-of-focus information cannot reach the image plane. By scanning foci through the 3D object with DPC illuminations, 3D absorption and phase contrast are captured. Based on a weakly scattering assumption, we derive a 3D linear forward model and the corresponding deconvolution algorithm that reconstructs 3D RI of various biological samples.

- Chapter 5 proposes an accurate and efficient 3D multiple-scattering model to image an optically dense object. As phase contrast and thickness of the object increases, the linear models used in previous chapters fail due to multiple-scattering effects. Hence, a more rigorous light scattering model as well as the 3D phase tomography framework are developed to achieve high-resolution large volume 3D QPI.

- Chapter 6 summarizes the contribution of this dissertation and lists a few potential directions to improve 3D QPI with coded illumination.

Chapter 2

Real-Time Quantitative Phase Imaging with Color Multiplexing

2.1 Single-Shot DPC Quantitative Phase Imaging

Amongst the wide array of existing QPI methods, several are single-shot techniques. Off-axis holography interferes the sample beam with a tilted reference beam, then recovers phase by Fourier filtering [15]. Parallel phase-shifting can spatially multiplex several holograms within a single exposure via an array of polarizers [55]. And single-shot QPI add-ons based on amplitude gratings work with commercial microscopes, replacing the traditional camera module [56, 57]. Another add-on option uses two cameras to capture defocused images which can then be used to solve the TIE [58]. Alternatively, if chromatic aberrations are large enough, they can enable single-shot color TIE [59] without any hardware changes. All of these methods require the some spatial or temporal coherence, limiting resolution, but provide camera-limited frame rates.

Our approach described in this chapter, termed color Differential Phase Contrast (cDPC), requires only a *single* color image for multiplexing source patterns[1]. Three RGB source color channels are used to display three different half-circle source patterns. This concept of color multiplexing is similar to that used in photographic depth ranging [60]. A 4th image in original DPC method [32] is not needed, since its information can be extracted by taking the sum of two images acquired with opposite half-circle illuminations (a synthetic brightfield image) and subtracting that of a 90 degree rotated half-circle source. Thus cDPC require only 3 illumination patterns and 3 measurements, which are collected in a single shot using a RGB Bayer filter sensor. One can achieve cDPC by implementing the source pattern in an LED array microscope, which offers many imaging modalities in one platform [25, 31, 32, 49, 50, 61, 62]. However, the proposed configuration does not require a dynamic source, making it possible to use a static multi-color filter placed in the condenser back focal plane, assuming

[1]This work was performed in close collaboration with Zachary F. Phillips (Waller Lab, EECS, UC Berkeley).

Köhler illumination. Both configurations simplify hardware and reduce costs significantly as compared to phase contrast or DIC, while providing quantitative phase, which is more general and can be used to synthesize both of the aforementioned methods digitally [63].

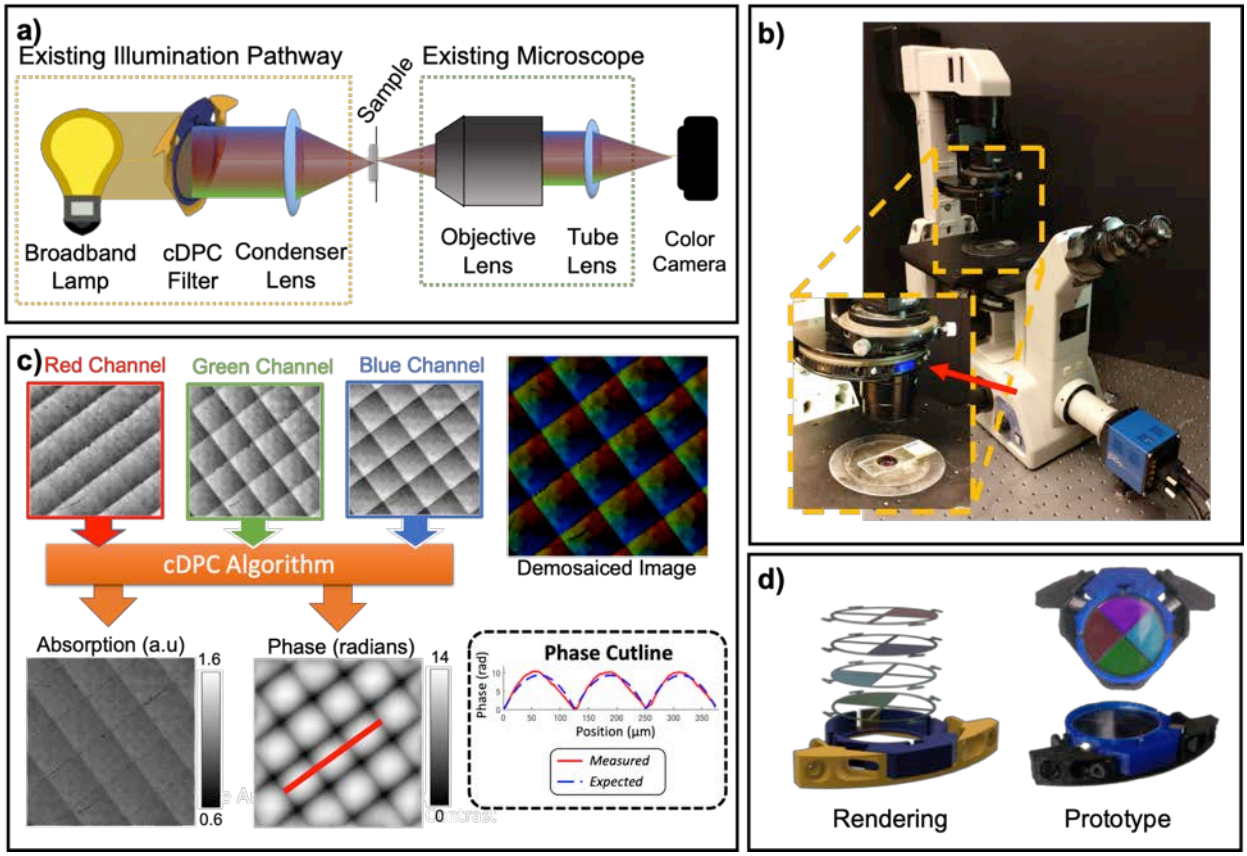

Figure 2.1: Single-shot color Differential Phase Contrast (cDPC) microscopy. a) Optical schematic of a brightfield microscope with a cDPC color filter placed at the back focal plane of the condenser in Köhler configuration. b) Installation in Nikon TE300 microscope condenser turret. c) Reconstruction: the captured color image is separated into its RGB components, which are then used to recover two unknowns (absorption and phase) via a well-posed linear deconvolution. The sample is a micro-lens array (Fresnel Technologies 605). d) CAD model and image of fabricated cDPC insert.

Hardware design

As in conventional DPC, our method requires measurements of the sample illuminated by known asymmetric sources. However, in our case the 3 half-circle sources are turned on simultaneously (for example, in each of the three color channels of an LED array). Since dynamic source patterning is no longer needed, it is not necessary to replace the entire

illumination unit of the microscope with an LED array. Instead, we can make use of the microscope's existing condenser unit, which has a turret commonly used for phase contrast inserts or DIC prisms. This intermediate plane can usually be accessed easily by removing the mechanical inserts. Here, a simple 3D printed color filter that is placed in the condenser turret of a Nikon TE300 microscope (Figure 2.1a).

The filter prototype consists of Polyethylene Terephthalate (PET) color filters (Lee Filter, Inc.) which were laser cut to size and installed into a 3D printed insert designed to fit our microscope. Narrow bandwidth illumination filters, *e.g.* multi-layer coated glass, would provide better spectral selectivity, but suffer from low light throughput and high cost. Therefore, the inexpensive and easy-to-cut PET film filters were chosen; the resulting cross-talk between color channels will be accounted for in post-processing, described below.

The total cost of raw materials is approximately $30 and filters were produced quickly with a 3D printer and laser cutter. One filter is shown in Figure 2.1d; it was installed in the condenser turret of an inverted microscope (Figure 2.1b), replacing one of the removable phase contrast (Ph1, Ph2 or Ph3) inserts.

Calibration

Ideally, the color filters would provide perfect separation of the three source patterns into the three color channels. In reality, both the illumination and camera color channels have cross-talk between the desired wavelengths. To account for this, system calibration is separated into two separate steps: detection-side and illumination-side.

Illumination-side calibration corrects for the relative spectral transmittance of each of the source color filters. The illumination pattern simultaneously encodes three half-circle sources, one each for the RGB color channels. Red and green are opposite half-circles, and blue is rotated by 90 degrees relative to the others. Where the blue and green patterns overlap, a cyan filter (blue + green) was used. Where the blue and red patterns overlap, a purple filter (blue + red) was used. Hence, the final filter design actually contains four quadrants having red, green, cyan and purple filters (see Fig. 2.2).

When filtered by the sensor Bayer pattern, the filters' spectra are not orthogonal. This can be seen in the spectra of each PET film after capture with a color camera (left column of Fig. 2.2). The result is an undesirable loss of asymmetry in the source that reduces phase SNR. However, the asymmetry is accounted for during the reconstruction by modeling the source patterns as in Fig. 2.2.

Detection-side calibration accounts for spectral cross-talk of the camera color channels. Standard RGB Bayer filters do not provide perfect discrimination between RGB wavelengths, but coupling artifacts can be removed by calibration. Given the pixel values from the raw color image with an RGGB Bayer filter ($\boldsymbol{I}_{\mathrm{r}}$, $\boldsymbol{I}_{\mathrm{g1}}$, $\boldsymbol{I}_{\mathrm{g2}}$, $\boldsymbol{I}_{\mathrm{b}}$), it is possible to solve for the decoupled color image ($\boldsymbol{I}_{\mathrm{R}}$, $\boldsymbol{I}_{\mathrm{G}}$, $\boldsymbol{I}_{\mathrm{B}}$) that would be obtained if the sample were illuminated

with a single color, according to the following equation,

$$\begin{bmatrix} \boldsymbol{I}_{\mathrm{r}} \\ \boldsymbol{I}_{\mathrm{g1}} \\ \boldsymbol{I}_{\mathrm{g2}} \\ \boldsymbol{I}_{\mathrm{b}} \end{bmatrix} = \mathbf{C} \begin{bmatrix} \boldsymbol{I}_{\mathrm{R}} \\ \boldsymbol{I}_{\mathrm{G}} \\ \boldsymbol{I}_{\mathrm{B}} \end{bmatrix}. \tag{2.1}$$

The matrix $\mathbf{C}$ is a 4×3 calibration matrix describing the coupling between each color channel. It is generated by filtering the broadband source with each filter independently, then measuring the relative red ($\boldsymbol{I}_{\mathrm{R}}$), green ($\boldsymbol{I}_{\mathrm{G}}$) and blue ($\boldsymbol{I}_{\mathrm{B}}$) read-outs to populate the corresponding column vectors of the $\mathbf{C}$ matrix. The ratio between the intensities of each flat-field image at each detection channel provides a linear weighting of the contribution of each source to our color measurement. Once $\mathbf{C}$ has been measured once, it can be used to pre-process all later measurements by solving Eq. (2.1). This step is important for reducing artifacts in the phase results.

Another important step for cDPC is to account for wavelength-dependent changes in phase and spatial frequency. DPC recovers absorption ($\boldsymbol{\mu}$) and phase ($\boldsymbol{\phi}$) information from intensity measurements. These quantities are defined as:

$$\boldsymbol{\mu} = \frac{2\pi}{\lambda_0}\boldsymbol{\alpha} d, \;\; \boldsymbol{\phi} = \frac{2\pi}{\lambda_0}\boldsymbol{n} d, \tag{2.2}$$

where λ_0 is a reference wavelength, d is the thickness of the sample, $\boldsymbol{n}$ represents RI and $\boldsymbol{\alpha}$ indicates absorption coefficient. Absorption and phase transfer functions are determined by illumination NA, objective NA and illumination wavelength [32]. In the proposed cDPC method, the transfer functions must also consider the change in wavelength of each color channel. Phase ($\boldsymbol{\phi}$) depends on which wavelength is used. By assuming no dispersion in the sample, it is possible to use Eq. (2.2) to synthesize phase for any wavelength by simply multiplying the optical path length ($\boldsymbol{n}d$) by the wave number ($\frac{2\pi}{\lambda_0}$) of a desired reference wavelength λ_0.

Forward model of cDPC

The forward model of cDPC is the same as the monochromatic DPC image formation in Eq. (1.17), except the transfer functions become wavelength dependent. Assume that $\boldsymbol{I}_{\mathrm{n}}$ is the normalized color intensity measurement, and $\boldsymbol{H}_{\mu}$ and $\boldsymbol{H}_{\phi}$ are the wavelength-dependent transfer functions for absorption and phase, it can be expressed in spatial frequency domain as

$$\tilde{\boldsymbol{I}}_{\mathrm{n}}(\boldsymbol{u}, \lambda) = \boldsymbol{H}_{\mu}(\boldsymbol{u}, \lambda)\tilde{\boldsymbol{\mu}}(\boldsymbol{u}) + \mathrm{i}\boldsymbol{H}_{\phi}(\boldsymbol{u}, \lambda)\tilde{\boldsymbol{\phi}}(\boldsymbol{u}), \tag{2.3}$$

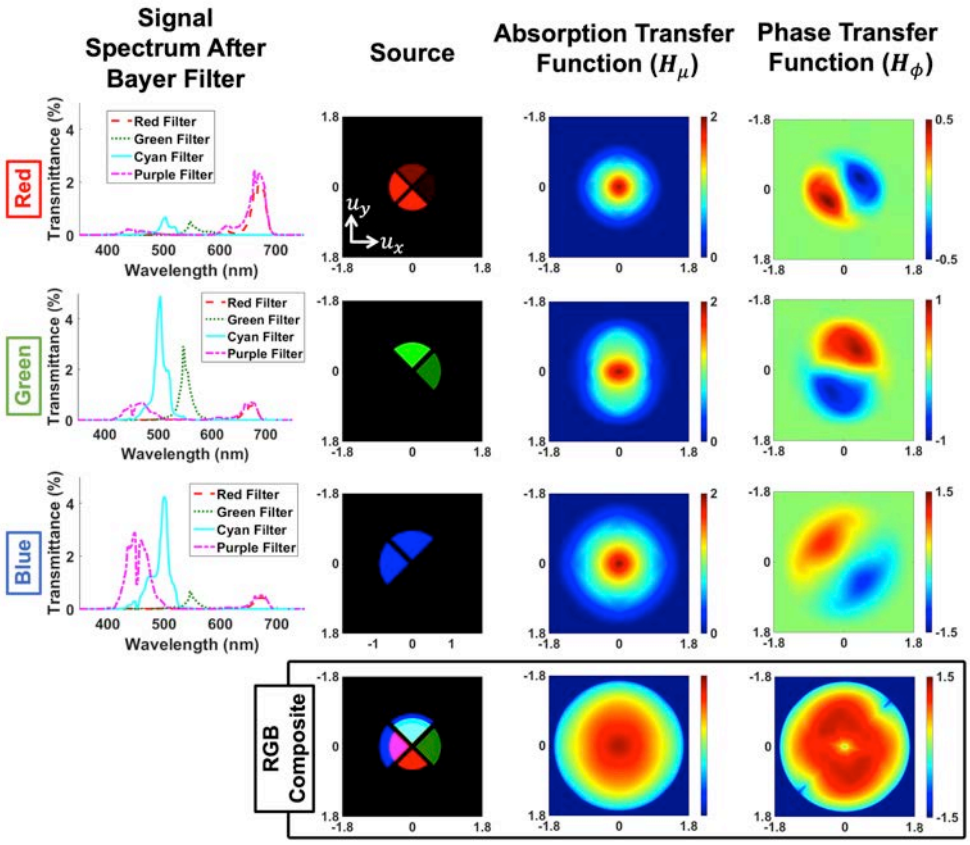

Figure 2.2: Transfer functions for absorption and phase contrast in each cDPC color channel. Left: Spectral contribution of each illumination filter as captured by the camera's Bayer pattern. The following columns show the source represented in each image, and the components of the absorption and phase transfer functions in the spatial frequency domain. Bottom row: sum of each column, representing the calibrated and scaled source and the total coverage of absorption and phase transfer functions, respectively.

where $\boldsymbol{u}$ is 2D spatial frequency coordinates and $\tilde{\cdot}$ denotes Fourier transform. Given a known source ($\boldsymbol{S}$), and pupil function ($\boldsymbol{P}$) which we model as a circle with radius set by the objective NA and λ, the transfer functions are [32, 33]:

$$\boldsymbol{H}_\mu(\boldsymbol{u},\lambda) = \left[\boldsymbol{P}(\boldsymbol{u},\lambda) \star \Big(\boldsymbol{P}(\boldsymbol{u},\lambda)\boldsymbol{S}(\boldsymbol{u},\lambda)\Big) + \Big(\boldsymbol{P}(\boldsymbol{u},\lambda)\boldsymbol{S}(\boldsymbol{u},\lambda)\Big) \star \boldsymbol{P}(\boldsymbol{u},\lambda)\right] \tag{2.4}$$

$$\boldsymbol{H}_\phi(\boldsymbol{u},\lambda) = \frac{\lambda_0}{\lambda}\left[\boldsymbol{P}(\boldsymbol{u},\lambda) \star \Big(\boldsymbol{P}(\boldsymbol{u},\lambda)\boldsymbol{S}(\boldsymbol{u},\lambda)\Big) - \Big(\boldsymbol{P}(\boldsymbol{u},\lambda)\boldsymbol{S}(\boldsymbol{u},\lambda)\Big) \star \boldsymbol{P}(\boldsymbol{u},\lambda)\right], \tag{2.5}$$

where $\star$ denotes cross-correlation. Note that because spatial frequency is a function of wavelength, the source shape $\boldsymbol{S}(\lambda)$ and pupil function $\boldsymbol{P}(\lambda)$ also depend on wavelength.

Specifically, the diameters of the source and transfer functions in Fourier space are inversely proportional to the wavelength of the color channel. Hence, blue illumination provides larger Fourier space coverage and better resolution than red. The forward model accounts for these differences in the color channel's transfer function. Figure 2.2 shows the absorption and phase transfer functions for $\lambda = 0.450\mu m$, $\lambda = 0.546\mu m$ and $\lambda = 0.670\mu m$, with top-left, top-right and bottom-left half-circle sources, respectively.

Examining Fig. 2.2, it is clear that the absorption transfer functions for each color channel are symmetric low-pass filters. The phase transfer functions, on the other hand, are asymmetric band-pass-like filters with a line of missing frequencies along the axis of asymmetry. By rotating the blue half-circle by 90 degrees relative to the red and green ones, the missing line is filled. The overall absorption and phase transfer functions for cDPC are shown in the last row of Fig. 2.2, calculated by summing the absolute values of each color transfer function. As with previous DPC implementations, absorption information loses contrast at high spatial frequencies. Phase has a similar drop-off at high frequencies, but also loses contrast in the low spatial frequency regions. Hence, SNR will be important for accurately recovering low-frequency phase information. The maximum spatial frequency range captured is $2\times$ the NA of the blue color channel. However, the final resolution using cDPC is set by the diffraction limit of green light, since total frequency coverage is set by the maximum spatial frequency which is measured by *two or more* color channels. This comes as an implication of trying to recover two unknowns, absorption and phase, thus requiring at least two measurements.

Inverse problem

Using the forward model developed in Sec. 2.1, the cDPC inverse problem aims to minimize the difference between the measured color image and that which would be measured, given the estimate of the sample's absorption and phase:

$$\min_{\boldsymbol{\mu},\boldsymbol{\phi}} \sum_{m=1}^{3} \left\| \tilde{\boldsymbol{I}}_{\mathrm{n}}(\lambda_m) - \boldsymbol{H}_{\mu}(\lambda_m)\tilde{\boldsymbol{\mu}} - \mathrm{i}\boldsymbol{H}_{\phi}(\lambda_m)\tilde{\boldsymbol{\phi}} \right\|_2^2 + \mathcal{R}(\tilde{\boldsymbol{\mu}}, \tilde{\boldsymbol{\phi}}), \tag{2.6}$$

where $\tilde{\boldsymbol{I}}_{\mathrm{n}}$ is the spatial frequency spectrum of the background-subtracted intensity, $\boldsymbol{H}_{\mu}$ and $\boldsymbol{H}_{\phi}$ are transfer functions for absorption and phase, $\tilde{\boldsymbol{\mu}}$ and $\tilde{\boldsymbol{\phi}}$ are the spatial frequency spectra of absorption and phase, m is the wavelength index and $\mathcal{R}(\tilde{\boldsymbol{\mu}}, \tilde{\boldsymbol{\phi}})$ is a regularization term (typically on the order of 10^{-3}). This problem is linear and can be solved with a one-step least-squares solution (e.g. Wiener deconvolution [64]) or by an iterative algorithm (e.g. gradient descent). The ideal choice of regularizer $\mathcal{R}(\tilde{\boldsymbol{\mu}}, \tilde{\boldsymbol{\phi}})$ depends on the sample and noise. Basic ℓ_2 regularization should be tuned to suppress noise amplification in spatial frequencies that are measured with low-contrast, without destroying sample information at those frequencies. Alternatively, if the sample is sparse (only a few non-zero values), one can use an ℓ_1 regularizer [65]. Other types of *a priori* information may be incorporated by

appropriate regularization. All experiments presented in this chapter make no assumptions on the sample structure; However, ℓ_2 regularization is used to constrain the total energy of the signal and make the problem well-posed. Equation (2.6) thus becomes,

$$\min_{\boldsymbol{\mu},\boldsymbol{\phi}} \sum_{m=1}^{3} \left\| \tilde{\boldsymbol{I}}_{\mathrm{n}}(\lambda_m) - \boldsymbol{H}_{\mu}(\lambda_m)\tilde{\boldsymbol{\mu}} - \mathrm{i}\boldsymbol{H}_{\boldsymbol{\phi}}(\lambda_m)\tilde{\boldsymbol{\phi}} \right\|_2^2 + \gamma_{\mu} \left\| \tilde{\boldsymbol{\mu}} \right\|_2^2 + \gamma_{\phi} \left\| \tilde{\boldsymbol{\phi}} \right\|_2^2, \tag{2.7}$$

which remains differentiable and allows us to find the global minimum solution for absorption and phase with a single matrix inversion step. The final reconstruction for the absorption and phase are obtained using Eq. (1.27) and Eq. (1.28).

2.2 Experimental Results and Discussion

To experimentally validate the proposed cDPC method, results were compared with two established QPI methods: monochromatic DPC and through-focus phase retrieval (Fig. 2.3). For fair comparison, all are implemented on the same Nikon TE300 microscope using illumination generated by an RGB LED array (Adafruit). cDPC uses a discretized version of the cDPC color filter design displayed on the LED array. Monochromatic DPC uses 4 images captured with each of 4 asymmetric source patterns [50]. Through-focus phase imaging uses only the central green LED (for temporal and spatial coherence) while capturing 14 images at different focus depths; phase is then recovered by a nonlinear optimization phase retrieval method [66].

Because of the coherent illumination, through-focus phase imaging has 2× worse resolution than DPC methods. Thus, a 20× 0.4 NA objective lens was used for DPC methods, but switched to a 60× 0.8 NA objective for through-focus phase, in order keep resolution equal for all three. Spatial resolution is quantified using a spoke-pattern phase target [67].

As can be seen in Fig. 2.3, the RGB color channel images have similar contrast to the left, right and top images of the monochromatic DPC, as expected. The phase results are also similar, with equivalent spatial resolution. Because the cDPC image is captured in one shot with color filters, it has lower SNR than monochromatic DPC and deviates in its low-frequency fluctuations, which have weaker transfer function values. Overall, however, single-shot cDPC performs comparably to multi-shot DPC.

Next, the LED array was removed and the microscope's condenser unit was reinstalled with an broadband arc lamp light source. Alternatively, a high-power blue-phosphor static LED source could be used. The color filter was then inserted into the condenser turret, as shown in Figs. 2.1b and 2.1d. Figure 2.4 shows amplitude and phase reconstructions from the cDPC method with objectives of various magnification, as well as simulated phase contrast and DIC images. This imaging method is compatible with any standard objective having

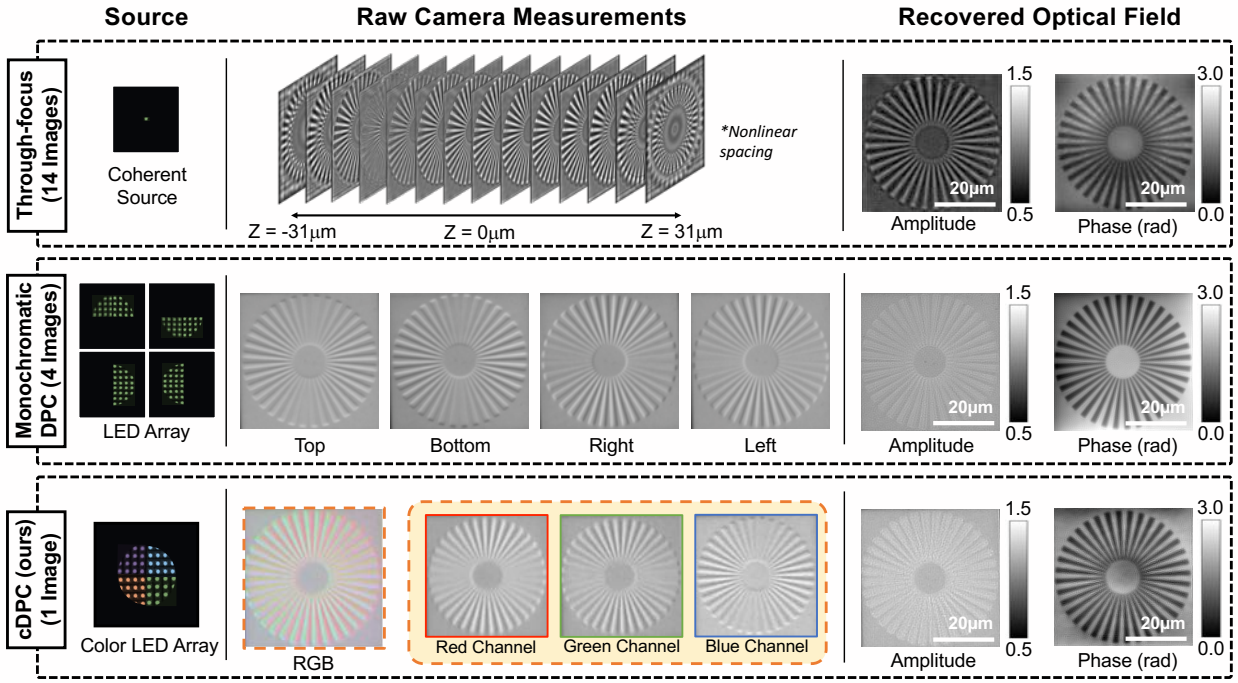

Figure 2.3: Experimental comparison of single-shot cDPC with monochromatic DPC and through-focus phase retrieval methods. (Left) Source patterns. (Middle) Raw camera measurements. (Right) Recovered optical field. DPC methods (partially coherent) were acquired using a 20× 0.4NA objective lens, while through-focus images (spatially coherent) were captured using 60× 0.8NA, in order to ensure equal resolution in all cases.

$\mathrm{NA}_{\mathrm{objective}} \leq \mathrm{NA}_{condenser}$. The ratio of $\mathrm{NA}_{\mathrm{objective}}$ to $\mathrm{NA}_{condenser}$ is referred to as the spatial coherence factor σ [32], defined as:

$$\sigma = \frac{\mathrm{NA}_{\mathrm{illumination}}}{\mathrm{NA}_{\mathrm{objective}}}. \tag{2.8}$$

In other words, $\sigma < 1$ will result in reduced phase contrast as compared to the $\sigma \geq 1$ case, as demonstrated in [32]. This is because low frequencies in phase are revealed only when using high-angle illuminations. It is important to note that illumination with $\sigma > 1$ does not improve resolution beyond the incoherent resolution limit, but also does not degrade image quality, allowing us to fix the condenser NA and use any objective with $\mathrm{NA}_{\mathrm{objective}} \leq \mathrm{NA}_{condenser}$ without changing the hardware. The Nikon TE300 microscope used in this study was configured with a 0.53NA condenser lens. To Perform high resolution cDPC imaging would require high-NA illumination, *e.g.* by using a domed LED array [62]. Temporal coherence is set by the bandwidth of the color filters, since those have narrower bandwidth than the camera filters. The full-width-half-maximum (FWHM) bandwidth for our filters was approximately $50nm$, which is similar to the emission spectrum of the LED array used

previously [32].

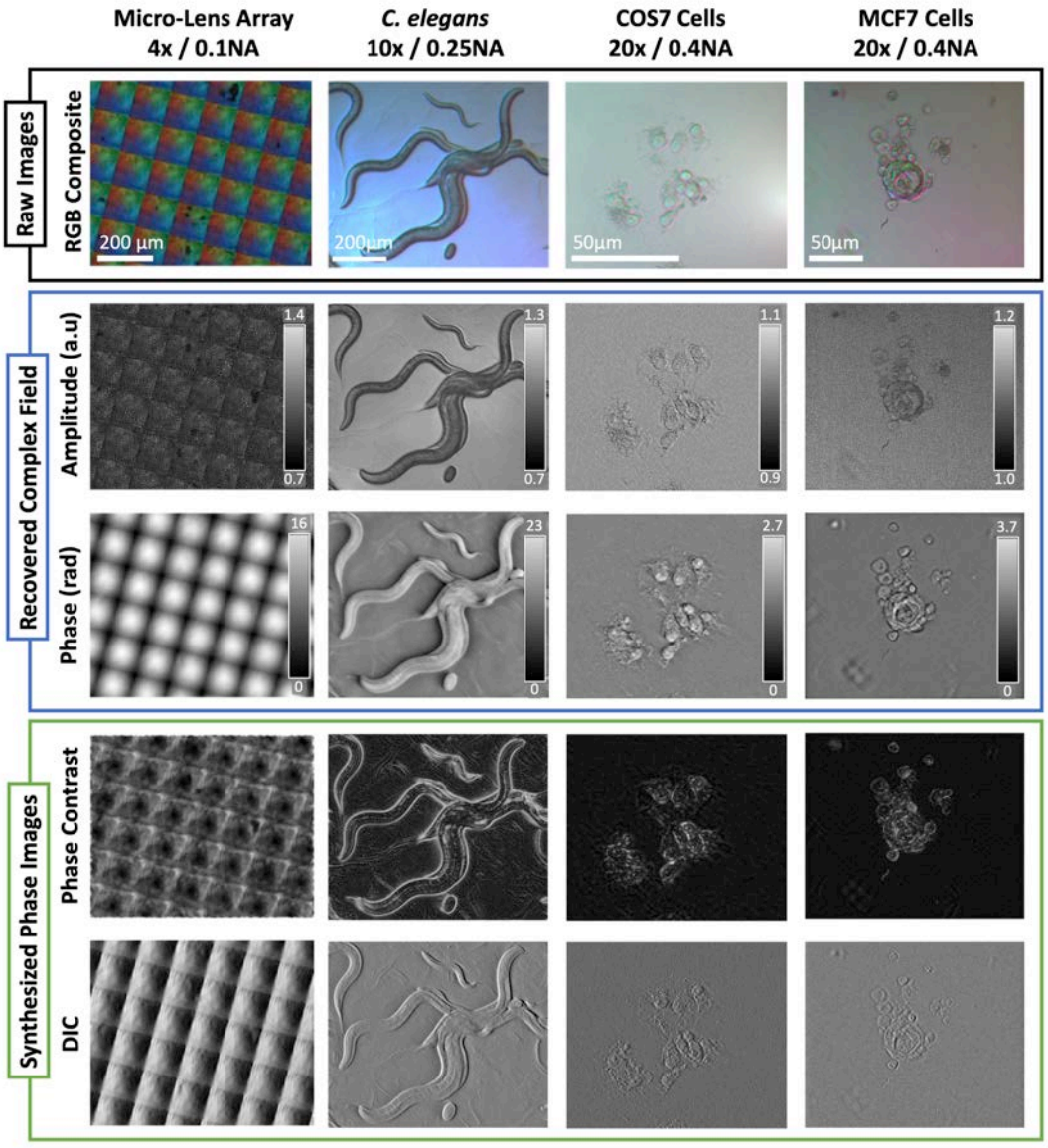

Figure 2.4: Raw data, phase and amplitude reconstructions, synthesized phase contrast and DIC images for various samples and magnifications: (First column) micro-lens array (4× 0.10NA). (Second column) wild-type *C. elegans* (10× 0.25NA). (Third column) HEK 293T cells (20× 0.40NA). (Fourth column) MCF7 cells (20× 0.40NA).

Temporal resolution

Since cDPC is single-shot, temporal resolution is set by the camera's frame rate, giving a factor of 4 improvement over conventional DPC. Single-shot methods reduce artifacts due to motion blur and image registration. This can be seen in Fig. 2.5, where we compare cDPC and conventional DPC (4 images) results for a live *C. elegans* culture. Motion blur is significantly reduced with cDPC, since the sample changes rapidly between frames, even at 12.5 frames per second (FPS). The camera-limited acquisition at 100 FPS was achieved and capturing real-time quantitative phase videos becomes possible for applications, such as imaging live *C. elegans* or floating cells in a microfluidic channel.

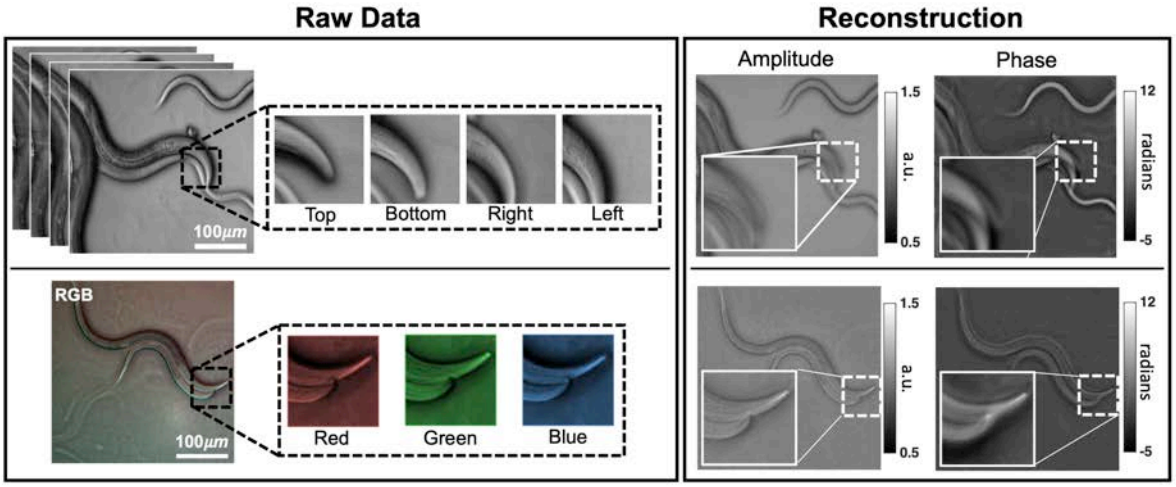

Figure 2.5: Experimental demonstration of motion blur reduction with cDPC vs. conventional DPC. The cDPC method results in significantly reduced motion blur artifacts due to its single-shot acquisition.

Synthesized PhC and DIC images

Differential Interference Contrast (DIC) and conventional Phase Contrast (PhC) microscopy are widely used in medicine and biomedical research. Optical components required for their implementation remain expensive, however, and alignment by an experienced user is required for acceptable performance. Both DIC and phase contrast can be described by forward models which produce a qualitative mixture of amplitude and phase images [1, 68]. Quantitative phase imaging methods can therefore be used to synthesize these contrast mechanisms digitally, mimicking the physical optical system through numerical simulation. Synthesized images from cDPC, as well as ground truth DIC and PhC images, are shown in Fig. 2.6 to be comparable.

Synthesizing DIC and PhC may be useful for clinicians and researchers who have been trained with them to make diagnoses or decisions. While all QPI methods can be used to

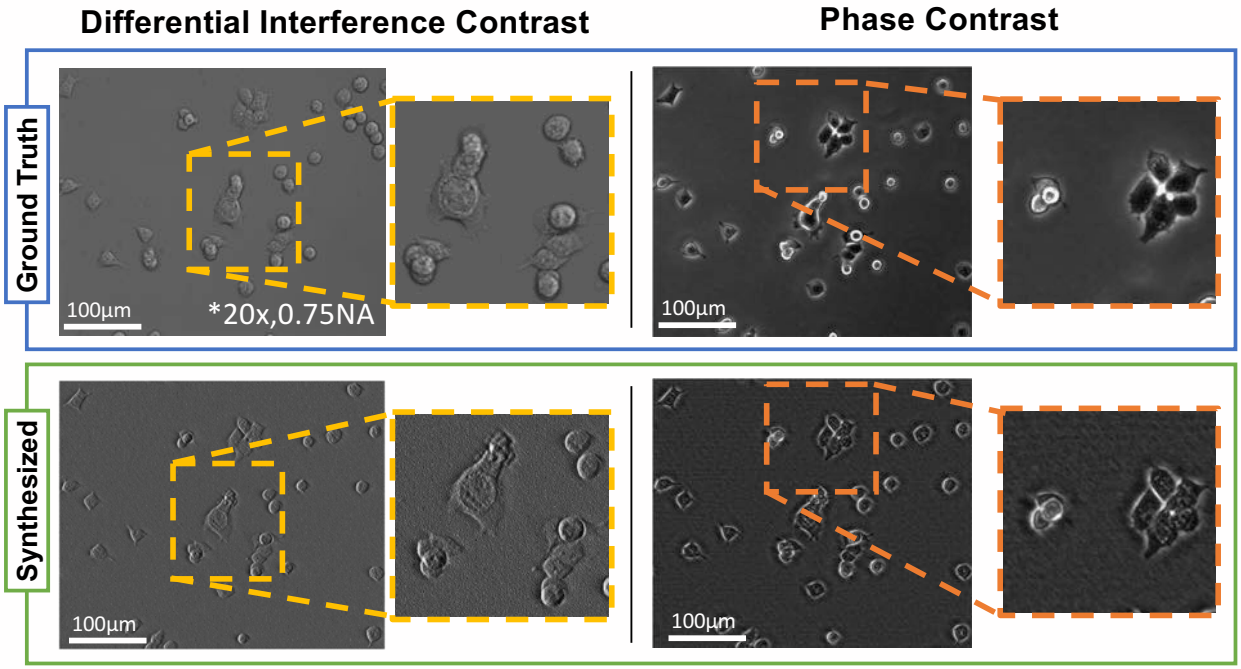

Figure 2.6: Comparison of standard DIC and PhC images to their synthesized counterparts from cDPC. Ground truth DIC images were acquired using a 20× 0.75NA objective and phase contrast images using a 20× 0.40NA PhC objective. cDPC images were acquired using a 20× 0.40NA objective and the filter insert.

synthesize these images, cDPC is particularly well-suited since it is single-shot, allowing for real-time digital synthesis. In addition to further providing quantitative phase, this method is much cheaper to implement than either DIC or PhC, since it requires only the addition of an inexpensive color filter insert or an LED array and no specialized objectives.

Stained and dispersive samples

The cDPC method uses color multiplexing to recover complex-field, making an inherent assumption that the sample is both non-dispersive and colorless. Non-dispersive means that the RI does not change appreciably with wavelength:

$$\boldsymbol{\phi}(\boldsymbol{n}(\lambda), d, \lambda) \approx \boldsymbol{\phi}(\boldsymbol{n}_0, d, \lambda). \tag{2.9}$$

This assumption implies that the optical path length ($\boldsymbol{OPL} = \boldsymbol{n}d$) will remain constant for all measurements. The relative phase delay will always vary with λ (Eq. (2.2)), but this is accounted for in the cDPC algorithm by scaling the transfer functions based on the relative wavelength of each color channel. Unless the dispersion curve is known and the material is assumed to be uniform, one cannot account for dispersive effects in the sample

using the proposed algorithm. However, in practice these effects do not corrupt our phase reconstructions results significantly due to relatively small dispersive effects of water across optical wavelengths.

The second assumption is that the sample is colorless, meaning that the absorption does not have chromatic dependence:

$$\boldsymbol{\mu}(\lambda) \approx \boldsymbol{\mu}_0. \tag{2.10}$$

This is generally valid for unstained biological samples, which are transparent. Color variations due to filter transmission coefficients at different wavelengths are present, but can be removed by the calibration procedure described in Sec. 2.1. Color-dependent absorption, such as that created by stained samples, cannot be recovered and will cause errors in the phase result. In practice, these assumptions limit the applicability of the cDPC method to unstained uncolored samples. However, quantitative phase reveals the mechanical structure of the microenvironment with high contrast, which may eliminate the need for staining in many applications.

2.3 Summary

A single-shot method for quantitative phase and amplitude imaging based on partially-coherent multiplexed color illumination is presented. The inverse algorithm uses a linear approximation to enable fast reconstruction by deconvolution. The hardware requirements are simple, inexpensive and compatible with most commercial microscopes that only need a color camera and a color filter insert placed at the back focal plane of the condenser lens. Unlike phase contrast and DIC, the method does not require special objectives or prisms, reducing hardware costs significantly. In addition, the recovered complex-field can be use to synthesize phase contrast and DIC images digitally, matching the functionality of existing systems at a fraction of the cost. Since the samples are assumed non-dispersive and unstained, this method should be used as an alternative, not in conjunction with, chemical staining.

Chapter 3

Quantitative DPC Microscopy with Computational Aberration Correction

3.1 Algorithmic Aberration Calibration

The concept of *algorithmic self-calibration* – solving jointly for the reconstructed image and the calibration parameters – has proven particularly useful in coherent computational imaging. Examples include probe retrieval in Ptychography [69, 70, 71, 72], source recovery for through-focus phase imaging [73, 74], pupil and source recovery for FPM [75, 76, 77], and calibration-invariant inverse scattering models [78]. The standard approach to self-calibration uses alternating projections (AP), which optimizes multiple variables serially, keeping other parameters fixed during each sub-iteration. The non-convexity of AP provides no guarantee of global convergence, but in practice it works with sufficiently diverse data. Self-calibration of aberrations has been demonstrated previously in an LED array microscope for the cases of through-focus phase [79] and FPM [26, 28, 75, 80, 81], but required a large number of images to be captured. For example, a typical FPM setup [82] uses approximately 5 times as many images as our system to achieve the equivalent resolution.

Here, we propose a method of *algorithmic aberration calibration* for DPC microscopy [30, 32, 33, 83], where we avoid the need for pre-calibration by jointly recovering both the sample's complex-field *and* the spatially-varying aberrations of the system, directly from raw images[1]. We present an AP framework that uses 4 captured images for simultaneous phase retrieval and digital correction of spatially-varying aberrations (Fig. 3.1). Three of the measurements are partially-coherent conventional DPC images (with rotated half-circle sources); these provide good phase contrast, but poor aberration contrast. The fourth image uses single-LED (spatially coherent) illumination; this provides aberration contrast, but alone cannot resolve the ambiguity between complex-field and pupil aberration [84]. Using both partially-coherent and coherent images together improves sensitivity to aberrations without sacrificing the ben-

[1]This work was performed in close collaboration with Zachary F. Phillips (Waller Lab, EECS, UC Berkeley).

efits of partial coherence. We model the aberrations parametrically (with a Zernike basis [85, 79]) to dramatically reduce the number of unknowns. In addition, by segmenting the FoV, we are able to recover and digitally correct for spatially-varying aberrations across the FoV.

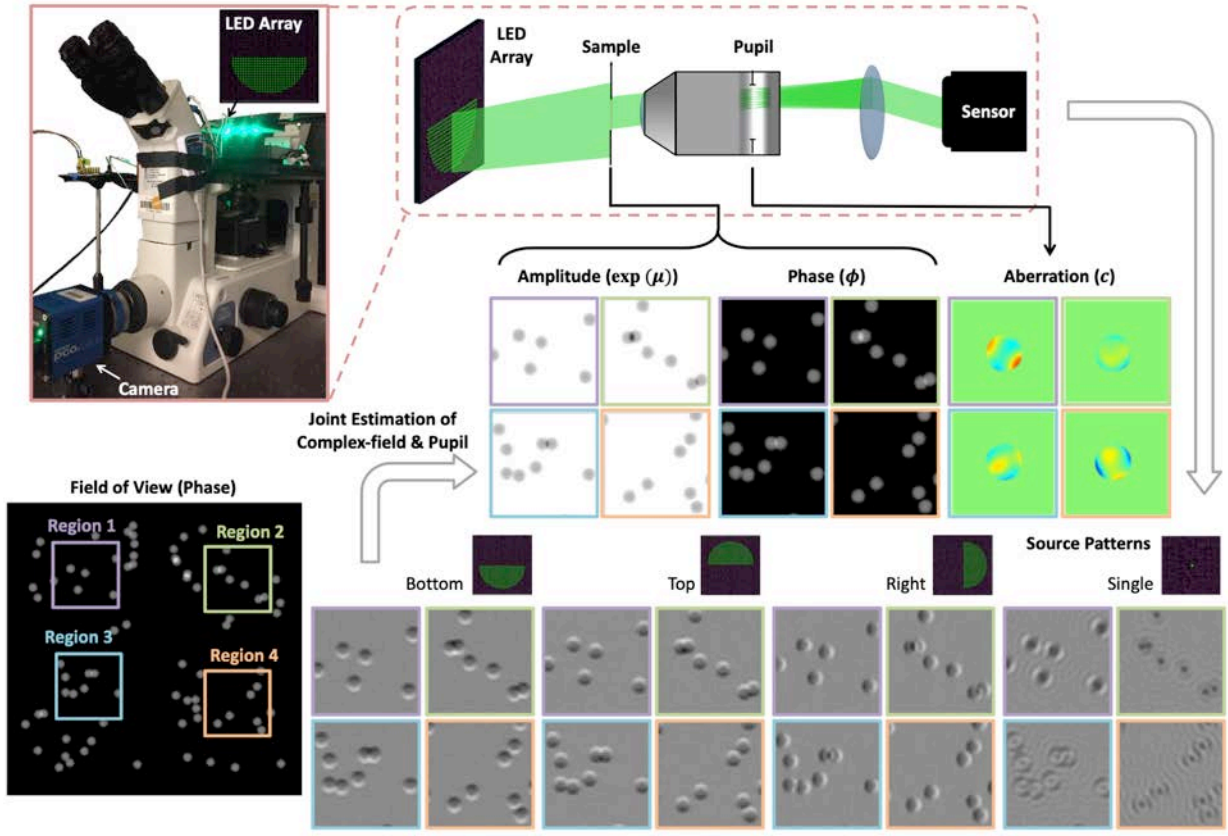

Figure 3.1: Our LED array microscope captures 4 images with different illumination source patterns (three half-circles and one single LED). The intensity images are used to simultaneously reconstruct both amplitude and phase of the sample, and to estimate the pupil aberrations at each spatial location, which are then digitally corrected for. We show reconstructions for 4 regions with different spatially-varying aberrations.

3.2 Joint Estimation of Complex-Field and Aberrations

Our LED array microscope and data capture scheme is shown in Fig. 3.1. Quantitative DPC (without aberration correction) requires a minimum of 3 intensity measurements to reconstruct phase [86], though only two quantities (amplitude and phase) are reconstructed at each pixel. Hence, there is significant redundancy in the data which may, in principle,

be used to solve for aberrations. However, intensity images formed by partially-coherent illumination do not exhibit significant aberration contrast. Hence, we modify the capture scheme to add one additional measurement with spatially-coherent illumination (a single on-axis LED). The example in Fig. 3.1 has a different aberration in each quadrant of the FoV, and only the single-LED image displays visible differences in contrast for each region. An off-axis LED would also provide the necessary coherent contrast, but the on-axis LED provides higher intensity and better SNR. Having achieved both phase and aberration contrast with 1 on-axis and 3 half-circle sources, we use this dataset to jointly recover both spatially-varying aberrations and the complex-field of the sample (with resolution set by the incoherent diffraction limit).

The process of estimating the sample's complex-field and the system's aberrations simultaneously is a joint estimation large-scale nonlinear non-convex problem. To simplify, DPC typically makes a weak scattering approximation which linearizes the forward model. This approximation is generally valid for optically thin or index-matched samples, like biological cells. Intensity measurements can then be related to absorption ($\boldsymbol{\mu}$) and phase ($\boldsymbol{\phi}$) of the sample by simple convolutions, which is described in Chapter 2. As derived in Appendix A.1, the DPC forward model in matrix form is:

$$\boldsymbol{I}_{\mathrm{n}} = \mathbf{F}^{-1}\left(\mathrm{diag}(\boldsymbol{H}_{\mu})\mathbf{F}\boldsymbol{\mu} + \mathrm{i}\cdot\mathrm{diag}(\boldsymbol{H}_{\phi})\mathbf{F}\boldsymbol{\phi}\right) \ . \tag{3.1}$$

Here, $\mathrm{diag}(\boldsymbol{x})$ denotes a diagonal matrix with diagonal values $\boldsymbol{x}$, $\mathbf{F}$ and $\mathbf{F}^{-1}$ represent the DFT and inverse DFT matrices, $\boldsymbol{I}_{\mathrm{n}}$ is the vectorized normalized measured intensity (with the DC term subtracted), and $\boldsymbol{H}_{\mu}$ and $\boldsymbol{H}_{\phi}$ are vectorized transfer functions for absorption and phase. If the source satisfies the Köhler illumination configuration, the transfer functions can be numerically evaluated based on Eq. (1.18) and the cross-correlation property of Fourier transforms:

$$\boldsymbol{H}_{\mu} = \frac{1}{\boldsymbol{I}_{\mathrm{o}}}\left[\mathbf{F}^{-1}\mathrm{diag}(\boldsymbol{O}^{*})\mathbf{F} + \mathbf{F}^{-1}\mathrm{diag}(\mathbf{F}^{*}\boldsymbol{P}^{*})\mathbf{F}\mathrm{diag}(\boldsymbol{S})\right]\boldsymbol{P} \tag{3.2}$$

$$\boldsymbol{H}_{\phi} = \frac{1}{\boldsymbol{I}_{\mathrm{o}}}\left[\mathbf{F}^{-1}\mathrm{diag}(\boldsymbol{O}^{*})\mathbf{F} - \mathbf{F}^{-1}\mathrm{diag}(\mathbf{F}^{*}\boldsymbol{P}^{*})\mathbf{F}\mathrm{diag}(\boldsymbol{S})\right]\boldsymbol{P} \ , \tag{3.3}$$

where $*$ is the complex conjugate operation, $\boldsymbol{I}_{\mathrm{o}}$ is the total intensity of the source passing through the system, $\boldsymbol{S}$ and $\boldsymbol{P}$ are the vectorized source and pupil, and $\boldsymbol{O} = \mathbf{F}\mathrm{diag}(\boldsymbol{S})\boldsymbol{P}$. Typically, the space-invariant exit pupil $\boldsymbol{P}$ is a circular function, $\mathrm{Circ}(\lambda\boldsymbol{u}/\mathrm{NA})$, with its radius determined by system NA, and wavelength, λ. The phase of $\boldsymbol{P}$ is the pupil aberration we wish to recover, modeled as a weighted sum of Zernike modes on spatial frequency coordinate ($\boldsymbol{u}$) [85]:

$$\boldsymbol{P}(\boldsymbol{c}) = \mathrm{Circ}\Big(\frac{\lambda\boldsymbol{u}}{\mathrm{NA}}\Big)\prod_{m=0}^{M} e^{\mathrm{i}c_m\boldsymbol{Z}_m} \ , \tag{3.4}$$

where M is the total number of Zernike modes and $\boldsymbol{c}$ contains the coefficients, c_m, of each orthogonal mode $\boldsymbol{Z}_m$. To recover spatially-varying aberrations, we solve for individual pupil

aberrations at different disjoint spatial regions across the FoV and assume the aberrations are locally space-invariant within each region. Given Eqs. (3.1)-(3.4), an objective function for the joint optimization of absorption, phase and pupil aberrations can be formulated as:

$$\min_{\boldsymbol{\mu},\boldsymbol{\phi},\boldsymbol{c}} \sum_{s=1}^{N_s} \left\| \mathbf{F}\boldsymbol{I}_{\mathrm{n},s} - \operatorname{diag}\left(\boldsymbol{H}_{\mu,s}(\boldsymbol{c})\right)\mathbf{F}\boldsymbol{\mu} - \mathrm{i}\cdot\operatorname{diag}\left(\boldsymbol{H}_{\phi,s}(\boldsymbol{c})\right)\mathbf{F}\boldsymbol{\phi} \right\|_2^2 + \tau\mathcal{R}(\boldsymbol{\mu},\boldsymbol{\phi}) \;, \tag{3.5}$$

where s is the measurement index of each corresponding source pattern, N_s is the total number of measurements, $\|\cdot\|_2$ represents an ℓ_2 norm, τ is a regularization parameter and $\mathcal{R}$ is a regularization term that helps mitigate noise artifacts. It is inferred from Eq. (3.5) that the aberration coefficients $\boldsymbol{c}$ are coupled with both $\boldsymbol{\mu}$ and $\boldsymbol{\phi}$, so simultaneously optimizing all variables does not guarantee convergence. An alternating projections update strategy instead provides a non-divergence guarantee, as was previously used for phase-from-focus joint source recovery [74]. Similarly, we iteratively solve for both the complex object and system aberrations as two sub-problems.

Our alternating projections algorithm initializes the Zernike coefficients, $\boldsymbol{c}$, with zero. At the start of one iteration, $\boldsymbol{c}$ are fixed and a DPC deconvolution sub-procedure (Sec. 3.2) is performed in order to update the estimates of amplitude, $\exp(\boldsymbol{\mu})$, and phase, $\boldsymbol{\phi}$. This new complex-field estimate is then held fixed while an aberration estimation procedure (Sec. 3.2) is performed. After updating the aberration estimate based on this procedure, a new iteration begins. Eventually, the objective function converges to a stationary point, giving the final estimates of amplitude, phase, and aberration coefficients. In general, this optimization strategy works as long as there exist enough diversity and redundancy in the measurements.

DPC phase retrieval sub-procedure

The phase retrieval sub-procedure amounts to solving the conventional DPC inverse problem as introduced in Sec. 1.3, except that it incorporates the current estimate of the Zernike coefficients $\boldsymbol{c}_k$ at iteration k:

$$\boldsymbol{\mu}_{k+1},\boldsymbol{\phi}_{k+1} = \arg\min_{\boldsymbol{\mu},\boldsymbol{\phi}} \sum_{s=1}^{N_s} \left\| \mathbf{F}\boldsymbol{I}_{\mathrm{n},s} - \operatorname{diag}\left(\boldsymbol{H}_{\mu,s}(\boldsymbol{c}_k)\right)\mathbf{F}\boldsymbol{\mu} - \mathrm{i}\cdot\operatorname{diag}\left(\boldsymbol{H}_{\phi,s}(\boldsymbol{c}_k)\right)\mathbf{F}\boldsymbol{\phi} \right\|_2^2 + \tau\mathcal{R}(\boldsymbol{\mu},\boldsymbol{\phi}) \;. \tag{3.6}$$

The regularization term, $\mathcal{R}$, should be chosen based on *a priori* information about the sample. For instance, Tikhonov regularization can mitigate noise, and the solution of Eq. (3.6) can then be found using a non-iterative deconvolution [86]. If the gradients of the object are relatively sparse, the TV regularizer can be used to reduce noise without degrading edges. Since the regularization term for TV is not differentiable, iterative algorithms for solving Eq. (3.6) are needed. In this paper, we use the ADMM to implement TV regularization [44], typically requiring about 20 iterations.

Aberration recovery sub-procedure

The aberration recovery sub-procedure uses a nonlinear optimization algorithm to update the aberration estimate based on the newly updated complex-field, which is held fixed. The sub-procedure is initialized with the Zernike coefficients estimate from the previous iteration, $\boldsymbol{c}_k$. Mathematically, the sub-procedure problem is written as:

$$\boldsymbol{c}_{k+1} = \arg\min_{\boldsymbol{c}} \sum_{s=1}^{N_s} \left\| \mathbf{F}\boldsymbol{I}_{\mathrm{n},s} - \mathrm{diag}\left(\boldsymbol{H}_{\mu,s}(\boldsymbol{c})\right)\mathbf{F}\boldsymbol{\mu}_{k+1} - \mathrm{i}\cdot\mathrm{diag}\left(\boldsymbol{H}_{\phi,s}(\boldsymbol{c})\right)\mathbf{F}\boldsymbol{\phi}_{k+1} \right\|_2^2 . \tag{3.7}$$

Equation (3.7) may be solved by a gradient descent (first-order optimization) approach, or more sophisticated second-order optimization routines (*e.g.* Newton's method [74]). All of these require computation of the gradient of the objective function with respect to $\boldsymbol{c}$. If we define the cost function as $f = \sum_{s=1}^{N_s} \|\boldsymbol{\varepsilon}_s\|_2^2$, in which $\boldsymbol{\varepsilon}_s = \mathbf{F}\boldsymbol{I}_{\mathrm{n},s} - \mathrm{diag}(\boldsymbol{H}_{\mu,s})\mathbf{F}\boldsymbol{\mu}_{k+1} - \mathrm{i}\cdot\mathrm{diag}(\boldsymbol{H}_{\phi,s})\mathbf{F}\boldsymbol{\phi}_{k+1}$ is the residual vector, the gradient becomes $\nabla_{\boldsymbol{c}} f = \sum_{s=1}^{N_s} \left[\partial\boldsymbol{\varepsilon}_s/\partial\boldsymbol{c}\right]^{\mathrm{H}} \boldsymbol{\varepsilon}_s$, where H denotes Hermitian transpose. Using Eqs. (3.2)-(3.4), the gradient can be calculated analytically as:

$$\begin{aligned}\nabla_{\boldsymbol{c}} f = \frac{\mathrm{i}}{\boldsymbol{I}_{\mathrm{o}}}\mathbf{Z}^{\mathrm{T}}\mathrm{diag}(\boldsymbol{P}^*)\sum_{s=1}^{N_s}\Big[&\mathbf{F}^{-1}\mathrm{diag}(\boldsymbol{O}_s)\mathbf{F}\left[\mathrm{diag}(\mathbf{F}^*\boldsymbol{\mu}_{k+1}^*) - \mathrm{i}\ \mathrm{diag}(\mathbf{F}^*\boldsymbol{\phi}_{k+1}^*)\right] + \\ &\mathrm{diag}(\boldsymbol{S}_s)\mathbf{F}^{-1}\mathrm{diag}(\mathbf{F}\boldsymbol{P})\mathbf{F}\left[\mathrm{diag}(\mathbf{F}^*\boldsymbol{\mu}_{k+1}^*) + \mathrm{i}\ \mathrm{diag}(\mathbf{F}^*\boldsymbol{\phi}_{k+1}^*)\right]\Big]\boldsymbol{\varepsilon}_s\ .\end{aligned} \tag{3.8}$$

In this gradient, T denotes transpose and the Zernike basis, $\mathbf{Z}^{\mathrm{T}} = [\boldsymbol{Z}_0, \boldsymbol{Z}_1, \ldots, \boldsymbol{Z}_M]^{\mathrm{T}}$, contains a finite number of modes where $\boldsymbol{Z}_0 - \boldsymbol{Z}_M$ are the vectorized Zernike modes. For efficient computation, we adopt the L-BFGS algorithm [87] and use the gradient in Eq. (3.8) to solve this nonlinear optimization problem, which generally takes ~ 10 iterations to converge.

3.3 Simulation Results

To verify the performance of our joint estimation framework, we show simulation results in Fig. 3.2. The system parameters were chosen to match our experimental setup (0.4NA, wavelength $0.514\mu m$, 177 source LEDs), with the LED array placed sufficiently far away from the sample such that the illumination from each LED is effectively spatially coherent (plane wave) [26, 28, 88].

We compare our results with joint phase and aberration recovery FPM in Fig. 3.2. FPM captures a separate image for each of the 177 LEDs, whereas DPC requires only 4 images to reconstruct the same quantities. FPM intensity images are simulated by using different tilted plane wave illuminations corresponding to each single LED. All the intensity images contain

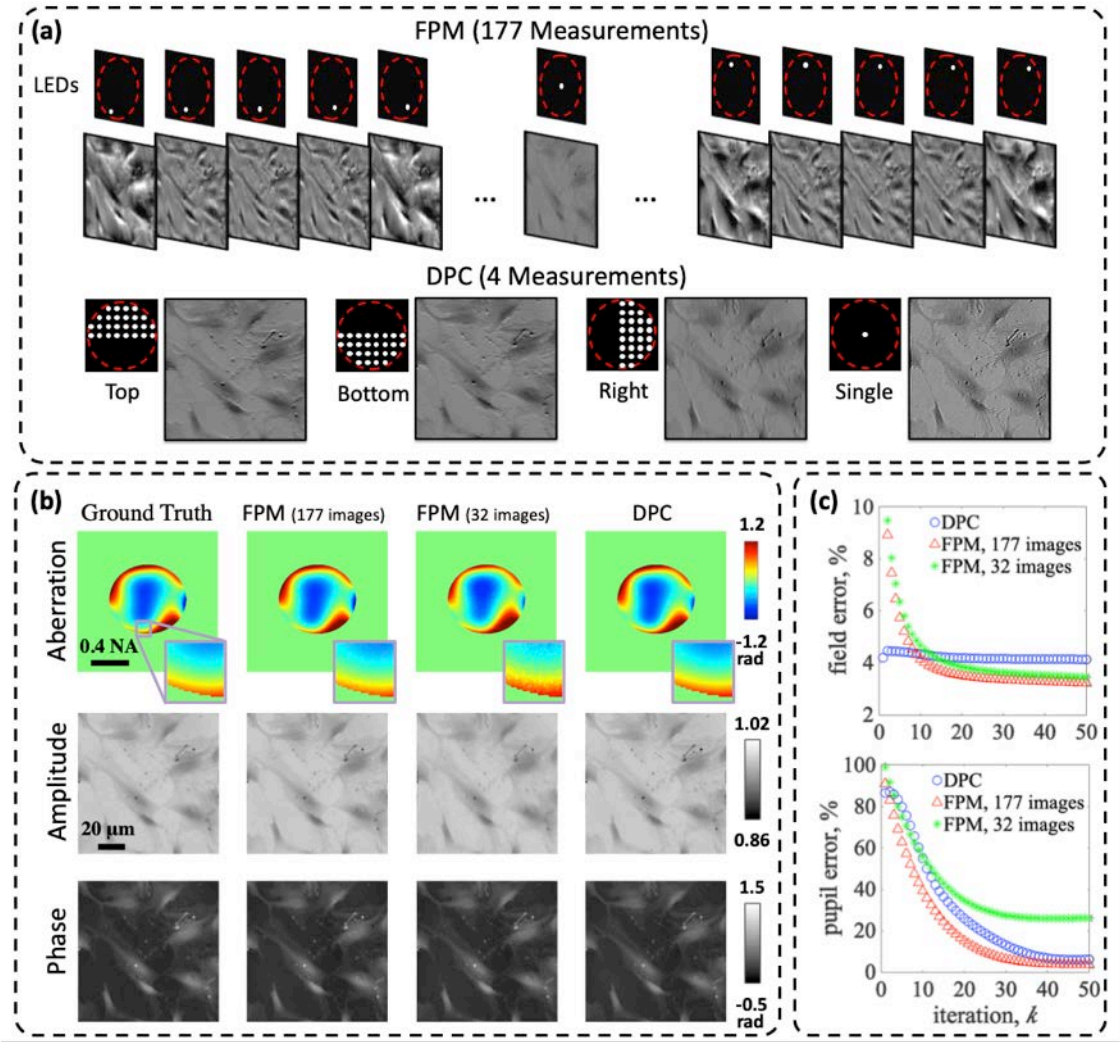

Figure 3.2: Performance of joint phase and aberrations estimation on a simulated dataset. (a) Simulated FPM and DPC measurements. Red dashed circles indicate the NA of the objective lens. (b) Joint estimation of optical field and pupil aberrations, comparing ground truth, FPM and DPC measurements. (c) Errors for complex-field and aberrations at each iteration.

the same pupil aberration, which is a weighted sum of the first 18 Zernike modes excluding piston and tilts. Our simulated DPC measurements are the sum of the intensity images from half-circle blocks of LEDs on the top, bottom, or right regions of the LED array [32]. For all measurements, we added synthesized noise using a Poisson distribution with a mean of $\sim$3000 photons per pixel. Equation (3.5) was then solved with ℓ_2 regularization using the 4 DPC images, while we implemented the same algorithm in [89] to recover complex-field and aberrations using FPM with the full 177 image dataset. In this setup, FPM could use

as few as 32 images (illuminations from the outer-most annular LEDs only) to achieve the same spatial frequency coverage as our DPC method. Therefore, we also include the results of FPM with 32 measurements for comparison.

Reconstructions from both FPM and our DPC algorithm match the ground truth as shown in Fig. 3.2(b); however, our method only requires 4 measurements, reducing acquisition time and memory requirements. Figure 3.2(c) plots the normalized root-mean-square error ($\|\boldsymbol{x} - \boldsymbol{x}_{\text{true}}\|_2 / \|\boldsymbol{x}_{\text{true}}\|_2$) at each iteration for both complex-field and pupil aberrations. FPM incurs lower complex-field error than DPC, likely due to both the weak scattering approximation and the larger dataset. As for the pupil aberration error, FPM performance varies significantly with dataset size. While FPM with the full dataset outperforms the proposed DPC framework, our method provides a better result than FPM with 32 images. This is because FPM with fewer measurements has lower effective SNR, adding noise to the recovered pupil aberration (inset of Fig. 3.2(b)). Our method requires significant computation since it solves two optimization problems at each iteration, but the computation time is comparable to a sequential FPM reconstruction. Both methods were implemented in MATLAB on a desktop computer (Intel Core i7 CPU, Nvidia Tesla C2075 GPU). With a 650×584 pixel object, each iteration took 2.2s for FPM and 2.5s for our DPC algorithm.

3.4 Experimental Results

Experimentally, we use an LED array microscope with the illumination module replaced with a custom-built LED array ($\lambda = 0.514\mu m$) [32, 28]. A phase target (Benchmark Technologies), which contains periodic patterns of continuous spatial frequencies, is imaged by a 20× 0.4NA objective lens (Nikon, CFI Plan Achro) in a Nikon TE300 microscope and images are recorded by a PCO.edge 5.5 sCMOS camera on the front port of the microscope (which adds 2× magnification). To test the weak phase gradient assumption, phase images of 6 resolution targets of different heights are recovered using DPC. After validating the reconstructed phase values against theoretical ones, we find that DPC provides accurate results when the phase of the sample is below 0.64 radians, then underestimates the phase values due to breakdown of the approximation. We collect 177 measurements by scanning individual LEDs within a maximum 0.4NA illumination angle. To provide a fair comparison between FPM and DPC, we use the same measurements to synthesize the 4 images for our method. As shown in Fig. 3.3(a), DPC measurements with half-circle source patterns have high resolution and qualitatively reveal the phase gradients of the sample, while measurements with single-LED illumination have lower resolution. Two single-LED image zoom-ins that contain the same structure at different orientations are shown in Fig. 3.3(a). One has high contrast, while the other does not, because of directional aberrations. By processing the images using the FPM algorithm and the proposed method with TV regularization, we recover the phase of the sample as shown in Fig. 3.3(b). The FPM and DPC reconstructions are similar, and can resolve features with period as small as $\lambda / (2 \times \text{NA}) = 0.643\mu m$. In addition, both results provide reliable quantitative phase of the sample. The RI of the binary phase target

is 1.52, with height of $100nm$, resulting in $\sim$0.64 radians peak-to-valley. Looking at the 1D cut-lines (taken along dashed lines) in Fig. 3.3(b), after subtracting the mean of each, the reconstructions show good agreement with the ideal height.

Pupil aberrations recovered by both FPM and DPC algorithms are in Fig. 3.3(c). While we have no ground truth, aberrations estimated from FPM and DPC match well within the 4^{th} radial degree of Zernike modes. The dominant aberration in the objective lens is the 8^{th} Zernike mode (horizontal coma); this agrees with the evidence of directional aberrations mentioned above and results in orientation-dependent resolution. One reason causing a difference between the reconstructed pupils is the high-frequency fluctuation shown in the pupil aberration from FPM, which does not exist in the low-order Zernike modes. Although high-order aberrations might be estimated with more measurements to avoid overfitting, it's usually enough to improve image quality by correcting the low-order aberrations.

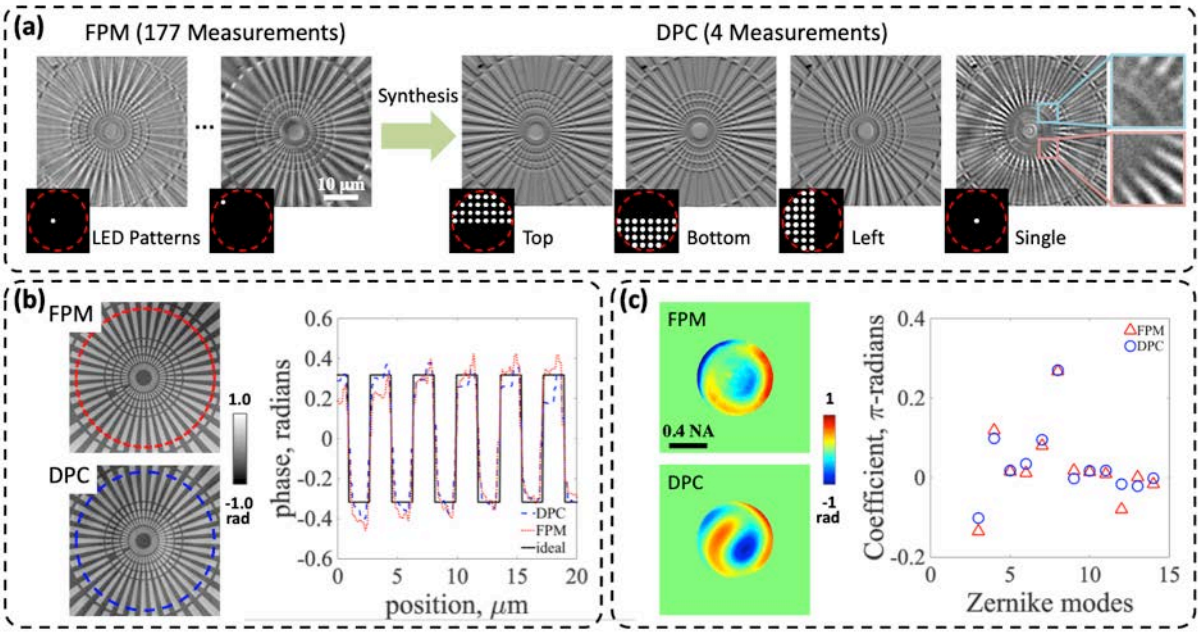

Figure 3.3: (a) Experimental FPM and DPC measurements for different LED source patterns. Zoomed regions at different orientations for coherent illumination are marked in cyan and pink boxes, respectively. (b) Quantitative phase of a star target using FPM and DPC, along with 1D cutlines for FPM (red) and DPC (blue) along the dashed lines. (c) Reconstructed wavefront error function and the weights of each Zernike mode up to the 4^{th} radial degree.

To quantify the performance of our method, we introduced known defocus aberrations using an axial motion stage (Thorlabs, MZS500-E). We translated the phase test target across a range of known axial steps over a total range of $40\mu m$. Each $2\mu m$ of translation, the 4 images for our method were acquired using a $10\times$ 0.25NA objective lens (Nikon, CFI

Plan Achro) at an acquisition rate of 20Hz. Quantitative phase reconstructions assuming zero aberration, aberration-corrected phase images and the recovered aberrations are shown in Fig. 3.4(a). With increased defocus, the uncorrected phase results degrade. Though our method also suffers from resolution degradation at large defocus distances ($\pm 20\mu m$), it provides better resolution than the uncorrected phase retrieval. For example, in Fig. 3.4(b) the numbers in group 9 are resolved with pupil correction, while they are not readable in the uncorrected result.

We can also recover the focus distances from the defocus term of the Zernike modes and compare the estimated defocus values to known values (Fig. 3.4(c)). Since the Zernike basis is normalized in a range from -1 to 1, the defocus value, d, at each time point, t, can be evaluated as $d(t) = c_4(t) \times \lambda/\pi/(1-(1-\mathrm{NA}^2)^{0.5})$. As expected, the predicted pupil aberrations have quadratic form, which indicates that defocus dominates. Experimentally, our method overestimates defocus values by a factor of 1.16. This discrepancy might originate from mis-calibration of the experiment or parameters used in computation (*e.g.* wavelength, NA of the objective lens, precision of the motion stage). This linear relationship between the predicted positions and the true focus holds when the magnitude of defocus is less than 16 μm, $\sim 2\times$ DoF. However, the accuracy of aberration correction drops as the defocus value exceeds $2\times$ DoF, when the maximum phase difference in the pupil becomes larger than 2π and the algorithm becomes more likely to converge to a local minimum. From these experiments, we conclude that our method accurately estimates time-varying aberrations, which not only enables phase retrieval with digital focusing but can also be applied to improve phase recovery with moving objects/background.

Our method is easily extended to account for spatially-varying aberrations, simply by solving the joint estimation problem separately over different patches of the FoV. In order to visualize spatially-varying aberrations, we prepared oil (Cargille, $\mathrm{n_D} = 1.58$) immersed $10\mu m$ polystyrene beads (Sigma-Aldrich) as our sample, which is assumed to be nearly spatially invariant. The sample was imaged by a $4\times$ 0.2NA objective lens (Nikon, CFI Plan Apo Lambda) that has a FoV of 1.7 $\times$ 2.1mm. Four images were captured at 12.5Hz using the same source patterns as in Fig. 3.3(a). Field-dependent aberrations are primarily caused by two types of system imperfections. First, the incident angle of individual LEDs changes from one FoV to another, since the relative position between the LEDs and the sample at each FoV varies. Second, there exist spatially-varying aberrations native to the optical system. To accommodate this spatial variance, we break the full FoV into small patches, and apply the joint estimation algorithm on each patch independently. In this case, the incident angle of individual LEDs and the aberrations are assumed invariant within the patch, which is usually valid when the region is much smaller than the total FoV. In Fig. 3.5(a), the full FoV is divided into 100 patches. Within each patch, the absorption, phase and pupil aberration were recovered independently before being stitched together to form the full FoV images. In practice, optimization for each patch converges in $20-30$ iterations.

Looking at the aberrations recovered, the center of the FoV is essentially aberration-free, which is consistent with the fact that optical systems are usually optimized there. Therefore, the absorption and phase images with pupil recovery are similar to that without aberration

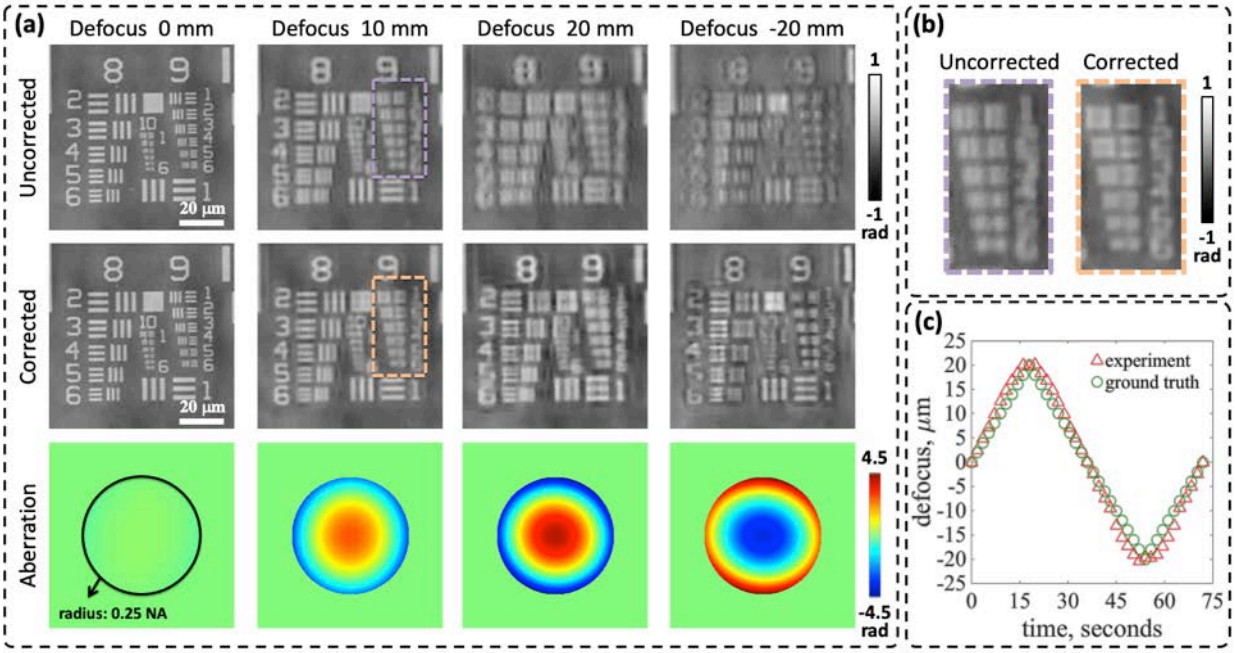

Figure 3.4: (a) Quantitative phase reconstructions of a USAF 1951 resolution target at various defocus distances with and without aberration correction, and the corresponding recovered aberrations. (b) Zoomed-in reconstructions at defocus of $10\mu m$. (c) Known and experimentally-estimated defocus values from the 4^{th} Zernike mode over time.

correction. Aberrations are much stronger along the edges of the FoV, where the field curvature blurs the image. Consequently, obvious differences occur between the normal DPC and aberration-corrected DPC reconstructions at those patches. The recovered amplitude (absorption) at the bottom right corner is dramatically changed after applying aberration correction. Qualitatively, the uncorrected absorption at the edge of the field appears to contain some phase information, leading to a shadow-like appearance; these artifacts are removed with pupil recovery. In addition, while aberrated phase evaluated with Tikhonov deconvolution suffered from high-frequency noise, phase with pupil correction shows reduced noise due to the use of TV regularization.

3.5 Summary

In computational imaging systems, aberrations can significantly degrade complex-field reconstructions if not properly compensated for. In order to correct aberrations without pre-calibration, we propose joint estimation of the sample and the pupil aberration. Our DPC-based phase retrieval technique simultaneously recovers the system pupil aberration and quantitative phase and absorption of the sample from only 4 intensity images. By

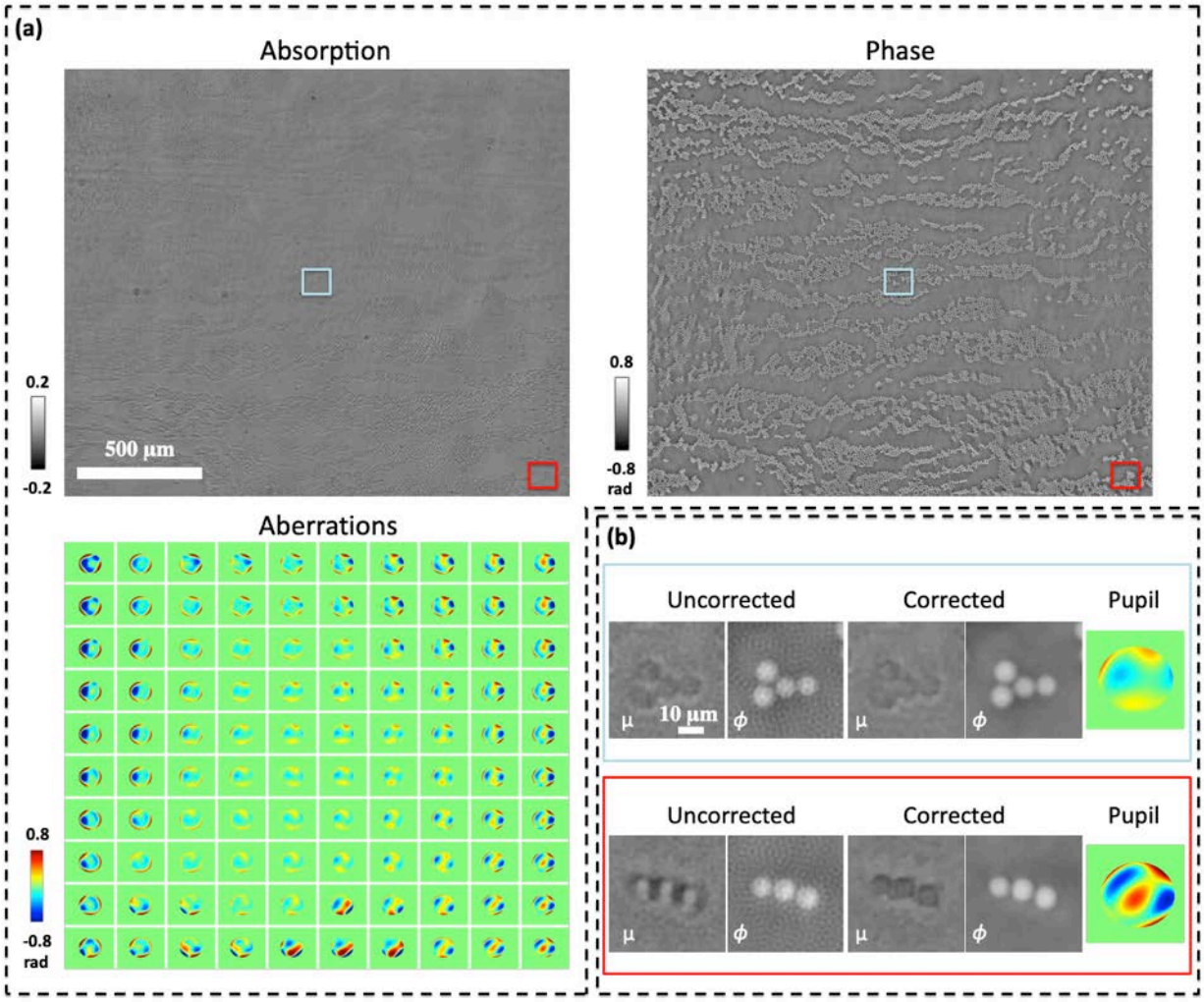

Figure 3.5: (a) Reconstructed absorption, phase and spatially-varying aberrations (recovered pupil wavefronts for different regions of the field-of-view). (b) Comparison of results with and without pupil estimation for central and edge regions of the field-of-view.

combining 3 half-circle source pattern measurements and 1 made under spatially coherent (single-LED) illumination, diffraction-limited complex-field and aberration Zernike coefficients were recovered through an alternating projections non-convex optimization. This method not only reduces the data acquisition time, but also increases the SNR due to higher light throughput compared to single-LED acquisition, which should aid in imaging dynamic biological samples. The recovered system aberrations are general to the system, and may be used for image correction in other subsequent imaging modalities on the same microscope, such as deconvolution of fluorescence images [81].

Chapter 4

3D Phase Imaging with Differential Phase Contrast

4.1 3D Phase Imaging using Partial Coherent Illumination

Although one can digitally back-propagate a measured 2D complex-field to refocus, this does not provide the optical sectioning capabilities of true 3D imaging. Phase being a projected quantity means that one cannot simply measure 2D phase at different focus planes to reconstruct 3D phase with coherent illumination. Partially coherent imaging, however, provides a distinct focus plane and optical depth sectioning. Hence, with partially coherent light, one can use 2D phase retrieval at multiple focus planes to reconstruct 3D RI. Previous 3D phase imaging [52] used defocus with *temporal* partial coherence for sectioning. On the other hand, *spatial* partial coherence also creates depth sectioning, and through-focus measurements with spatial partial coherent illumination can then be used to solve the 3D phase retrieval problem. In this chapter, a 3D DPC method is presented that recovers 3D absorption and RI from intensity images taken at different focus planes with each of the 4 half-circle source patterns (Fig. 4.1). In order to properly account for out-of-focus contributions, a full 3D model is derived, rather than solving for 2D phase independently at each focus plane. In order to formulate a linear inverse problem, we consider only weak scattering (1^{st} Born/Rytov approximation) [11, 90, 91, 92]. As a result, efficient inverse algorithms that solves for 3D RI directly from the intensity measurements become possible, without an intermediate phase retrieval step. Finally, we explore the use of priors for mitigating both out-of-focus and halo artifacts. The resulting non-interferometric 3D quantitative phase imaging method is simple to implement in a commercial microscope, achieves the incoherent resolution limit ($2\times$ the coherent resolution limit) and is accurate for most biological samples.

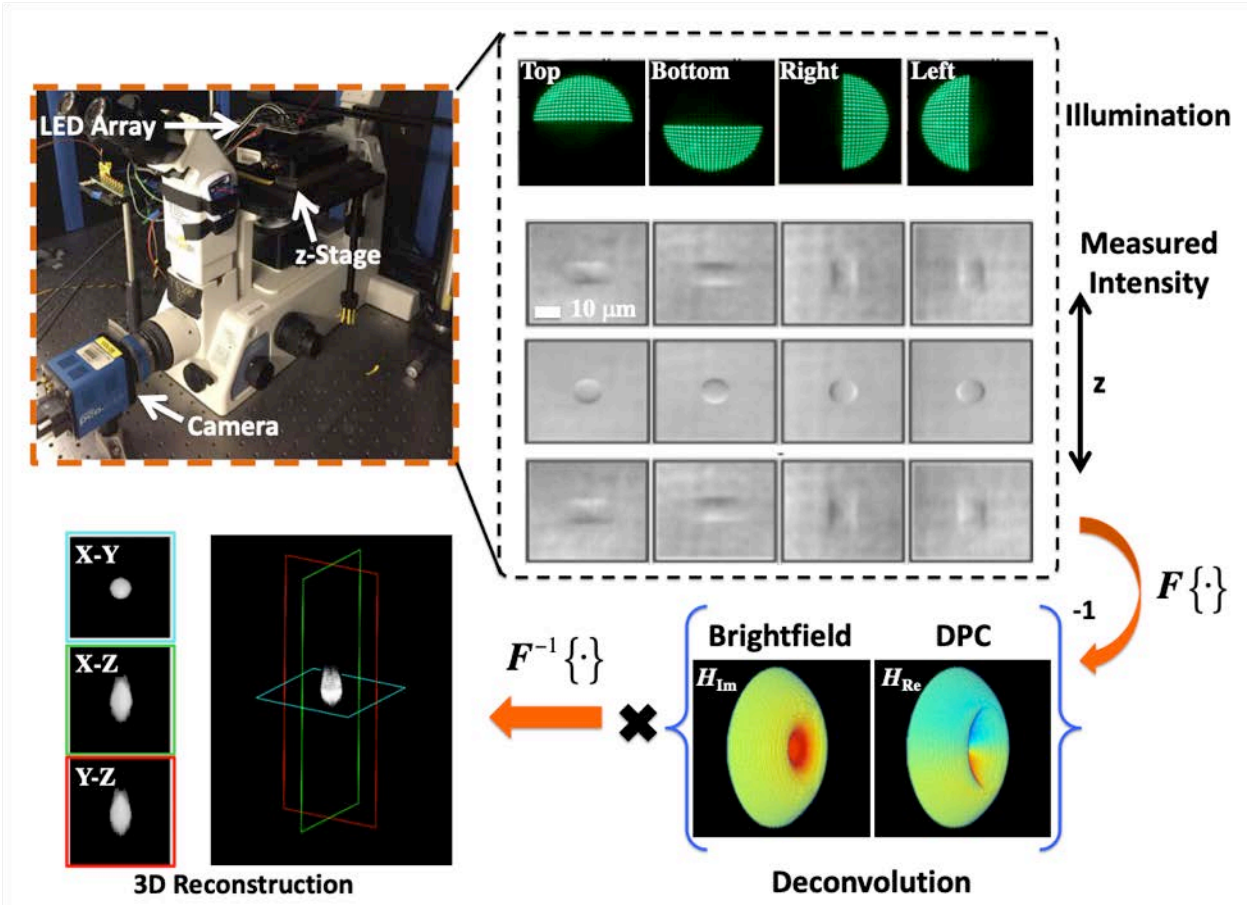

Figure 4.1: 3D Differential Phase Contrast (DPC) microscopy. The setup is a microscope equipped with LED array illumination and an axial motion stage. Through-focus intensity stacks are captured using 4 source patterns (top, bottom, right, and left half-circles). The intensity data is related to the 3D RI distribution by illumination-dependent transfer functions, according to the 1st Born approximation. A deconvolution algorithm then recovers the 3D complex RI.

4.2 Principles of 3D DPC Microscopy

Forward model

A 3D sample can be characterized by its scattering potential $\boldsymbol{V}(\boldsymbol{r}) = k_o^2(n_\mathrm{b}^2 - \boldsymbol{n}^2(\boldsymbol{r}))$ [11], where n_b is the RI of the surrounding media and $\boldsymbol{n} = \boldsymbol{n}_\mathrm{Re} + \mathrm{i}\boldsymbol{n}_\mathrm{Im}$ is the sample's complex RI. The real part of the RI, $\boldsymbol{n}_\mathrm{Re}$, describes how phase delays accumulate as light passes through the sample, while the imaginary part, $\boldsymbol{n}_\mathrm{Im}$, describes absorption. For weakly scattering objects, multiple-scattering is negligible and the total field can be approximated by the sum

of the incident field and the single-scattered field as in Eq. (1.6),

$$\boldsymbol{U}_{\text{tot}}(\boldsymbol{r}) \approx \boldsymbol{U}_{\text{in}}(\boldsymbol{r}) + \iiint \boldsymbol{U}_{\text{in}}(\boldsymbol{r}')\boldsymbol{V}(\boldsymbol{r}')\boldsymbol{G}(\boldsymbol{r}-\boldsymbol{r}')\mathrm{d}^3\boldsymbol{r}'. \tag{4.1}$$

Next, quasi-monochromatic (with wavelength λ) spatially partial coherent illumination from an extended source in Köhler geometry is considered. Each point on the source generates a distinct plane wave at the sample described by $\boldsymbol{U}_{\text{in}}(\boldsymbol{\rho}, z) = e^{-\mathrm{i}2\pi(\boldsymbol{u}'\cdot\boldsymbol{\rho}+\eta' z)}$, where $\boldsymbol{u}'$ and η' are frequencies determining the propagation direction in 3D space and $\|\boldsymbol{u}'\|_2^2 + \eta'^2 = \lambda^{-2}$. After passing through the sample, the field is low-pass filtered by the pupil function $\boldsymbol{P}(\boldsymbol{u})$ of the microscope, corresponding to the 2D coherent point spread function $\boldsymbol{h}(\boldsymbol{\rho})$. The measured intensity $\boldsymbol{I}_{\text{img}}(\boldsymbol{\rho}, z)$ is the incoherent sum of intensities from each point source. With 1st Born approximation and Eq. (4.1), the measured intensity is

$$\boldsymbol{I}_{\text{img}}(\boldsymbol{\rho}, z) = \iint \boldsymbol{S}(\boldsymbol{u}')\Big|\Big[\boldsymbol{U}_{\text{in}}(\boldsymbol{\rho}, z) + \Big(\boldsymbol{U}_{\text{in}}(\boldsymbol{\rho}, z)\boldsymbol{V}(\boldsymbol{\rho}, z)\Big) \otimes_{3\text{D}} \boldsymbol{G}(\boldsymbol{\rho}, z)\Big] \otimes_{3\text{D}} \boldsymbol{h}(\boldsymbol{\rho})\Big|^2 \mathrm{d}^2\boldsymbol{u}', \tag{4.2}$$

where $\otimes_{3\text{D}}$ is the 3D convolution operator, $\boldsymbol{\rho}$ denotes 2D transverse coordinates, and z the axial coordinate, with its origin at the focal plane of the microscope. The 2D intensity distribution of the source is described by $\boldsymbol{S}(\boldsymbol{u}')$. In practice, only 2D intensity can be measured from a single image. Thus, scanning the sample through z and capture images at many focus planes is needed in order to build up the 3D intensity measurement on the left side of Eq. (4.2). Taking a 3D Fourier transform $\tilde{\cdot}$ of both sides of Eq. (4.2) shows a Fourier space relation between the 3D measured intensity spectrum and the scattering potential,

$$\begin{aligned}\tilde{\boldsymbol{I}}_{\text{img}}(\boldsymbol{u}, \eta) = \iint \boldsymbol{S}(\boldsymbol{u}')\Big[\boldsymbol{P}(\boldsymbol{u})\Big(\boldsymbol{\delta}(\boldsymbol{u}+\boldsymbol{u}', \eta+\eta') + \tilde{\boldsymbol{V}}(\boldsymbol{u}+\boldsymbol{u}', \eta+\eta')\tilde{\boldsymbol{G}}(\boldsymbol{u}, \eta)\Big)\Big] \otimes_{3\text{D}} \\ [\boldsymbol{P}^*(-\boldsymbol{u})\Big(\boldsymbol{\delta}(\boldsymbol{u}-\boldsymbol{u}', \eta-\eta') + \tilde{\boldsymbol{V}}^*(\boldsymbol{u}'-\boldsymbol{u}, \eta'-\eta)\tilde{\boldsymbol{G}}^*(-\boldsymbol{u}, -\eta)\Big)\Big]\mathrm{d}^2\boldsymbol{u}',\end{aligned} \tag{4.3}$$

where $\boldsymbol{u}$ denotes transverse spatial frequency variables and η represents the axial frequency variable. Eq. (4.3) can be further expanded into the following three terms:

$$\begin{aligned}\tilde{\boldsymbol{I}}_{\text{img}}(\boldsymbol{u}, \eta) = \tilde{\boldsymbol{I}}_o + \tilde{\boldsymbol{I}}_{ss} + \iint \boldsymbol{S}(\boldsymbol{u}')\Big[\boldsymbol{P}(-\boldsymbol{u}')\tilde{\boldsymbol{V}}^*(-\boldsymbol{u}, -\eta)\tilde{\boldsymbol{G}}^*(-\boldsymbol{u}'-\boldsymbol{u}, -\eta-\eta')\boldsymbol{P}^*(-\boldsymbol{u}'-\boldsymbol{u}) \\ + \boldsymbol{P}^*(-\boldsymbol{u}')\tilde{\boldsymbol{V}}(\boldsymbol{u}, \eta)\tilde{\boldsymbol{G}}(-\boldsymbol{u}'+\boldsymbol{u}, -\eta'+\eta)\boldsymbol{P}(-\boldsymbol{u}'+\boldsymbol{u})\Big]\mathrm{d}^2\boldsymbol{u}',\end{aligned} \tag{4.4}$$

where $\tilde{\boldsymbol{I}}_o = \iint \boldsymbol{S}(\boldsymbol{u}')\,|\boldsymbol{P}(-\boldsymbol{u}')|^2 \mathrm{d}^2\boldsymbol{u}'\boldsymbol{\delta}(\boldsymbol{u}, \eta)$ is the DC term representing the background intensity. $\tilde{\boldsymbol{I}}_{ss}$ is a nonlinear term describing 2nd order scattering interactions, involving convolution between $\tilde{\boldsymbol{V}}$ and $\tilde{\boldsymbol{V}}^*$. If the sample has small RI contrast and weak absorption, this 2nd order term becomes negligible. Hence, under the weak object approximation (WOA), Eq. (4.4) is linearized by dropping $\tilde{\boldsymbol{I}}_{ss}$. The implication is that the linear relation only holds

when a majority of the scattered energy is contributed from the interaction between the scattered field and the illumination [32, 33, 90], as opposed to the interaction of the scattered field with itself. This tends to be a valid approximation for transparent biological cells, which provide a strong DC term and minimal scatter-scatter interactions.

To evaluate the phase and absorption effects separately, it is necessary to consider both real and imaginary parts of the scattering potential, $\tilde{\boldsymbol{V}} = \tilde{\boldsymbol{V}}_{\mathrm{Re}} + \mathrm{i}\tilde{\boldsymbol{V}}_{\mathrm{Im}}$. Finally, the forward model, relating the 3D intensity images under different illumination patterns to the 3D scattering potential, becomes

$$\tilde{\boldsymbol{I}}_{\mathrm{img}} = \tilde{\boldsymbol{I}}_o + \boldsymbol{H}_{\mathrm{Re}}\tilde{\boldsymbol{V}}_{\mathrm{Re}} + \boldsymbol{H}_{\mathrm{Im}}\tilde{\boldsymbol{V}}_{\mathrm{Im}}, \tag{4.5}$$

where the 3D *phase* transfer function $\boldsymbol{H}_{\mathrm{Re}}$ is

$$\begin{aligned}\boldsymbol{H}_{\mathrm{Re}}(\boldsymbol{u},\eta) = \iint \boldsymbol{S}(\boldsymbol{u}')\Big[&\boldsymbol{P}^*(-\boldsymbol{u}')\tilde{\boldsymbol{G}}(-\boldsymbol{u}'+\boldsymbol{u},-\eta'+\eta)\boldsymbol{P}(-\boldsymbol{u}'+\boldsymbol{u})+\\ &\boldsymbol{P}(-\boldsymbol{u}')\tilde{\boldsymbol{G}}^*(-\boldsymbol{u}'-\boldsymbol{u},-\eta'-\eta)\boldsymbol{P}^*(-\boldsymbol{u}'-\boldsymbol{u})\Big]\mathrm{d}^2\boldsymbol{u}'\end{aligned} \tag{4.6}$$

and the 3D *absorption* transfer function $\boldsymbol{H}_{\mathrm{Im}}$ is

$$\begin{aligned}\boldsymbol{H}_{\mathrm{Im}}(\boldsymbol{u},\eta) = \mathrm{i}\iint \boldsymbol{S}(\boldsymbol{u}')\Big[&\boldsymbol{P}^*(-\boldsymbol{u}')\tilde{\boldsymbol{G}}(-\boldsymbol{u}'+\boldsymbol{u},-\eta'+\eta)\boldsymbol{P}(-\boldsymbol{u}'+\boldsymbol{u})-\\ &\boldsymbol{P}(-\boldsymbol{u}')\tilde{\boldsymbol{G}}^*(-\boldsymbol{u}'-\boldsymbol{u},-\eta'-\eta)\boldsymbol{P}^*(-\boldsymbol{u}'-\boldsymbol{u})\Big]\mathrm{d}^2\boldsymbol{u}'.\end{aligned} \tag{4.7}$$

Since phase and absorption transfer functions only depend on the source $\boldsymbol{S}$ and pupil $\boldsymbol{P}$, which are known, they can be pre-computed. The 1st Born approximation is applied; however, the Rytov approximation could instead be used to arrive at the same result [93]. They are equivalent here because a small phase assumption (i.e. $|\boldsymbol{\phi}| \ll 1$) is made in both cases to build a linear relationship between the scattering potential of the sample and the measured intensity. Note that the Weak Object Transfer Functions (WOTFs) in Eq. (4.6) and (4.7) have been shown to be valid beyond the small-phase regime, for weakly scattering large-phase samples that have slowly varying phase/RI (i.e. $|\nabla\boldsymbol{\phi}| \ll 1$) [93, 94, 95]. Here, non-paraxial WOTFs are considered to also go beyond the paraxial regime [90, 93].

3D renderings and orthogonal slices of the phase and absorption transfer functions in Eq. (4.6) and (4.7) are shown in Fig. 4.2(a). For brightfield images, only the absorption transfer function contains non-zero values (*i.e.* no phase information is encoded). This is the familiar 3D incoherent transfer function in a wide-field microscope [90]. For DPC illumination, however, contrast comes mostly from phase [29] since the asymmetric illumination converts information about the real part of the scattering potential into measured intensity.

The spatial resolution of 3D DPC method is determined by wavelength λ and NA. The transverse Fourier coverage of the DPC transfer function spans a bandwidth $2\times$ larger than the NA of the objective ($\mathrm{NA}_{\perp,\mathrm{max}} = 2 \times \mathrm{NA}$), so phase and absorption may be recovered with resolution that is $2\times$ the coherent resolution limit. Axial bandwidth is also determined

by NA, but is not directly proportional. It improves non-linearly as the illumination and objective NAs increase ($\mathrm{NA}_{\parallel,\max} = 1 - \sqrt{1 - \mathrm{NA}^2}$) [11, 39, 90], as shown in Fig. 4.2(b). For instance, if an objective lens with 0.65 NA and a light source with $\lambda = 0.500\mu m$ are used, the Abbe diffraction-limited lateral and axial resolution are $\lambda/(2 \times \mathrm{NA}) = 0.385\mu m$ and $\lambda/(1 - \sqrt{1 - \mathrm{NA}^2}) = 2.083\mu m$, respectively.

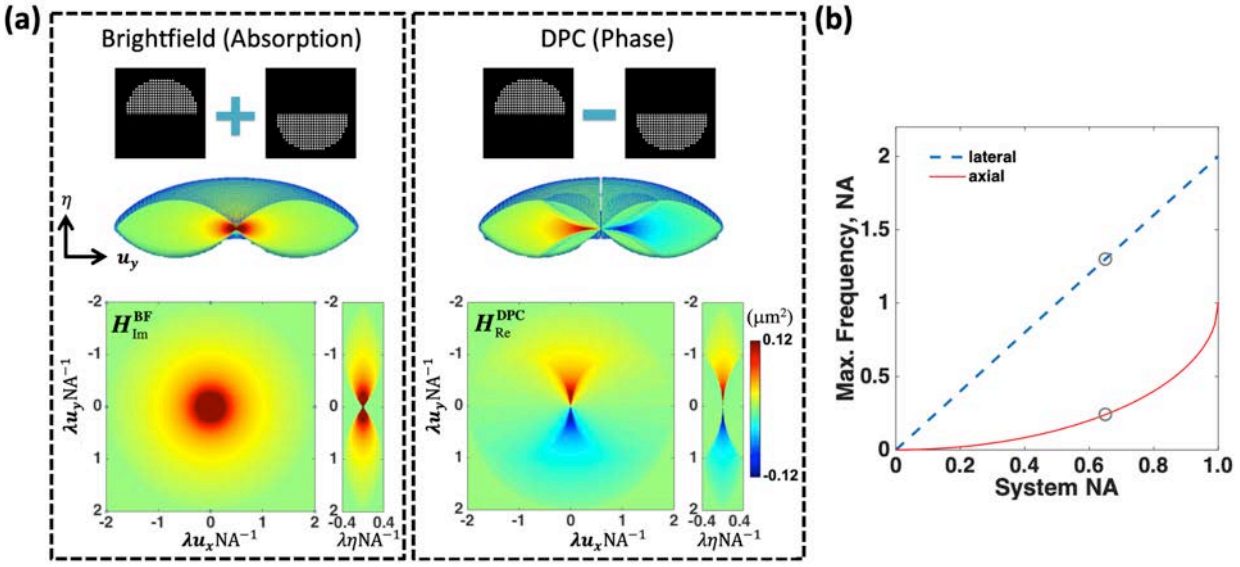

Figure 4.2: (a) Absorption ($\boldsymbol{H}_{\mathrm{Im}}$) and phase ($\boldsymbol{H}_{\mathrm{Re}}$) 3D transfer functions for the brightfield and DPC stacks. The NA of both illumination and detection is 0.65. (b) Lateral and axial resolution (measured by Fourier bandwidth normalized to units of NA) improve as the NA increases. Gray circles indicate the case shown in (a).

Inverse problem

Inverse problem with the imaging model in Sec. 4.2 estimates the sample's 3D complex RI from the captured intensity measurements. In the following, two reconstruction algorithms are compared: least squares (ℓ_2) and TV regularized. The least squares algorithm minimizes the ℓ_2-norm of the difference between the actual measurements and the predicted measurements based on the current estimate and the forward model. In this problem, since both the illumination and imaging optics only cover a limited range of angles, there is a 'missing cone' along the axial dimension in both the phase and absorption transfer functions (see Fig. 4.2). Direct inversion will therefore result in high-frequency artifacts due to the missing information. ℓ_2 (Tikhonov) regularization is a standard way to alleviate this problem [32]

by imposing a minimum total energy constraint as described in Sec. 1.3,

$$\min_{\tilde{\boldsymbol{V}}_{\mathrm{Re}},\tilde{\boldsymbol{V}}_{\mathrm{Im}}} \sum_m \left\| \tilde{\boldsymbol{I}}'_m - \boldsymbol{H}'_{\mathrm{Re},m}\tilde{\boldsymbol{V}}_{\mathrm{Re}} - \boldsymbol{H}'_{\mathrm{Im},m}\tilde{\boldsymbol{V}}_{\mathrm{Im}} \right\|_2^2 + \gamma_{\mathrm{Re}} \left\| \tilde{\boldsymbol{V}}_{\mathrm{Re}} \right\|^2 + \gamma_{\mathrm{Im}} \left\| \tilde{\boldsymbol{V}}_{\mathrm{Im}} \right\|_2^2, \tag{4.8}$$

where m indexes the illumination patterns corresponding to brightfield and DPC, γ_{Re} and γ_{Im} are regularization parameters, $\tilde{\boldsymbol{I}}'$ denotes the Fourier transform of the normalized intensity data stack and $\boldsymbol{H}'_{\mathrm{Re}} = \boldsymbol{H}_{\mathrm{Re}}/|\tilde{\boldsymbol{I}}_o|$ and $\boldsymbol{H}'_{\mathrm{Im}} = \boldsymbol{H}_{\mathrm{Im}}/|\tilde{\boldsymbol{I}}_o|$ are normalized transfer functions. The brightfield image stack is computed by averaging the intensities from all DPC illumination patterns (top, bottom, left, right). Each brightfield image is normalized by first subtracting a background image, and then dividing it by the (scalar) DC term. The DPC images are computed by taking the difference of the pairs of images from complimentary illumination patterns, then normalized by the illumination intensity. Mathematically, these procedures are written as:

$$\boldsymbol{I}_{\mathrm{BF}} = \frac{\boldsymbol{I}_{\mathrm{top}} + \boldsymbol{I}_{\mathrm{bottom}} + \boldsymbol{I}_{\mathrm{right}} + \boldsymbol{I}_{\mathrm{left}}}{2},\ \boldsymbol{I}'_{\mathrm{BF}} = \frac{\boldsymbol{I}_{\mathrm{BF}} - |\tilde{\boldsymbol{I}}_o|}{|\tilde{\boldsymbol{I}}_o|},\ \boldsymbol{I}'_{\mathrm{DPC}} = \frac{\boldsymbol{I}_{\mathrm{top/right}} - \boldsymbol{I}_{\mathrm{bottom/left}}}{|\tilde{\boldsymbol{I}}_o|}. \tag{4.9}$$

where $\boldsymbol{I}_{\mathrm{top}}$, $\boldsymbol{I}_{\mathrm{bottom}}$, $\boldsymbol{I}_{\mathrm{right}}$ and $\boldsymbol{I}_{\mathrm{left}}$ represent measured intensities using top, bottom, right, and left half-circle illumination, respectively, $\boldsymbol{I}_{\mathrm{BF}}$ is brightfield intensity and $\boldsymbol{I}'_{\mathrm{DPC}}$ is the normalized DPC intensity. One can acquire the DC term by measuring the background brightfield intensity without the sample. However, it can be approximated by the average intensity of the brightfield images when the WOA holds, *i.e.* $|\tilde{\boldsymbol{I}}_o| = \langle \boldsymbol{I}_{\mathrm{BF}} \rangle$.

Equation (4.8) has a closed-form solution that can be obtained by setting its derivative with respective to $\boldsymbol{V}_{\mathrm{Re}}$ and $\boldsymbol{V}_{\mathrm{Im}}$ to zero, giving the least-squares solution:

$$\begin{aligned}
\tilde{\boldsymbol{V}}_{\mathrm{Re}} &= \frac{\left(\sum_m |\boldsymbol{H}'_{\mathrm{Im},m}|^2 + \gamma_{\mathrm{Im}}\right)\sum_m \left(\boldsymbol{H}'^{*}_{\mathrm{Re},m}\tilde{\boldsymbol{I}}'_m\right) - \sum_m \left(\boldsymbol{H}'^{*}_{\mathrm{Re},m}\boldsymbol{H}'_{\mathrm{Im},m}\right)\sum_m \left(\boldsymbol{H}'^{*}_{\mathrm{Im},m}\tilde{\boldsymbol{I}}'\right)}{\left(\sum_m |\boldsymbol{H}'_{\mathrm{Re},m}|^2 + \gamma_{\mathrm{Re}}\right)\left(\sum_m |\boldsymbol{H}'_{\mathrm{Im},m}|^2 + \gamma_{\mathrm{Im}}\right) - \sum_m \left(\boldsymbol{H}'_{\mathrm{Re},m}\boldsymbol{H}'^{*}_{\mathrm{Im},m}\right)\sum_m \left(\boldsymbol{H}'^{*}_{\mathrm{Re},m}\boldsymbol{H}'_{\mathrm{Im},m}\right)} \\
\tilde{\boldsymbol{V}}_{\mathrm{Im}} &= \frac{\left(\sum_m |\boldsymbol{H}'_{\mathrm{Re},m}|^2 + \gamma_{\mathrm{Re}}\right)\sum_m \left(\boldsymbol{H}'^{*}_{\mathrm{Im},m}\tilde{\boldsymbol{I}}'_m\right) - \sum_m \left(\boldsymbol{H}'_{\mathrm{Re},m}\boldsymbol{H}'^{*}_{\mathrm{Im},m}\right)\sum_m \left(\boldsymbol{H}'^{*}_{\mathrm{Re},m}\tilde{\boldsymbol{I}}'\right)}{\left(\sum_m |\boldsymbol{H}'_{\mathrm{Re},m}|^2 + \gamma_{\mathrm{Re}}\right)\left(\sum_m |\boldsymbol{H}'_{\mathrm{Im},m}|^2 + \gamma_{\mathrm{Im}}\right) - \sum_m \left(\boldsymbol{H}'_{\mathrm{Re},m}\boldsymbol{H}'^{*}_{\mathrm{Im},m}\right)\sum_m \left(\boldsymbol{H}'^{*}_{\mathrm{Re},m}\boldsymbol{H}'_{\mathrm{Im},m}\right)}.
\end{aligned} \tag{4.10}$$

Hence, the scattering potential can be recovered using deconvolution with FFTs. The two regularization parameters, γ_{Re} and γ_{Im}, should scale with the magnitude of $\boldsymbol{V}_{\mathrm{Re}}$ and $\boldsymbol{V}_{\mathrm{Im}}$, respectively. Overly large regularization parameters result in reduction of absorption and phase values, while overly small regularization parameters result in high frequency noise.

Due to the missing cone problem, phase reconstructions suffer from halo artifacts (see Fig. 4.3(c)). To mitigate this, two different priors are exploited. First, a piece-wise constant approximation of the 3D scattering potential (*i.e.* the sample can be represented as multiple regions of constant RI) is made by using a TV regularizer [38, 96]. Second, in the experiments, the sample is immersed in a medium whose RI is always smaller than the sample's. Thus,

positivity constraint can be further imposed on the RI. Including both priors, the 3D phase reconstruction solves the following minimization problem similar to Eq. (1.29):

$$\min_{\tilde{\boldsymbol{V}}_{\mathrm{Re}},\tilde{\boldsymbol{V}}_{\mathrm{Im}}} \sum_m \left\| \tilde{\boldsymbol{I}}'_m - \boldsymbol{H}'_{\mathrm{Re},m}\tilde{\boldsymbol{V}}_{\mathrm{Re}} - \boldsymbol{H}'_{\mathrm{Im},m}\tilde{\boldsymbol{V}}_{\mathrm{Im}} \right\|_2^2 + \tau_{\mathrm{Re}} \left\| \boldsymbol{V}_{\mathrm{Re}} \right\|_{\mathrm{TV}} + \tau_{\mathrm{Im}} \left\| \boldsymbol{V}_{\mathrm{Im}} \right\|_{\mathrm{TV}}, \quad \text{s.t. } \boldsymbol{V}_{\mathrm{Re}}, \boldsymbol{V}_{\mathrm{Im}} \leq 0, \quad (4.11)$$

where τ_{Re} and τ_{Im} are the regularization coefficients. We adopt the anisotropic 3D TV operator, $\|\cdot\|_{\mathrm{TV}} = \|\nabla\{\cdot\}\|_1$, in which ∇ is the 3D gradient operator. Finally, ADMM algorithm introduced in Sec. 1.3 is then applied to recover the 3D scattering potential.

4.3 Experimental Results

The experimental setup is a commercial microscope (Nikon TE300) with source patterning achieved by a programmable LED array (32×32, 4 mm spacing, central $\lambda = 0.514\mu m$). The LED array is placed at 69 mm above the focal plane in order to provide illumination NA 0.65. An automated piezo-stage (Thorlabs, MZS500-E) implements axial scanning while capturing 4 images at each position using the 4 half-circle illumination patterns shown in Fig. 4.1. In order to avoid aliasing, the axial spacing between focus planes within the 3D intensity stack should be smaller than the DoF, $\lambda/(2-2\sqrt{1-\mathrm{NA}^2})$. At the same time, it is required to capture the full axial range of the sample's intensity variations. Hence, for 10–20 μm thick samples, data at 100 defocus planes equally spaced by 1 μm are collected. Note that the method requires similar amounts of data as compared to other diffraction tomography schemes, which use 4 phase-shifted interferograms (or an off-axis hologram with 4× more pixels) at each angle [97] or axial plane [52]. Both the LED array and the piezo-stage are synchronized to the camera (PCO.Edge 5.5), so acquisition speed is limited by the axial translation speed ($\sim$ 90 seconds for 400 images).

During the reconstruction process, the 4 images at each z are first used to synthesize a brightfield and two DPC images along orthogonal directions [32]. These brightfield and DPC image stacks provide complementary information. Direct solutions from inverse algorithms are complex scattering potentials, which are converted to RI distributions. Using FFT-based implementations, reconstruction of 512×512×100 voxels using Eq. (4.8) on a desktop computer (Intel i7 CPU) with Matlab takes ∼10 seconds, whereas implementation of Eq. (4.11) typically requires about 30 iterations to converge (∼13 minutes). Computation times could be further reduced through parallel processing on Graphics Processing Units (GPUs).

Comparison between ℓ_2 and TV regularization

To compare reconstruction algorithms for a known test sample, a single polystyrene bead (Sigma-Aldrich) immersed in index-matching fluid (Cargille, index 1.59) is imaged. This sample is a pure phase object with piece-wise constant RI, so satisfies the TV constraint.

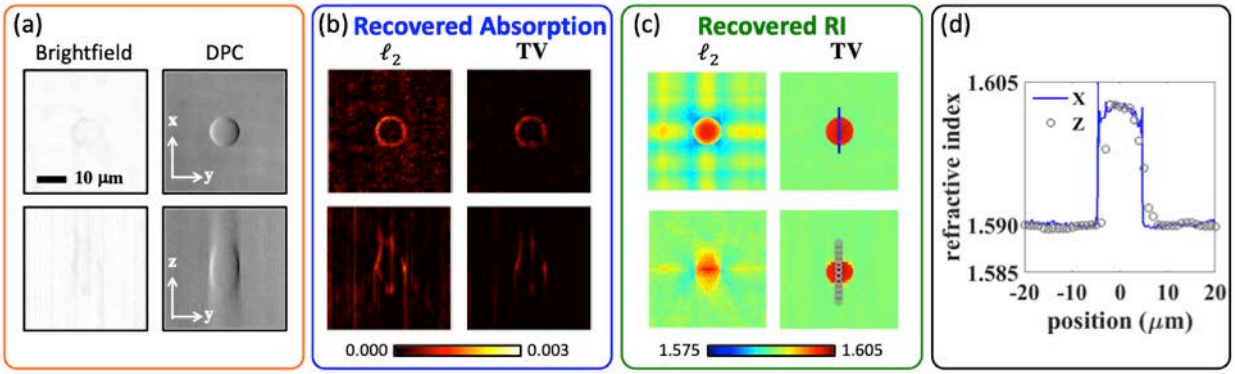

Figure 4.3: 3D RI reconstructions of a 10μm diameter polystyrene bead immersed in oil of RI 1.59 (40× 0.65 NA objective lens). (a) Cross-sectional views of 3D brightfield and DPC measurements. (b) Absorption and (c) phase reconstructions with ℓ_2 and TV regularization. (d) 1D cross-sections of recovered RI with TV regularization.

Two cross-sectional views of the 3D brightfield and DPC intensity stacks from Eq. (4.9) are shown in Fig. 4.3(a). Brightfield images appear to have absorption at the edges of the bead, where strong diffraction causes light to scatter outside the the objective's collection aperture. Since this loss is small, the recovered absorption map using ℓ_2 (Tikhonov) regularization is noisy (Fig. 4.3(b)).

Looking at the reconstructed 3D RI (Fig. 4.3(c,d)), significantly less halo artifacts are observed in the TV regularization case, as compared to ℓ_2, as well as less noise. The reconstruction with ℓ_2 regularization suffers from elongation along the axial direction - the axial width is ∼1.6× larger than the bead. This is due to the missing frequencies along the axial direction (see Fig. 4.2(a)). In order to reduce the elongation, one can use higher NA, rotate the object [93], or leverage prior knowledge similar to this case. Alternatively, nonlinear forward models [43, 96] that accounts for multiple-scattering can be used to go beyond the 1st Born approximation and the WOA, potentially allowing recovery of higher frequency components as well as missing cone information. However, such algorithms are not guaranteed to find the global solution and require more computation power and time. Despite using a weak object approximation, the reconstructed RI (∼ 1.602) matches well with previous experimental measurements [98], providing accurate quantitative phase results. In the rest of experimental results, the TV regularization are adopted.

Effect of numerical aperture

To experimentally study the effects of NA on final 3D phase reconstructions, results from two objective lenses (20× 0.40NA and 40× 0.65NA) are compared. The test sample is composed of several polystyrene beads immersed in oil of RI 1.54. As expected, higher NA gives better resolution in both lateral and axial dimensions, as shown in Fig. 4.4. Poor depth sectioning

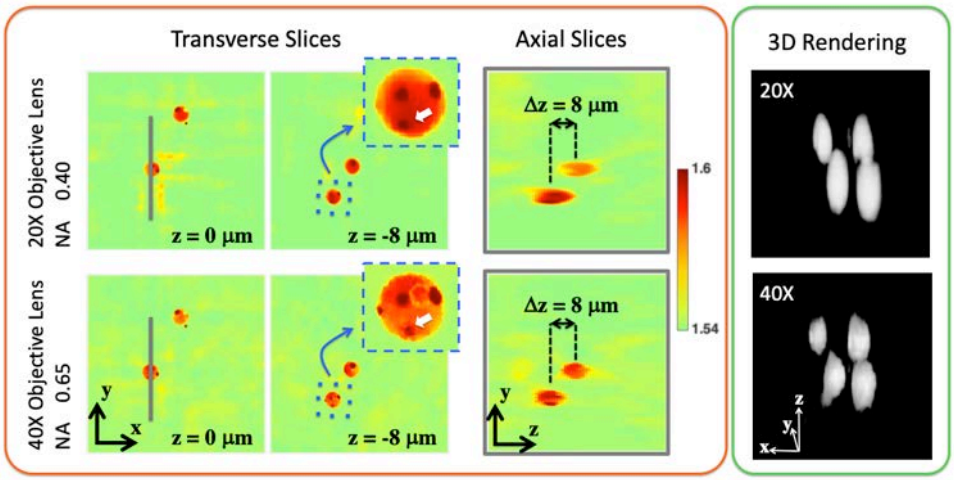

Figure 4.4: Comparison of recovered 3D RI (6 μm polystyrene beads) with 20× 0.4 NA and 40× 0.65 NA objectives. Larger NA provides better lateral and axial resolution.

from the lower NA also causes slowly varying background artifacts, which are mitigated in the high NA reconstructions. The improved axial resolution both reduces the axial elongation and enables observation of finer structures within the large beads (indicated by the white arrows). The diffraction-limited lateral and axial resolutions are 0.64 μm and 6.14 μm for 20× objective, and 0.39 μm and 2.14 μm for 40× objective, respectively. Figure 4.4 also illustrates a caveat of 3D DPC. As the index difference between the surrounding media and the beads becomes larger ($\Delta n > 0.07$ in this case), the WOA or slowly-varying phase approximation does not hold but the model attempts to fit the measurements with those assumptions. Hence, although the shape remains the same, the retrieved RI is lower than the actual value.

Comparison between 2D and 3D phase reconstructions

To illustrate the differences between 2D and 3D phase imaging, two different 2D phase methods (2D DPC [32] and the transport of intensity equation (TIE) [18]) are also implemented. Both use through-focus intensity stacks to recover the on-axis projected phase, ignoring sample thickness. A 40× 0.65 NA objective is used and fixed saline-immersed human mammary epithelial MCF10A cell is imaged. To implement TIE, 15 images are recorded with exponential axial spacing from 1 μm to 64 μm, using coherent (single-LED) illumination. The phase at the focal plane is recovered using a modified TIE algorithm [18]. Note that 2D DPC provides 2× better lateral resolution than TIE (see Fig. 4.5(a)) because it uses partially coherent illumination.

Since the 2D phase reconstructions are proportional to the total projected optical path length of the sample, this quantity alone cannot distinguish features at different axial posi-

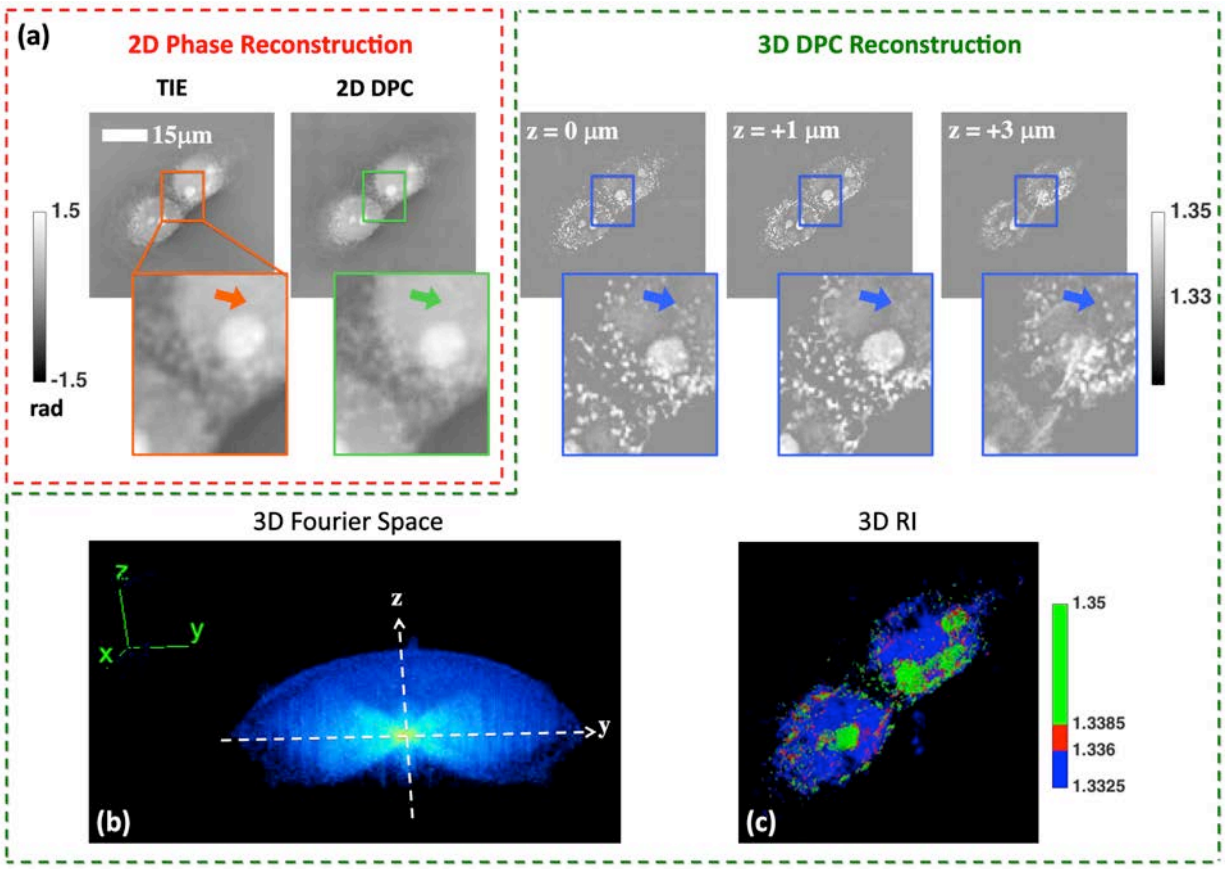

Figure 4.5: Comparison between 2D phase reconstructions (TIE and 2D DPC) and 2D slices of 3D DPC RI reconstruction for a human mammary epithelial MCF10A cell. (a) TIE and 2D DPC, next to three slices of the recovered RI from 3D DPC at three different depths. (b) 3D view of the recovered index's 3D Fourier spectrum. (c) 3D rendering of the recovered RI distribution.

tions. The 3D DPC method, on the other hand, can clearly distinguish sub-cellular features such as cytosol, cytoplasm and nucleus, which are located at different axial planes (see Fig. 4.5). The sharper appearance of the reconstructed slices is a result of the axial sectioning that removes out-of-focus features. 3D DPC provides the same lateral resolution as 2D DPC and the reconstructed 3D Fourier spectrum (Fig. 4.5(b)) covers the same volume in Fourier space as the transfer functions in Fig. 4.2(a). In Fig. 4.5(c), it shows the 3D rendered RI reconstruction with different RI values mapping to different colors as in [36, 52].

3D DPC is also applied to image embryo cells (Fig. 4.6). These cells have diameter ∼100 μm and are surrounded by *zona pellucida* (bottom arrow). The top arrow points to the *polar body* of the oocyte. The nucleus as well as cytoplasm distribution along the axial direction are clearly observed within the region in the orange box. The blue dashed box shows a 4-cell stage embryo at three distinct focus planes, where two sets of two cells sit on top of each

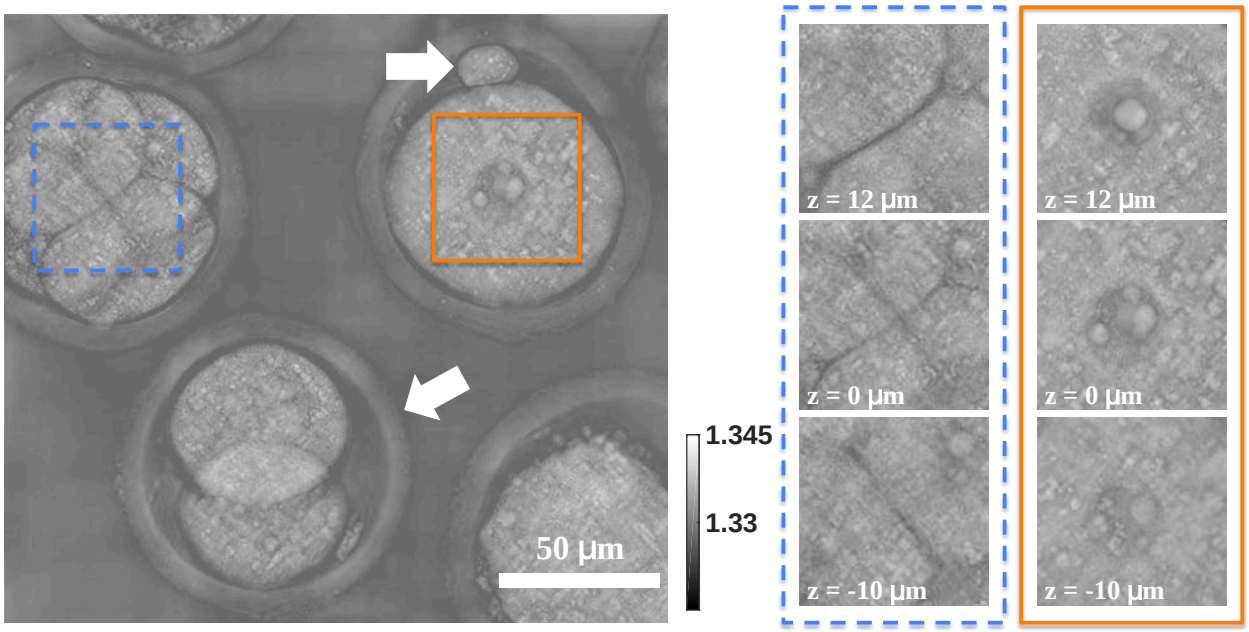

Figure 4.6: Reconstructed 3D RI of embryo cells. (Left) Full field-of-view at a single focus plane. (Right) 3 axial slices for regions in the blue dashed and orange boxes.

other, with cleavage planes on the diagonal and off-diagonal directions. Recovering the 3D information enables us to figure out the location of individual cells, providing a non-invasive way to isolate sub-cellular features with high resolution and accuracy.

4.4 Summary

A novel quantitative 3D phase imaging technique is introduced, which captures images with asymmetric partially coherent illumination at different focus planes. Under the 1st Born approximation, a linear 3D model can be derived that relates illumination-dependent intensity to 3D RI and absorption. The reconstruction algorithm is fast and efficient, using either Tikhonov (ℓ_2) or TV regularization with a positivity constraint. The experimental setup is simple and inexpensive (with an LED array add-on), enabling label-free and stain-free single-cell imaging with sub-cellular feature specificity.

Chapter 5

3D Phase Imaging with Multiple-Scattering Objects

5.1 multiple-scattering Models for 3D Phase Imaging

While many 3D phase imaging methods like 3D DPC in Chapter 4 work with weakly scattering objects, they fail imaging the multiple-scattering objects due to their inaccurate forward models. To perform 3D phase imaging with multiple-scattering objects or optically dense samples, a scattering model that describes light-matter interaction beyond the single scattering regime is needed. As a result, Multi-Slice (MS) or beam propagation method scattering model was adopted to account for multiple-scattering effects when light propagates through the objects, and inverse problems were solved using MS propagation with both holography and intensity only measurements [43, 96]. MS assumes each slice as an infinitesimally thin transmission layer. However, it is no longer accurate in the case of oblique illuminations; the off-axis light travels a longer distance compared to the on-axis light. Therefore, the accuracy of MS lessens as the angle of incidence increases. Several heuristic approaches have been proposed to mitigate the issue, but they rely on geometric optics within each slice and are either not stable for high angle oblique illuminations or greatly increase computation cost [99, 100]. In addition, MS only describes the forward scattering process and misses the back-scattered light, which can potentially be used to solve the missing cone problems in ODT. More quantitatively accurate scattering models have also been developed to generate forward and backward scattering fields close to the analytic solution of the Helmholz equation via series of convolutions with a 3D Green's function. These include recursive Born [11, 101], contrast source inversion method [102], coupled dipole method [103], hybrid method [104], and series expansion with accelerated gradient descent on the Lippmann-Schwinger Equation (SEAGLE) [105]. Unlike the weakly scattering models or MS, they require orders of magnitude more computation and memory due to 3D matrix operations, which limits their application to 2D slice reconstructions or small volume 3D phase tomography [106, 107]. To conquer the issues mentioned above, a new efficient scattering model, Multi-Layer Born

(MLB), is presented in this chapter. The model contains two major conceptual steps. First, the 3D object is decomposed into multiple 3D slabs with finite thickness. Second, 1st Born scattering process is sequentially applied to each slab. This new method not only removes the paraxial assumption in MS, but is also capable of computing backward scattering light from the samples.

5.2 Multi-Layer Born Light Scattering Model for 3D Phase Tomography

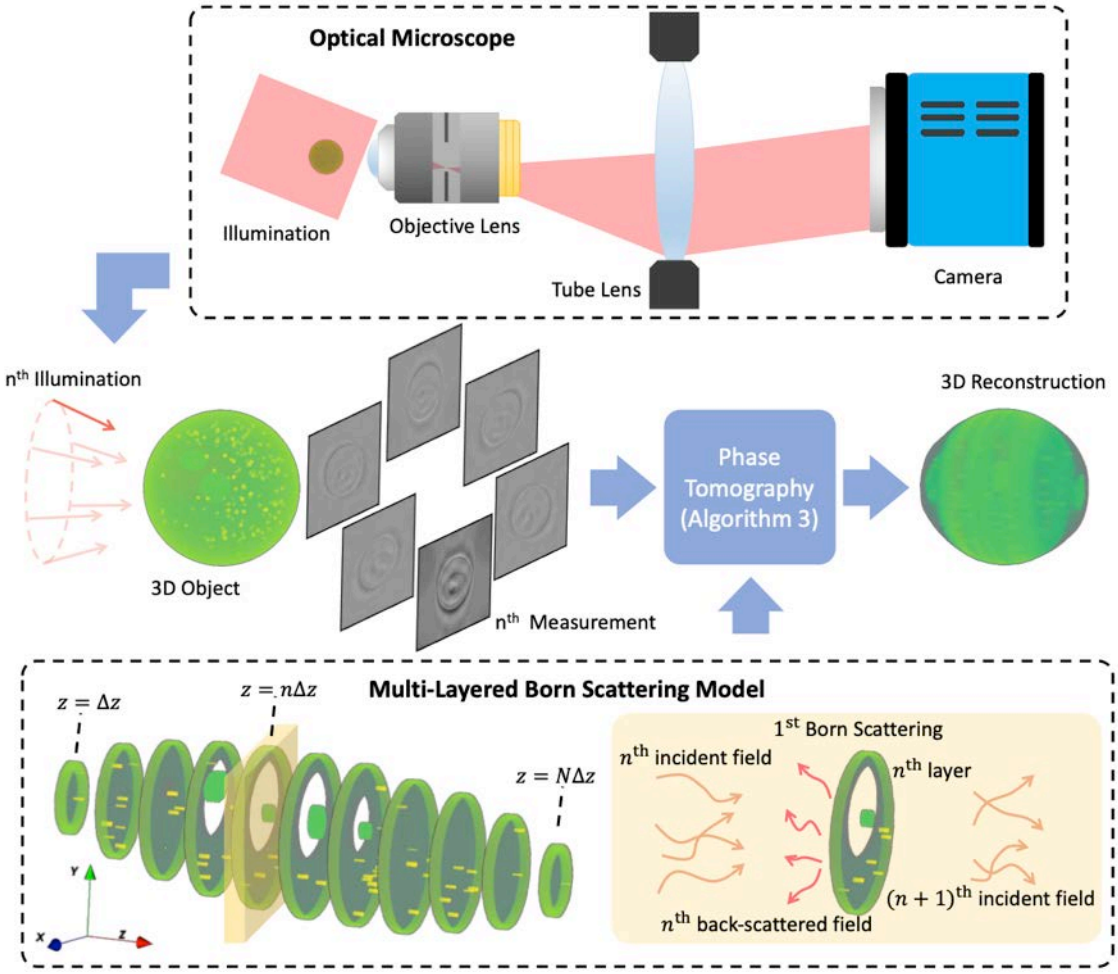

Figure 5.1: Proposed 3D phase imaging framework. Intensity measurements with spatially coherent illuminations from different angles are captured on an optical microscope and fed in as inputs to the 3D phase tomography algorithm. By solving a nonlinear optimization problem with MLB scattering model, 3D RI of a multiple-scattering object can be recovered.

Forward scattering model

Any 3D scattering object can be described by a spatial distribution of scattering potential, $\boldsymbol{V}(x, y, z)$, which is related to its RI, $\boldsymbol{n}(x, y, z)$, in the following expression:

$$\boldsymbol{V}(x, y, z) = k_o^2 \left(n_{\mathrm{b}}^2 - \boldsymbol{n}^2(x, y, z)\right), \tag{5.1}$$

where (x, y, z) represents the 3D coordinates, $k_o = \frac{2\pi}{\lambda}$, λ is the wavelength of incident field, and n_{b} denotes background RI of the surrounding media. As light propagates through the object, the scattered field interferes with the incident field and forms the total field. Under the 1st Born approximation, the scattered field is linearly related to the scattering potential by a Green's function, $\boldsymbol{G}(x, y, z)$ [11]. Consequently, given the incident field, $\boldsymbol{U}_{\mathrm{in}}$, the total field, $\boldsymbol{U}_{\mathrm{tot}}$ follows the expression in Eq. (1.6):

$$\boldsymbol{U}_{\mathrm{tot}}(x, y, z) = \boldsymbol{U}_{\mathrm{in}}(x, y, z) + \iiint \boldsymbol{G}(x - x', y - y', z - z')\boldsymbol{U}_{\mathrm{in}}(x', y', z')\boldsymbol{V}(x', y', z')\mathrm{d}x'\mathrm{d}y'\mathrm{d}z' \,. \tag{5.2}$$

This linear assumption only holds when the magnitude of $\boldsymbol{V}$ is small (*i.e.* a weakly scattering object). Note that Eq. (5.2) does not account for multiply scattering processes in highly scattering objects. However, multiple-scattering is accounted for when the object is divided into multiple weakly scattering pieces and each being sequentially applied the 1st Born scattering process. Intuitively, a 3D object can be viewed as layer-by-layer slabs, and each layer has a thin finite thickness Δz. Under this configuration, the field after wave propagates through the n^{th} layer is the total field after the n^{th} layer by Eq. (5.2), and serves as the the incident field of the $(n+1)^{\mathrm{th}}$ layer. Therefore, by applying the 1st Born scattering process on each layer recursively, the total field evaluated from the last layer becomes the final multiply scattered field that will reach the imaging plane. Going forward, we will refer to this method as the Multi-Layer Born (MLB) scattering model. Let $\boldsymbol{U}^n$ and $\boldsymbol{U}_{\mathrm{s}}^n$ be the incident field and the scattered field of the n^{th} layer, the recursive formula can be written as

$$\boldsymbol{U}^{n+1}(\boldsymbol{\rho}, (n+1)\Delta z) = \boldsymbol{U}^n(\boldsymbol{\rho}, (n+1)\Delta z) + \boldsymbol{U}_{\mathrm{s}}^n(\boldsymbol{\rho}, (n+1)\Delta z) \text{ , where} \tag{5.3}$$

$$\boldsymbol{U}_{\mathrm{s}}^n(\boldsymbol{\rho}, (n+1)\Delta z) = \int_{\frac{-\Delta z}{2}}^{\frac{\Delta z}{2}} \iint \boldsymbol{G}(\boldsymbol{\rho} - \boldsymbol{\rho}', \Delta z - \zeta)\boldsymbol{U}^n(\boldsymbol{\rho}', n\Delta z + \zeta)\boldsymbol{V}(\boldsymbol{\rho}', n\Delta z + \zeta)\mathrm{d}^2\boldsymbol{\rho}'\mathrm{d}\zeta \,, \tag{5.4}$$

where $\boldsymbol{\rho} = (x, y)$ is the 2D vector in real space coordinates.

The first term in Eq. (5.3) is the incident field at the center of n^{th} layer propagating to a distance Δz away. Given the 2D Fourier transform operator $\mathcal{F}\{\cdot\}$, the spatial frequency spectrum of the incident field $\tilde{\boldsymbol{U}}^n(\boldsymbol{u}) = \mathcal{F}\{\boldsymbol{U}^n(\boldsymbol{\rho}, n\Delta z)\}$, and the angular spectrum propagation kernel $\boldsymbol{K}(\boldsymbol{u}, z) = e^{\mathrm{i}2\pi z\sqrt{(n_{\mathrm{b}}/\lambda)^2 - \|\boldsymbol{u}\|_2^2}}$ with the 2D spatial frequency space coordinates vector $\boldsymbol{u}$, we get

$$\boldsymbol{U}^n(\boldsymbol{\rho}, (n+1)\Delta z) = \mathcal{F}^{-1}\left\{\boldsymbol{K}(\boldsymbol{u}, \Delta z)\tilde{\boldsymbol{U}}^n(\boldsymbol{u})\right\} \,. \tag{5.5}$$

To simplify Eq. (5.4), it is useful to use the Fourier representation of the Green's function in Eq. (1.21). In addition, the scattering potential is assumed to not vary axially within each layer because the thickness, Δz, is small, *i.e.* $\boldsymbol{V}(\boldsymbol{\rho}, n\Delta z+\zeta) = \boldsymbol{V}^n(\boldsymbol{\rho})$ for $\zeta \in [-\Delta z/2, \Delta z/2]$. Based on Eqs. (5.4), (1.21) and the convolution theorem, the spatial frequency spectrum of the scattered field, $\tilde{\boldsymbol{U}}_s^n(\boldsymbol{u}) = \mathcal{F}\{\boldsymbol{U}_\mathrm{s}^n(\boldsymbol{\rho}, (n+1)\Delta z)\}$, becomes

$$\tilde{\boldsymbol{U}}_\mathrm{s}^n(\boldsymbol{u}) = \int_{\frac{-\Delta z}{2}}^{\frac{\Delta z}{2}} \iint \frac{-\mathrm{i}\boldsymbol{K}(\boldsymbol{u}, \Delta z - \zeta)}{4\pi\boldsymbol{\Gamma}(\boldsymbol{u})} \boldsymbol{K}(\boldsymbol{u}', \zeta)\tilde{\boldsymbol{U}}^n(\boldsymbol{u}')\tilde{\boldsymbol{V}}^n(\boldsymbol{u}-\boldsymbol{u}')\mathrm{d}^2\boldsymbol{u}'\mathrm{d}\zeta \ , \tag{5.6}$$

where $\tilde{\boldsymbol{V}}^n(\boldsymbol{u}) = \mathcal{F}\{\boldsymbol{V}^n(\boldsymbol{\rho})\}$ denotes the 2D spatial frequency spectrum of the scattering potential at the n^{th} layer. The integration along the ζ dimension only involves two propagation kernels,

$$\int_{\frac{-\Delta z}{2}}^{\frac{\Delta z}{2}} \boldsymbol{K}(\boldsymbol{u}, \Delta z - \zeta)\boldsymbol{K}(\boldsymbol{u}', \zeta)\mathrm{d}\zeta = \boldsymbol{K}(\boldsymbol{u}, \Delta z)\mathrm{sinc}\Big(\Big(\boldsymbol{\Gamma}(\boldsymbol{u}') - \boldsymbol{\Gamma}(\boldsymbol{u})\Big)\Delta z\Big)\Delta z \ , \tag{5.7}$$

where $\mathrm{sinc}(\boldsymbol{x}) = \sin(\pi\boldsymbol{x})/(\pi\boldsymbol{x})$. Plugging in the integration result into Eq. (5.6), we obtain

$$\tilde{\boldsymbol{U}}_\mathrm{s}^n(\boldsymbol{u}) = \tilde{\boldsymbol{G}}(\boldsymbol{u}, \Delta z) \iint \mathrm{sinc}\Big(\Big(\boldsymbol{\Gamma}(\boldsymbol{u}') - \boldsymbol{\Gamma}(\boldsymbol{u})\Big)\Delta z\Big)\tilde{\boldsymbol{U}}^n(\boldsymbol{u}')\tilde{\boldsymbol{V}}^n(\boldsymbol{u}-\boldsymbol{u}')\Delta z\mathrm{d}^2\boldsymbol{u}' \ . \tag{5.8}$$

Eqs. (5.5) and (5.8) conclude the forward scattering part of MLB. Eq. (5.8) is computation expensive; however, the sinc function is almost equal to 1 when a small Δz is chosen and the integration becomes a convolution, which can be efficiently evaluated via FFT. The major difference between MLB and MS scattering models is that MLB considers non-paraxial 3D scattering effect within each layer while MS simplifies it with a 2D field transmission. Hence, MLB becomes more accurate as oblique light dominates in the object. Due to the nature of 3D scattering, MLB is also capable of modelling the backward scattering field (detailed derivation and simulation of backward scattering in Appendix A.2). Usually, the total field after the light passes through all the layers is imaged by a low-pass imaging system, where the spatial frequency bandwidth is determined by the NA of the imaging system. This process is described by refocusing the total field to the image plane and applying a low-pass filter. Typically, the objective lens focuses at the center plane of the object, where the refocusing distance is $\Delta f = -N\Delta z/2$ from the last layer to the center. With the ideal circular low-pass filter $\boldsymbol{P}(\boldsymbol{u}) = \mathrm{Circ}(\boldsymbol{u}\lambda/\mathrm{NA})$, the measured forward scattered field can be efficiently computed using FFTs, as shown in Algorithm 1.

3D intensity-based phase tomography with MLB

An intuitive way to probe 3D structure of an object is by rotating the object around the axis perpendicular to the optical axis [108, 109]. However, this is difficult to achieve on an

Algorithm 1 Multi-Layer Born Forward Scattering

Input: Incident field at the 1st layer $\boldsymbol{U}^1(\boldsymbol{\rho}, \Delta z)$, N layers of 3D scattering potential $\{\boldsymbol{V}^n(\boldsymbol{\rho})\}_{n=1}^N$, layer thickness Δz, and the refocusing distance Δf.

1: **for** $n \leftarrow 1$ to N **do** ▷ MLB scattering

2: $\quad \boldsymbol{U}^n(\boldsymbol{\rho}, (n+1)\Delta z) \leftarrow \mathcal{F}^{-1}\left\{\boldsymbol{K}(\boldsymbol{u}, \Delta z)\mathcal{F}\left\{\boldsymbol{U}^n(\boldsymbol{\rho}, n\Delta z)\right\}\right\}$

3: $\quad \boldsymbol{U}_{\mathrm{s}}^n(\boldsymbol{\rho}, (n+1)\Delta z) \leftarrow \mathcal{F}^{-1}\left\{\tilde{\boldsymbol{G}}(\boldsymbol{u}, \Delta z)\mathcal{F}\left\{\boldsymbol{U}^n(\boldsymbol{\rho}, n\Delta z)\boldsymbol{V}^n(\boldsymbol{\rho})\Delta z\right\}\right\}$

4: $\quad \boldsymbol{U}^{n+1}(\boldsymbol{\rho}, (n+1)\Delta z) \leftarrow \boldsymbol{U}^n(\boldsymbol{\rho}, (n+1)\Delta z) + \boldsymbol{U}_{\mathrm{s}}^n(\boldsymbol{\rho}, (n+1)\Delta z)$

5: **end for**

6: $\boldsymbol{U}_{\mathrm{image}}(\boldsymbol{\rho}) \leftarrow \mathcal{F}^{-1}\left\{\boldsymbol{P}(\boldsymbol{u})\boldsymbol{K}(\boldsymbol{u}, \Delta f)\mathcal{F}\left\{\boldsymbol{U}^{N+1}(\boldsymbol{\rho}, (N+1)\Delta z)\right\}\right\}$ ▷ refocus and image

Return: Total field on the image plane $\boldsymbol{U}_{\mathrm{image}}$ and incident fields at each layer $\{\boldsymbol{U}^n(\boldsymbol{\rho}, n\Delta z)\}_{n=1}^N$.

optical microscope without additional hardware and limits the types of objects that can be imaged [93, 110]. In contrast, illuminating the object at various angles also reveals the 3D information of objects. This technique is widely adopted in ODT systems using either Galvo mirrors or spatial light modulators [35, 41, 111]. For intensity-based 3D phase tomography techniques, the requirement of spatial and temporal coherence of the light source is less stringent, and the illumination scanning process can be realized using an inexpensive LED array [50, 88, 112, 113]. Combining the illumination scanning scheme and the proposed MLB scattering model, a 3D intensity-based phase tomography algorithm that applies to multiple-scattering objects is complete. Similar to those previously proposed multiple-scattering methods [43, 96, 105], an iterative algorithm is needed to recover the 3D RI of the sample because the measurements are nonlinearly related to the scattering potential. First, the 3D intensity-based phase tomography is formulated as an optimization problem with an objective function $\mathcal{L}(V)$ as shown in Eq. (5.9):

$$\min_{\boldsymbol{V}} \mathcal{L}(\boldsymbol{V}) = \sum_{j=1}^{N_{\mathrm{LED}}} \| |\boldsymbol{U}_{\mathrm{image},j}(\boldsymbol{V})| - \sqrt{\boldsymbol{I}_{\mathrm{measure},j}} \|^2 + \tau \mathcal{R}(\boldsymbol{V}) \ , \tag{5.9}$$

where N_{LED} is the total number of LED used which determines the number of illuminations. Equation (5.9) consists of two terms. The first term is the data fidelity term that measures the Euclidean distance between the estimated amplitudes and the square root of measured intensities $\boldsymbol{I}_{\mathrm{measure}}$ from MLB prediction. The second term is a regularization term that enforces prior knowledge on the 3D scattering potential. To balance the strength of data fidelity and regularization, τ is introduced as a tunable parameter. Because the minimum of Eq. (5.9) cannot be computed analytically, an iterative algorithm is required. Due to the large scale nature of 3D tomography problems, the proximal gradient method is chosen for minimizing Eq. (5.9) which has relatively lower memory requirements and computation complexity compared to ADMM or 2nd order Newton's method. To implement the inverse algorithm, gradient of the data fidelity term with respect to $\boldsymbol{V}$, $\{\boldsymbol{V}_{\mathrm{grad}}^n(\boldsymbol{\rho})\}_{n=1}^N$, is required

Algorithm 2 Gradient Computation

Input: Measured intensity $\boldsymbol{I}_{\text{measure}}$, predicted total field on the image plane $\boldsymbol{U}_{\text{image}}$, incident fields at each layer $\{\boldsymbol{U}^n(\boldsymbol{\rho}, n\Delta z)\}_{n=1}^N$, current estimated 3D scattering potential $\{\boldsymbol{V}^n(\boldsymbol{\rho})\}_{n=1}^N$, layer thickness Δz, and the refocusing distance Δf.

$\boldsymbol{R}(\boldsymbol{\rho}) \leftarrow |\boldsymbol{U}_{\text{image}}(\boldsymbol{\rho})| - \sqrt{\boldsymbol{I}_{\text{measure}}(\boldsymbol{\rho})}$ ▷ residual

$\boldsymbol{U}^{\dagger}_{\text{image}}(\boldsymbol{\rho}) \leftarrow (\boldsymbol{U}_{\text{image}}(\boldsymbol{\rho})/|\boldsymbol{U}_{\text{image}}(\boldsymbol{\rho})|)\, \boldsymbol{R}(\boldsymbol{\rho})$

$\boldsymbol{U}^{N+1,\dagger}(\boldsymbol{\rho}, (N+1)\Delta z) \leftarrow \mathcal{F}^{-1}\left\{\boldsymbol{P}(\boldsymbol{u})\boldsymbol{K}(\boldsymbol{u}, -\Delta f)\mathcal{F}\left\{\boldsymbol{U}^{\dagger}_{\text{image}}(\boldsymbol{\rho})\right\}\right\}$

for $n \leftarrow N$ to 1 **do** ▷ MLB back-propagation

  $\boldsymbol{U}^{n,\dagger}(\boldsymbol{\rho}, n\Delta z) \leftarrow \mathcal{F}^{-1}\left\{\boldsymbol{K}(\boldsymbol{u}, -\Delta z)\mathcal{F}\left\{\boldsymbol{U}^{n+1,\dagger}(\boldsymbol{\rho}, (n+1)\Delta z)\right\}\right\}$

  $\boldsymbol{Q}^n(\boldsymbol{\rho}, n\Delta z) \leftarrow \mathcal{F}^{-1}\left\{\tilde{\boldsymbol{G}}^*(\boldsymbol{u}, \Delta z)\mathcal{F}\left\{\boldsymbol{U}^{n+1,\dagger}(\boldsymbol{\rho}, (n+1)\Delta z)\right\}\right\}\Delta z$

  $\boldsymbol{V}^n_{\text{grad}}(\boldsymbol{\rho}) \leftarrow \boldsymbol{U}^{n,*}(\boldsymbol{\rho}, n\Delta z)\boldsymbol{Q}^n(\boldsymbol{\rho}, n\Delta z)$

  $\boldsymbol{U}^{n,\dagger}(\boldsymbol{\rho}, n\Delta z) \leftarrow \boldsymbol{U}^{n,\dagger}(\boldsymbol{\rho}, n\Delta z) + \boldsymbol{V}^{n,*}(\boldsymbol{\rho})\boldsymbol{Q}^n(\boldsymbol{\rho}, n\Delta z)$

end for

Return: Gradient at each layer $\{\boldsymbol{V}^n_{\text{grad}}(\boldsymbol{\rho})\}_{n=1}^N$.

at each iteration. Steps to evaluate the gradient are listed in Algorithm 2, where o^* stands for the complex conjugate of o. Typically the algorithm converges faster if $\boldsymbol{V}$ is sequentially updated over different angles of incidence [43, 96, 114], as opposed to summing the gradients computed from all measurements and refining $\boldsymbol{V}$. The penalty function helps regularize the updated $\boldsymbol{V}$ to avoid over-fitting due to high degree of nonlinearity of the model. The following proximal operator is applied after the gradient steps

$$\mathbf{prox}_{\tau\mathcal{R}}(\boldsymbol{V}) = \arg\min_{\boldsymbol{x}} \tau\mathcal{R}(\boldsymbol{x}) + \frac{1}{2}\|\boldsymbol{x} - \boldsymbol{V}\|_2^2 \,. \tag{5.10}$$

In this chapter, TV is used as the penalty function because it has an efficient proximal operator and provides reasonable regularization [47]. Finally, the Nesterov's acceleration method is used at the end of every iteration to further speed up the convergence [115]. In addition, the momentum restarting mechanism [116] is also adopted, which makes the accelerated gradient method stable by preventing it from diverging. Detailed implementation of the 3D intensity-based phase tomography with MLB is summarized in Algorithm 3. Note that MLB also applies to holographic phase tomography with complex field measurements by simply changing the data fidelity term in Eq. (5.9). At the same time, the inverse Algorithm 3 is compatible with other scattering models by switching to their own Algorithms 1–2. In both simulations and experiments, step size α is set within a range from 0.5 to 5 and τ is manually chosen to be around 10^{-2} for the 1st Born, Rytov, and MLB models. In contrast, these two parameters are 2 to 3 orders of magnitude smaller when MS is applied. This is due to the large local Lipschitz constant of the objective function when using MS, in which RI is solved instead of the scattering potential. Based on Algorithms 1–3, the proposed 3D phase imaging framework using MLB is summarized in Fig. 5.1.

Algorithm 3 3D intensity-based phase tomography with MLB

Input: Measured intensities $\{\boldsymbol{I}_{\text{measure,j}}(\boldsymbol{\rho})\}_{j=1}^{N_{\text{LED}}}$, incident fields at the 1st layer $\{\boldsymbol{U}_j^1(\boldsymbol{\rho}, \Delta z)\}_{j=1}^{N_{\text{LED}}}$, layer thickness Δz, refocusing distance Δf, step size α, regularization parameter τ, and max number of iteration N_{iter}.

Initialization: 3D scattering potentials $\{\boldsymbol{V}_1^n(\boldsymbol{\rho})\}_{n=1}^N = \{\boldsymbol{V}_{\text{prox},0}^n(\boldsymbol{\rho})\}_{n=1}^N = 0$ and $t_0 = 1$

for $k \leftarrow 1$ to N_{iter} **do**
  for $j \leftarrow 1$ to N_{LED} **do** ▷ sequential gradient descent
    $\left(\boldsymbol{U}_{\text{image},j}(\boldsymbol{\rho}), \{\boldsymbol{U}_j^n(\boldsymbol{\rho}, n\Delta z)\}_{n=1}^N\right) \leftarrow$ run Algorithm 1
    $\{\boldsymbol{V}_{\text{grad}}^n(\boldsymbol{\rho})\}_{n=1}^N \leftarrow$ run Algorithm 2
    $\{\boldsymbol{V}_k^n(\boldsymbol{\rho})\}_{n=1}^N \leftarrow \{\boldsymbol{V}_k^n(\boldsymbol{\rho})\}_{n=1}^N - \alpha\{\boldsymbol{V}_{\text{grad}}^n(\boldsymbol{\rho})\}_{n=1}^N$
  end for
  if $\mathcal{L}(\{\boldsymbol{V}_k^n(\boldsymbol{\rho})\}_{n=1}^N) > \mathcal{L}(\{\boldsymbol{V}_{k-1}^n(\boldsymbol{\rho})\}_{n=1}^N)$ **then** ▷ momentum restart
    $\{\boldsymbol{V}_{k+1}^n(\boldsymbol{\rho})\}_{n=1}^N \leftarrow \{\boldsymbol{V}_{\text{prox},k-1}^n\}_{n=1}^N$
    $t_k \leftarrow 1$
    Start $k+1$ iteration
  end if
  $\{\boldsymbol{V}_{\text{prox},k}^n\}_{n=1}^N \leftarrow \mathbf{prox}_{\tau\mathcal{R}}(\{\boldsymbol{V}_k^n(\boldsymbol{\rho})\}_{n=1}^N)$ ▷ regularization
  $t_k \leftarrow \frac{1}{2}\left(1 + \sqrt{1 + 4t_{k-1}^2}\right)$ ▷ Nesterov's acceleration
  $\{\boldsymbol{V}_{k+1}^n(\boldsymbol{\rho})\}_{n=1}^N \leftarrow \{\boldsymbol{V}_{\text{prox},k}^n(\boldsymbol{\rho})\}_{n=1}^N + \frac{t_{k-1}-1}{t_k}\left(\{\boldsymbol{V}_{\text{prox},k}^n(\boldsymbol{\rho})\}_{n=1}^N - \{\boldsymbol{V}_{\text{prox},k-1}^n(\boldsymbol{\rho})\}_{n=1}^N\right)$
end for

Return: Reconstructed 3D scattering potential $\{\boldsymbol{V}_{N_{\text{iter}}+1}^n(\boldsymbol{\rho})\}_{n=1}^N$.

5.3 Simulation Results

Comparison of scattering models

From Eq. (5.9), notice that a scattering model evaluating accurate amplitude images is required in order to recover quantitative 3D RI. It is especially important for oblique illumination, where the amplitude contains more high spatial frequency information and stronger phase contrast. To analyze the accuracy of common scattering models used in 3D phase imaging, including 1st Born, Rytov, and MS, and the proposed MLB method, the amplitude images of a 3D cell phantom with different methods are simulated. Then, their results are compared with those generated by SEAGLE, which is considered to be the ground truth. The RI of the cell phantom is set large enough such that it is not a weakly scattering object. Specifically, it has a $15 \times 15 \times 7.5\mu m^3$ ellipsoid body, which contains cytoplasm (RI $n = 1.35$), a nucleus ($n = 1.33$), two nucleoli ($n = 1.36$), several small organelles ($n = 1.39$), and a thin plasma membrane ($n = 1.37$) enclosing the body. In addition, the 3D cell phantom is surrounded by medium of $n = 1.33$, resulting in a volume of $450 \times 450 \times 150$ voxels with $0.05\mu m$ resolution. Assuming the illumination wavelength is $0.532\mu m$ and NA of the objec-

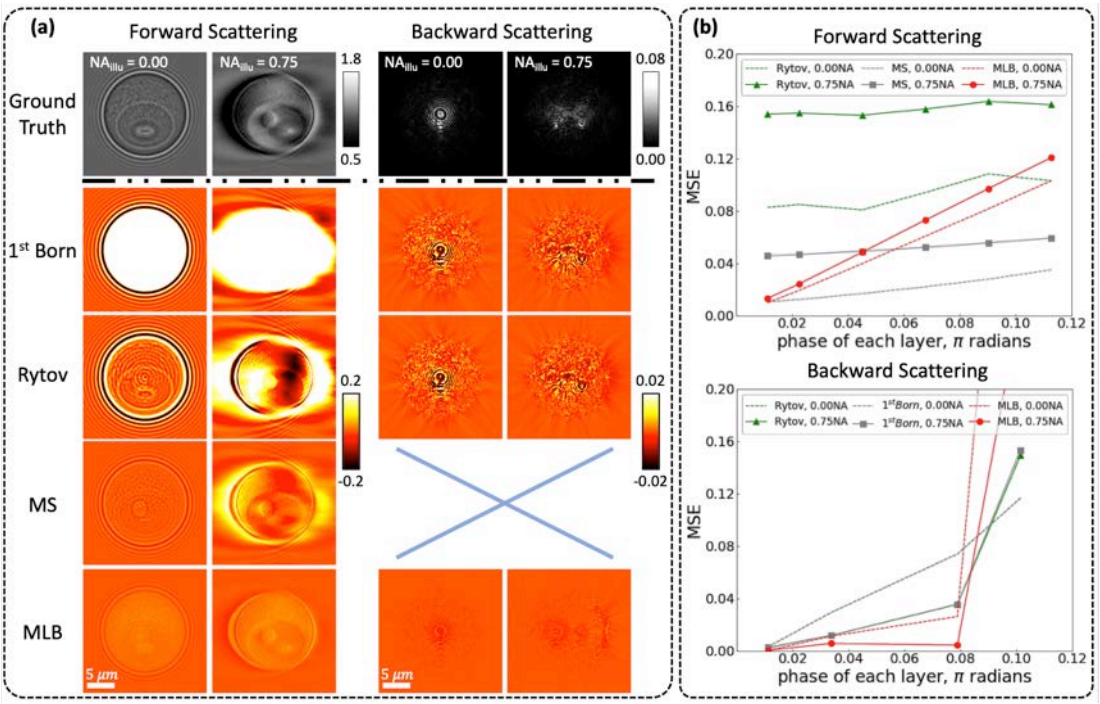

Figure 5.2: Accuracy of image formation with a 3D cell phantom using the 1st Born, Rytov, MS, and MLB scattering models. (a) Ground truth of forward and backward scattered amplitude (first row) with on-axis and off-axis illuminations, and the error maps for all models (bottom rows). (b) Accuracy of each model when the maximum phase within each layer increases.

tive lens is $\mathrm{NA}_{\mathrm{obj}} = 0.8$, the amplitude images are calculated using forward and backward scattered light under on-axis ($\mathrm{NA}_{\mathrm{illu}} = 0.00$) and off-axis ($\mathrm{NA}_{\mathrm{illu}} = 0.75$) illumination scenarios. Ground truth of the amplitudes are shown in the top row of Fig. 5.2(a), while the errors, evaluated by subtracting the ground truths from the amplitudes generated by each model, are listed in the bottom 4 rows. Since the weakly scattering approximation does not hold, both 1st Born and Rytov methods produce high errors in amplitude. In contrast, MS and MLB scattering models account for multiple light scattering within the object, which greatly increase the accuracy. However, the error of MS becomes obvious in the off-axis illumination setting due to paraxial approximation, and the method does not model backward scattering. As a result, MLB is the most accurate model among the four mentioned above. There is a trade-off between the model accuracy and the maximum phase within each layer when using MLB. This is the fact that 1st Born approximation might fail between layers as the phase in each slice becomes too large to satisfy the weak object assumption. Figure 5.2(b) visualizes this trade-off by plotting the evolution of mean squared error (MSE) over the maximum phase value in each layer. By binning the neighboring layers and adapting a larger Δz along z-axis, the maximum phase in each layer is effectively increased. MSE of the 1st Born results

is not displayed because its value is order of magnitude larger than the others. In the forward scattering case, MSE of the MLB results grow linearly when the phase in each layer becomes higher, while the MSEs of Rytov and MS remain similar. Meanwhile, MLB provides more accurate amplitude images in oblique illumination settings when the phase within each layer is smaller than 0.04π for the cell phantom. For backward scattering, MSEs using all models are smaller due to weaker back-scattered light, but the error quickly increases as the phase in each layer grows. Similarly, MLB is expected to have significant accuracy improvement over the others when the weakly scattering assumption is valid within each layer. All the processing was done on a NVIDIA TITAN X GPU installed on a desktop computer (Intel i7-5960X CPU), and the forward computation time of 1st Born, Rytov, MS, and MLB were 0.22, 0.22, 0.25, and 0.32 seconds respectively for the 150-layer phantom.

Comparison of 3D RI reconstructions

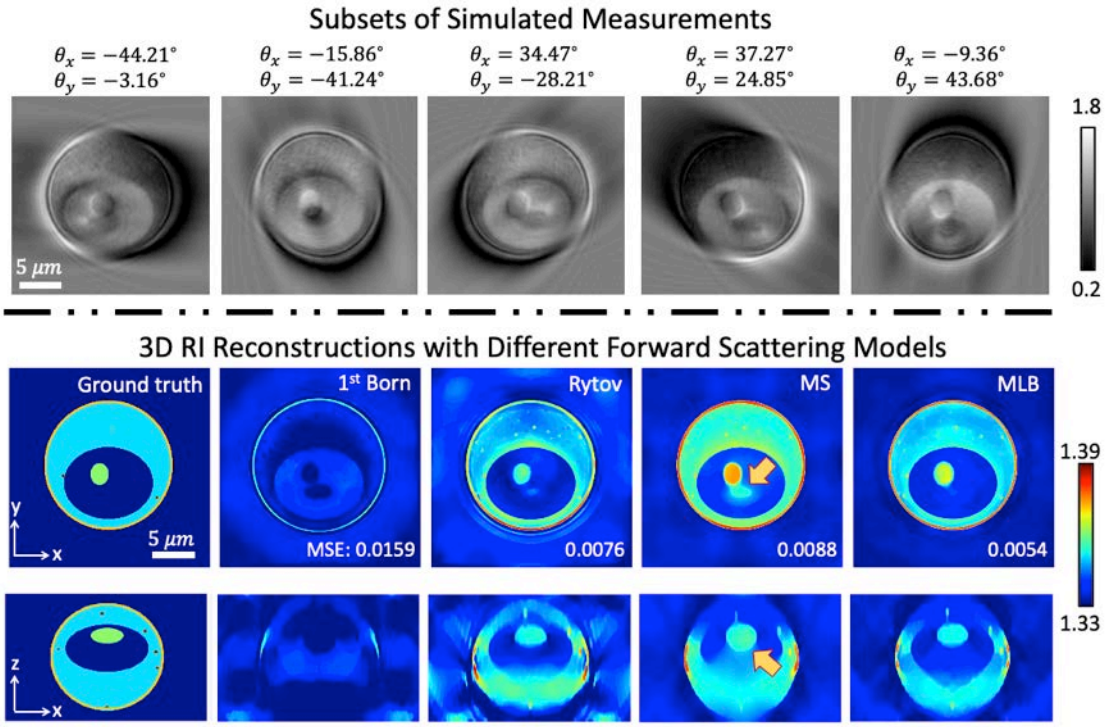

Figure 5.3: Comparison of 3D RI reconstructions using the 1st Born, Rytov, MS, and MLB scattering models and the proposed inverse Algorithm 3. (Top row) Simulated measurements correspond to 5 distinct angles of incidence. (Bottom rows) $x-y$ and $x-z$ cross sections of true RI distribution of the cell phantom as well as the 3D reconstruction results. The MSEs are labeled at the lower right corner of each $x-y$ cross section.

To understand how the accuracy of the forward scattering model used in Algorithm 3 affects 3D RI reconstructions, phase tomography results with 4 different models described in 5.3 are compared. SEAGLE was used to simulate ground truth measurements, where 104 forward scattered amplitudes were generated with illuminations ($NA_{illu} \approx 0.75$) from an annular region on the source plane. And the rest of the imaging parameters, *i.e.* NA, pixel size and wavelength, for image formation simulation remain the same as listed in Sec. 5.3. Similar to Differential Phase Contrast (DPC), measurements contain high spatial frequency contents and rich phase information when the object is illuminated by oblique light with NA_{illu} close to NA_{obj} [32], as shown in the first row of Fig. 5.3. Hence, high resolution 3D RI of the object can be recovered with those measurements. Comparing the ground truth RI of the cell phantom to results computed using different models, obvious differences among them are observed. And the accuracy is quantified by the MSE of each reconstruction, which are 0.0159, 0.0076, 0.0088, and 0.0054 for the 1st Born, Rytov, MS, and MLB methods, respectively. Since 1st Born method overestimate the amplitude values on the image plane (see Fig. 5.2(a)), the RI retrieved using it becomes underestimated. On the other hand, Rytov scattering model results in a more accurate reconstruction due to a less strict approximation. However, it suffers from incorrect background RI, and RI is less uniform inside the object especially on the middle plane of the object ($x - y$ cross section). This suggests that the forward modelling error of Rytov is non-negligible for this multiple-scattering object. In contrast, MS and MLB recover RIs with more uniform background, which are similar to the ground truth. However, the 3D phantom recovered using MS has features elongated in axial direction, which gives rise to a less accurate shape and introduces undesired contrast on the $x - y$ cross section, as indicated in Fig. 5.3. This is also the main reason that MSE with MS is slightly higher than with Rytov model, though the RI reconstruction using MS provide better visual appearance in this simulation. Despite suffering from the missing cone problem as in other cases and sacrificing the axial resolution of low spatial frequency content, the proposed algorithm adopting MLB recovers the most quantitative 3D RI because of the high accuracy of the scattering model. All the computations were performed on the same computer described in 5.3, and the total reconstruction times using Algorithm 3 with 100 iterations were 0.67, 1.19, 1.50 and 1.67 hours, respectively. The computation time grows linearly with the product of number of layers, number of iterations and number of measurements, but barely changes as the number of pixels in each layer increases. This comes from the fact that the most computationally expensive operation in each layer, the FFT, can be efficiently parallelized on a GPU.

5.4 Experimental Results

In the following experiments, an LED array microscope is used to realize the 3D intensity-based phase tomography described in Sec. 5.2. A planar 32×32 programmable LED array is mounted on a Nikon TE300 inverted microscope, which generates $0.514\mu m$ light from different angles of incidence [43]. Since the LEDs are placed far away from the object

compared to the FoV, the incident light from each LED can be treated as a plane wave whose propagating direction is determined by the position of the LED. The distance between the LED array and the object plane is $68mm$ when using the $40\times$, 0.65NA objective lens. And it is adjusted to $46mm$ when the $20\times$, 0.50NA and $60\times$ 0.80NA objective lenses are used for higher illumination intensity and larger angle of incidence. All the images are captured by a monochrome sCMOS camera (PCO.edge 5.5, $6.5\mu m$ pixel size) at the front port of the microscope, where an additional $2\times$ magnification is provided. For each illumination, two intensity images are recorded, with and without the object in the FoV. By dividing the former by the latter, the normalized intensity, $\boldsymbol{I}_{\text{measure}}$, serves as the input when solving the inverse problem in Algorithm 3.

Quantitative comparison between different scattering models

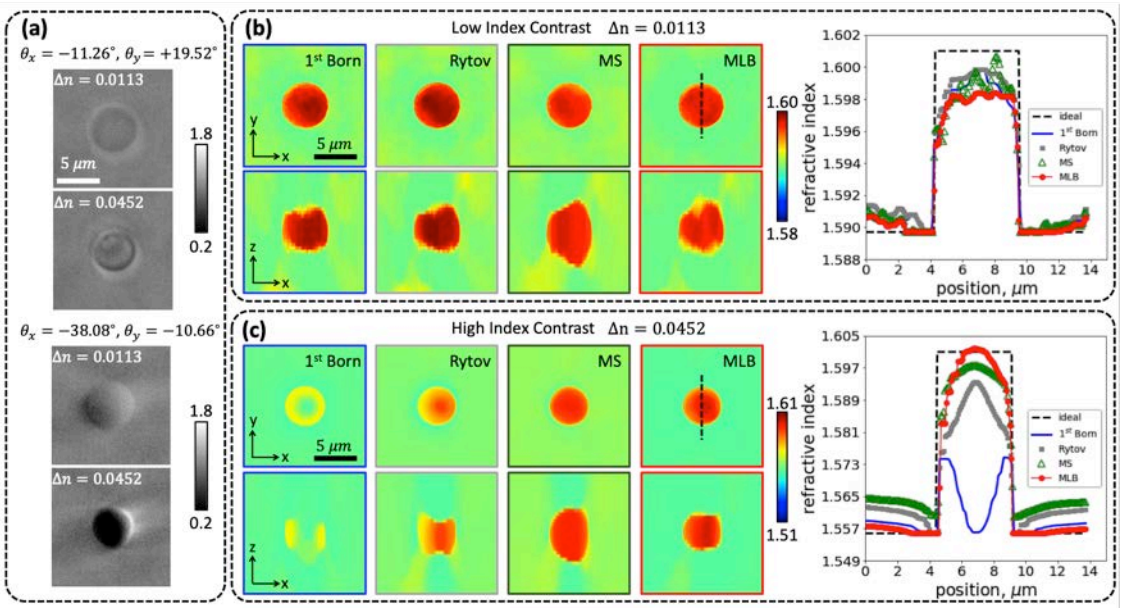

Figure 5.4: Quantitative comparison of recovered RI using different scattering models. (a) Two examples of the normalized transmitted amplitude of both low and high contrast polystyrene beads. (b)–(c) Comparison between orthogonal slices of 3D RI reconstructions of low/high contrast polystyrene beads from different scattering models. 1-D cross sections along the black dotted lines are plotted on the right.

To quantify the accuracy between 3D RI reconstructions from different scattering models in practice, ground truth phantoms are needed. Hence, two $\sim 5\mu m$ polystyrene beads (Sigma-Aldrich, $n = 1.6010$ @$\lambda = 0.514\mu m$) are prepared as the samples by immersing them into two different index-matching oils (Cargille), resulting in RI contrasts of $\Delta n = 0.0113$ and $\Delta n = 0.0452$, respectively. A $40\times$, 0.65 NA objective lens (Nikon CFI Plan

Achromat) was used, whose front focal plane was aligned with the center of the polystyrene beads. 100 images with angles of incidence ranging from 22.77° to 44.09° were captured at 6.66 frame-per-second (FPS) to recover each bead. During the iterative reconstructions, a positivity constraint and TV regularization were incorporated in the proximal step. As shown in Fig. 5.4(b), both single and multiple-scattering models yield similar results as RI contrast is low, since all of them are valid in the weakly scattering regime. In contrast, the recovered RIs drastically changes among different models when the RI contrast increases by a factor of 4, as shown in Fig. 5.4(c). The 1st Born approximation completely fails by underestimating the RI value and missing content in the center region of the bead. Using the Rytov scattering model mitigates the RI underestimation due to less stringent assumptions, but results in a corrupted shape on $x-z$ plane. While reconstructions with MS and MLB methods both accounts for multiple-scattering events, the reconstructed bead using MS has a elongated shape and slightly less quantitative contrast, similar to the simulations. On the other hand, the recovered polystyrene bead using MLB has higher quantitative accuracy and more isotropic resolution. This indicates that MLB best describes the scattering process compared to the other 3 models when imaging objects of high RI contrast.

MLB on weakly scattering object

To see if the proposed algorithm with MLB works with weakly scattering object, we prepare a fixed 3T3 cell as our sample. In this case, a 60×, 0.80 NA objective lens (Nikon CFI Achromat) is used to capture 100 intensity measurements at 2 FPS, and the angles of incidence of LED illuminations were ranging from 49.40° to 51.43°. Since the NA of illuminations is set to be close to the NA of the objective lens, both high frequency content and low frequency phase contrast of the 3D sample are simultaneously encoded in the measurements. This is critical as it is desired to achieve high resolution phase tomography with realistic 3D structure. By using the 60× objective lens, the images formed on the camera plane is over-sampled due to the additional magnification provided by the tube lens at front port. Hence, all the images are down-sampled by a factor of 4 (2 in each dimension) before serving as the inputs of the reconstruction algorithm, which helps reducing the number of unknowns, increasing SNR, and saving computation time. Specifically, the measurements are down-sampled to size 612×612 and set Δz be 5× as large as the demagnified pixel size when solving 3D RI within a $612 \times 612 \times 120$ volume, whose voxel size is $0.108 \times 0.108 \times 0.540 \mu m^3$. In this result, neither the positivity constraint nor TV regularization was used. Figure 5.5(a) shows the orthonormal views of the recovered 3D RI of 3T3 cell. Although the reconstruction suffers from minor anisotropic resolution, the components within the cell can be identified, such as nucleus indicated by the arrows. The physical thickness of the cell is also identified to be $\sim 17 \mu m$. Besides providing quantitative density of the sample, it is also observed that a slice of RI actually provides better contrast compared to conventional 2D phase (contrast) imaging methods. Figure 5.5(c) provides a comparison between DPC using bottom-half circular illumination [30, 32], quantitative phase from DPC with four measurements, and the recovered RI of two regions within the cell at two different depths. While all of them theoretically

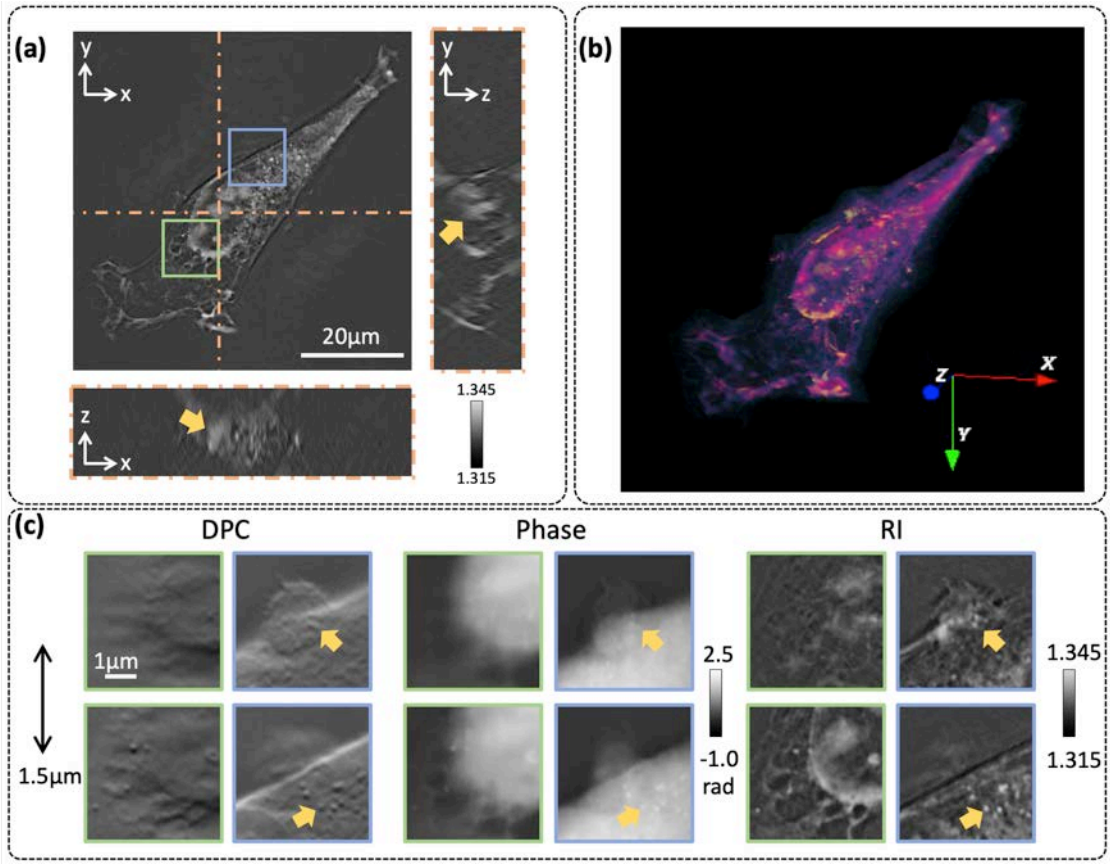

Figure 5.5: 3D RI reconstruction of a 3T3 cell using the MLB scattering model. (a) Orthonormal views of the recovered 3T3 cell. (b) 3D rendering of RI reconstruction. (c) Zoomed-in comparison between DPC, quantitative phase, and slice of 3D RI of the 3T3 cell at two different depths within green and blue boxes in (a).

have similar DoF $\sim 0.64\mu m$, which helps reveal different structures at each plane as those vesicles indicated by the arrows, their contrasts vary dramatically. Out-of-focus information is integrated with in-focus cell content in the phase image, making it hard to distinguish one from the other. Although the DPC images highlight the in-focus components of the cell, it is non-intuitive to interpret the actual structure from the qualitative directional gradient appearance. In contrast, 3D RI reconstruction naturally displays optical density at each depth and builds up high contrast contours that separates distinct organelles.

3D phase imaging of multiple-scattering object

Since MLB model considers multiple-scattering events as opposed to other simplified weakly scattering models, there are improvements in RI reconstructions of an optically thick object when comparing MLB against other models. Here, a 4-cell stage embryo harvested from

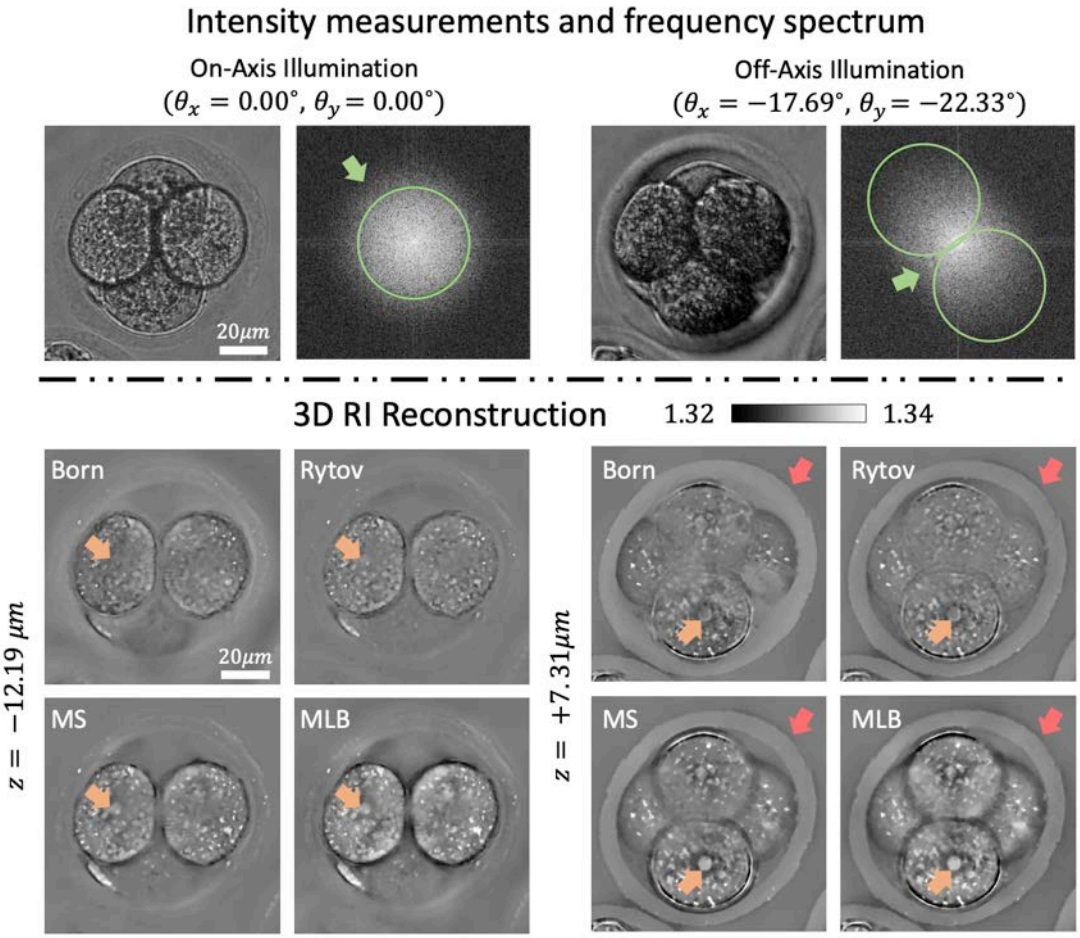

Figure 5.6: (Top) Two examples of measured intensities and their spatial frequency spectrum of a 4-cell stage mouse embryo under the LED array microscope, showing the existence of multiple-scattering event. (Bottom) Two layers of 3D RI reconstruction of a 4-cell stage mouse embryo using the 1st Born, Rytov, MS, and MLB scattering models, respectively.

B6J mice and immersed in KSOM media is imaged, which spans a spherical volume of $\sim 100\mu m$ diameter. The embryo is relatively large and it can drift during the data capture, so a 20×, 0.5NA objective lens is used to trade-off spatial resolution for large FoV, high light throughput, and fast acquisition. With this system adjustment, 132 brightfield images are recorded at 50 FPS to achieve single volume 3D phase tomography within 3s. The first row in Fig. 5.6 shows intensity measurements using on-axis ($\mathrm{NA_{illu}} = 0$) and off-axis ($\mathrm{NA_{illu}} \sim 0.5$) illuminations and their corresponding Fourier spectra. Green circles on the power spectra indicate the spatial frequency coverage of the weak object transfer functions based on the illumination angles [32, 33], in which single scattering signals exist. And some strong signals pointed by green arrows appear outside those regions, indicating that non-

negligible multiple-scattering events happen when light propagates through the embryo. As mentioned in Sec. 5.4, the measurements are down-sampled before sending to Algorithm 3, and the volume of reconstruction is set to be $600 \times 600 \times 50$ voxels, where the voxel size is $0.244 \times 0.244 \times 2.44 \mu m^3$. As a result, 3D RIs of the embryo are recovered with each forward scattering model. The bottom rows in Fig. 5.6 compare RI slices focusing at the lower two cells (aligned horizontally) and the upper two cells (aligned vertically), respectively. When observing the weakly scattering components, *e.g. zona pellucida* (red arrows), both weakly scattering and multiple-scattering methods give rise to similar results. However, obvious differences can be found around the center of the FoV, where the bottom cells are occluded by the top cells. For instance, nucleoli reconstructed using the 1st Born and Rytov approximation either vanish or degrade while the results with MS and MLB provide greater contrast compared to the surrounding cytoplasm, as indicated by the orange arrows. This explains why a multiple-scattering model is necessary for 3D phase tomography with optically dense objects. Here, not much difference between RI results from MS and MLB is observed, since the illumination angles and the objective's NA are both small and paraxial assumption holds in MS propagation. In order to explore the benefit of MLB over MS in reconstructions, high resolution optical microscopes should be used as demonstrated in the next Section.

High resolution 3D phase Imaging of multiple-scattering objects

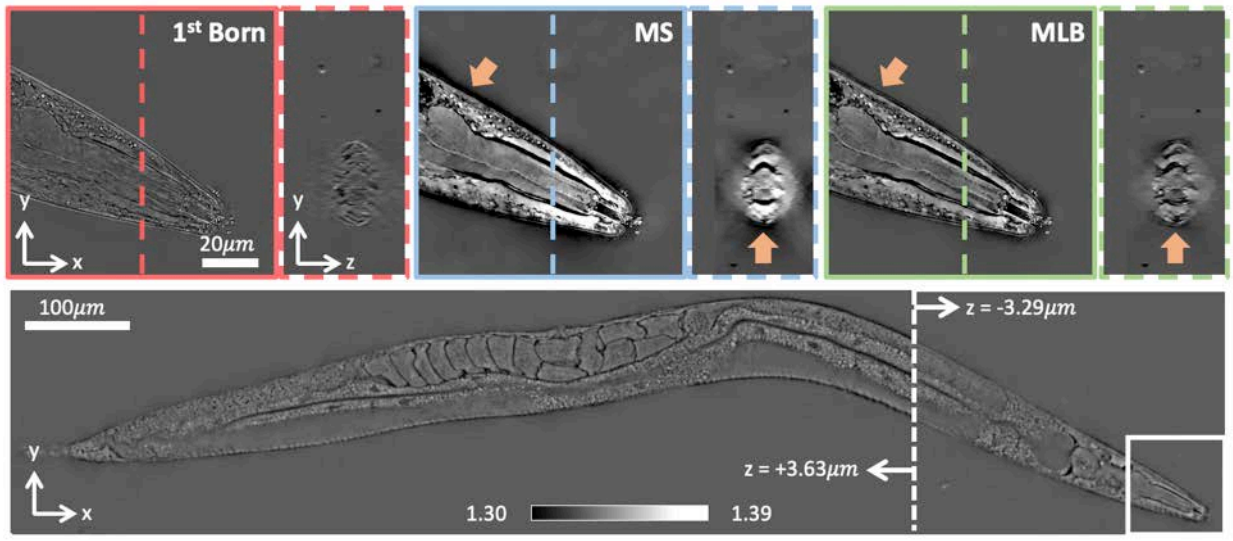

Figure 5.7: 3D RI reconstructions of an entire adult hermaphrodite *C. elegans* worm. The insets show zoomed-in comparison between orthonormal cross-sections of recovered RIs using the 1st Born, MS, and MLB methods, indicated in the white box region that includes the mouth and pharynx of the *C. elegans*.

MLB describes the multiple light scattering process based on scalar wave theory in the object space without any assumptions on the imaging system. Hence, it naturally applies to different microscopic setups in addition the LED array microscopes. Moreover, unlike the Multi-Slice (MS) or beam propagation method, MLB considers non-paraxial wave interaction with 3D objects. To demonstrate these features, the aforementioned intensity-based phase tomography is applied to a custom built high resolution optical microscope [117]. Instead of using an LED array as the light source, a fiber-coupled LED (Thorlabs M530F2, $\lambda = 0.530\mu m$ center wavelength) is combined with a mirror mounted on a motorized kinematic mount (Thorlabs KS1-Z8) to achieve a programmable angle-scanning illumination module. Two high-NA oil-immersion objective lenses (Nikon, CFI Plan Apo Lambda 100×, NA = 1.45) serve as the condenser and the imaging lens respectively, which enables a sub-wavelength resolution phase imaging system. To avoid severe aberrations from steep-angle illuminations, both the illumination and the detection NA are limited up to 1.1 by placing a physical aperture in the pupil plane. A fixed *C. elegans* sandwiched between two coverslips is treated as the multiple-scattering object, and the magnified intensity image corresponds to each illumination is captured by a CMOS camera (FLIR BFS-U3-200S6M). For this specific setup, 120 images are collected with the illumination angles scanned on a spiral-shaped trajectory for 3D RI reconstruction. Since the angle of incidence is mechanically controlled by tilting the mirror, it has lower precision compared to motion-free scanning using the LED array. In order to get robust reconstructions, a self-calibration process is adopted that uses the raw intensity measurements to estimate correct illumination angles computationally [27]. Algorithm 3 can then be applied and provides quantitative RI within a volume of $1200 \times 1200 \times 100$ voxels, whose voxel size is $0.12 \times 0.12 \times 0.35\mu m^3$. However, the length of the *C. elegans* is too long ($\sim 1mm$) to fit in single FoV of the high resolution microscopic system. Therefore, 12 phase tomography dataset at different regions are measured, and the 3D RIs from all FoVs are digitally registered and stitched to visualize the entire worm. In Fig. 5.7, drastic differences between RI results using the 1^{st} Born, MS, and MLB models can be observed. As expected, the RI contrast of body of *C. elegans* is large and the sample is thick so that the weakly scattering approximation fails. Hence, the recovered RI from 1^{st} Born method only shows outlines of the sample but loses most of the low frequency content. Moreover, structures on the $y-z$ cross-section do not look similar to those recovered with multiple-scattering models. On the other hand, the RI values recovered using MS are slightly higher than RIs in the MLB case. This agrees well with the simulation results, where the physical accuracy of the forward scattering models mirrors the accuracy of the final reconstructions. In addition, the unrealistic halo artifacts pointed by the arrows in Fig. 5.7 are mitigated by simply changing the scattering model from MS to MLB. All facts mentioned above support that MLB works with high-NA imaging system. And the intensity-based phase tomography using MLB has superior performance in terms of accuracy as imaging multiple-scattering objects. At the same time, the computation and memory cost of MLB is similar to MS, which is an efficient method to evaluate 3D scattering. As a result, it is possible to achieve 2 Giga-voxels 3D RI retrieval of the whole *C. elegans*, shown at the bottom in Fig. 5.7, on a desktop computer with GPUs.

5.5 Summary

MLB scattering model is introduced, which fundamentally removes the paraxial approximation as used in MS and is able to compute the backward scattering field simultaneously. MLB shows superior accuracy in far-field simulations using multiple-scattering objects compared to widely used 1^{st} Born, Rytov and MS methods. As a result, the 3D RI reconstruction using MLB has better quantitative accuracy and higher fidelity in geometric shape as imaging strongly scattering samples. The LED array microscope has no moving part during data acquisition, which helps achieving fast 3D imaging capability that is only limited to the power of the LEDs or frame rate the of camera. Meanwhile, thanks to moderate computation complexity and highly parallelizable operations, the inverse algorithm with MLB achieves large volume 3D phase imaging in practice. The 3D phase tomography scheme also applies to optical microscopes with high NA and enables nearly isotropic high resolution 3D RI reconstructions. Since MLB provides a computationally efficient way to model the light scattering process, it helps push the limits of existing methods and inspire new optical design to further improve the performance of 3D phase tomography.

Chapter 6

Conclusion and Future Work

In this work, we have proposed several quantitative phase imaging methods in optical microscopes using a computational imaging framework. In conventional microscopes, the phase or refractive index of objects cannot be directly measured and single phase contrast image does not contain enough information for QPI. Hence, we need to modify the optics of the imaging system, design the data acquisition to operate in tandem with programmable modules, and develop a post-processing algorithm to accomplish phase retrieval. However, introducing additional hardware other than existing optics not only increases the cost, but also makes QPI less feasible on conventional microscopes. Moreover, techniques that involve spatial light modulations at the pupil plane might result in artifacts if the system is not perfectly calibrated. In this work, several multidimensional phase reconstruction methods are proposed using purely coded illumination. By replacing the conventional light source with a low-cost programmable LED array, different 2D and 3D QPI schemes are realized on a commercially available microscope. Object movement during data acquisition is minimized thanks to the fast speed of illumination coding via LEDs, which provides descent temporal resolution and enhances the robustness of object reconstruction. The main contributions of this dissertation include a novel coded illumination strategy for real-time QPI, joint phase recovery and high-dimensional pupil aberration calibration in a low-dimensional space, accurate 3D scattering modelling for both weakly and multiple-scattering objects, and efficient algorithms for solving the inverse problems.

In Chapter 2, a real-time QPI method is demonstrated based on DPC microscopy. To further improve the temporal resolution and increase the frame rate, 3 DPC measurements for phase retrieval are captured simultaneously by a RGB camera using color-multiplexing (cDPC). This relies on a coded illumination that splits 3 half-circular source patterns into different color channels, which can be easily generated via a RGB LED array or a color filter insert with broadband light source. Typically, the color camera has wide band Bayer filters on top of its pixels, so we implement a *demosaic* process to extract DPC images from the raw measurement. By solving a least-squares problem, a single-shot reveals 2D quantitative absorption and phase, and camera-limited speed QPI is achieved. In addition, multiple contrasts, such as PhC and DIC, can also be synthesized since they have well-

defined forward models using the phase reconstruction. Hence, cDPC offers multi-contrast high-speed imaging with fast moving objects, *e.g. C. elegans* and floating cells in microfluidic channel.

In Chapter 3, it is shown that a computational method simultaneously solves for the complex field and calibrates spatially-varying aberrations with as less as 4 measurements. While DPC images are not sensitive to system aberrations, intensity measured with spatially coherent illuminations contains rich information of the aberrated point spread function. Therefore, combining both DPC and coherent intensity images enables joint estimation of absorption, phase, and pupil aberrations. If no assumption is applied during aberration recovery, the number of unknowns are comparable to the size of each image, which requires many data to calculate accurate results. However, it is well-known that the aberrations of circular imaging lenses in optical microscopes can be decomposed using Zernike polynomials. In consequence, a few parameters in a low-dimensional space are able to represent the pupil function, which greatly reduces data requirement of the technique. Furthermore, when the aberrations slowly varies across the FoV, the pupil functions and objects at different locations can be resolved in parallel by splitting the FoV into multiple regions with spatially-invariant aberrations.

In Chapter 4, we extend the DPC microscopy to 3D QPI. Since DoF is narrow compared to the thickness of objects when using spatially partial coherent illumination, through-focus DPC images are measured to gather phase contrasts at multiple depths. Similar to 2D DPC QPI, a linear relationship between the scattering potential of the object and the captured intensity stacks is derived based on weakly scattering assumptions. With our proposed analytic 3D linear transfer functions for absorption and phase, the RI of the objects are reconstructed via a 3D deconvolution algorithm. Instead of using Tikhonov regularization, incorporating *a priori* knowledge (*i.e.* piece-wise smoothness and non-negativity constraints) of the objects mitigates halo artifacts and anisotropic resolution due to the missing cone in 3D spatial frequency spectrum. As a result, the quantitative optical density and volumetric structures of biological samples are visualized under the LED array microscope.

In Chapter 5, a computationally efficient and accurate MLB scattering model is proposed for 3D QPI with multiple-scattering objects. The entire volume containing the object of interest is decomposed into cascaded thin 3D slabs, and the incident light sequentially propagates through each layer. Since the phase in each slab is small, the 1st Born scattering stays valid within individual layer and the multiple-scattering phenomenon becomes a series of single scattering process. Unlike beam propagation or MS method, MLB does not make paraxial assumption and improves the quantitative accuracy, especially for oblique illuminations. At the same time, multiple backward scattering light is also modeled. By illuminating the object with spatially coherent plane waves at various angles and capturing the intensity images, 3D phase information can be rapidly recorded. The proposed iterative algorithm is then used to recover 3D RI of multiple-scattering objects. In addition, the 3D QPI framework is compatible to high NA optical microscopes, where it achieves Giga-voxel *C. elegans* reconstruction at sub-wavelength resolution.

While many 2D QPI methods have been explored and optimized, 3D QPI techniques are relatively new and desire both hardware and software solutions to improve performance in

practice. The following are several interesting potential extensions of this work:

- **Isotropic high resolution 3D QPI using back-scattering:** To essentially solve the missing cone problem as described in Sec. 1.2, a sample could be physically rotated to perform phase retrieval at multiple projected views [93, 110]. However, these approaches increase the complexity of imaging systems and are not trivial to apply for every object. An alternative method is to measure the transmitted as well as reflected light simultaneously. In this case, spatial frequency spectrum of the object can be uniformly sampled and 3D QPI with isotropic resolution becomes possible even in the weakly scattering regime. [118, 119]. To completely fill the missing cone in Fourier spectrum and achieve high resolution phase tomography, high NA objective lenses and an accurate forward/backward scattering model, *e.g.* MLB, must be used.

- **Self-calibration algorithm in 3D QPI:** Similar to DPC with aberration correction in Chapter 3, other computational self-calibration methods [26, 76, 27] for 2D QPI using coded illumination have been demonstrated. Since 3D QPI is even more sensitive to modelling errors, system calibration becomes inevitable in order to reconstruct the object with extreme resolution. Precise incident waves and pupil aberrations need to be recovered to get back the accurate quantitative results. This also applies to 3D QPI beyond optical microscopy, such as electron tomography, where it requires tilt angles, lateral and axial displacements, and system aberrations to be well calibrated for 3D reconstructions at atomic scale [120, 121].

- **Data-driven optical system/priors design for 3D QPI:** The illumination patterns used in this work are heuristically designed based on physical intuitions, which might not be optimal for QPI. Since most phase retrieval problems are non-linear and involves iterative reconstruction, the optimal system cannot be determined analytically. Alternatively, physics-based unrolled algorithm has been demonstrated to provide source coding that results in the best performance given a 2D QPI method [122]. While the iterative algorithms solving Eq. (1.3) is viewed as a deep neural network, physical system parameters like angle and intensity distribution of the light source or phase at the pupil plane are learned. With accurate light scattering models that generate phase contrasts measurements of various kinds of objects as the training data, it is possible to design the most efficient optical system for 3D QPI. At the same time, the post-processing algorithms are developed based on existing regularization schemes, which might not be ideal for the objects being imaged. Similarly, priors for specific type of objects can also be learned [123, 124] along with the system parameters and improve the 3D QPI results.

Bibliography

[1] Frits Zernike. "Phase contrast, a new method for the microscopic observation of transparent objects". In: *Physica* 9.10 (Dec. 1942), pp. 686–698.

[2] R. D. Allen, G. B. David, and Nomarski G. "The Zeiss-Nomarski differential interference equipment for transmitted-light microscopy". In: *Z Wiss Mikrosk* 69.193–221 (1969).

[3] Eric Betzig et al. "Imaging Intracellular Fluorescent Proteins at Nanometer Resolution". In: *Science* 313.5793 (2006), pp. 1642–1645. DOI: 10.1126/science.1127344.

[4] Samuel T. Hess, Thanu P.K. Girirajan, and Michael D. Mason. "Ultra-High Resolution Imaging by Fluorescence Photoactivation Localization Microscopy". In: *Biophysical Journal* 91.11 (2006), pp. 4258–4272. DOI: https://doi.org/10.1529/biophysj.106.091116.

[5] Michael J Rust, Mark Bates, and Xiaowei Zhuang. "Sub-diffraction-limit imaging by stochastic optical reconstruction microscopy (STORM)". In: *Nature Methods* 3 (Aug. 2006), pp. 793–795.

[6] M. G. L. Gustafsson. "Surpassing the lateral resolution limit by a factor of two using structured illumination microscopy". In: *Journal of Microscopy* 198.2 (2000), pp. 82–87. DOI: 10.1046/j.1365-2818.2000.00710.x.

[7] Marc Levoy et al. "Light Field Microscopy". In: *ACM Trans. Graph.* 25.3 (July 2006), pp. 924–934. DOI: 10.1145/1141911.1141976.

[8] Robert Hooke, James Allestry, and John Martyn. *Micrographia, or, Some physiological descriptions of minute bodies made by magnifying glasses :with observations and inquiries thereupon.* London :Printed by Jo. Martyn and Ja. Allestry, printers to the Royal Society ... , 1665, p. 323.

[9] Joseph W Goodman. "Introduction to Fourier optics". In: *Introduction to Fourier optics, 3rd ed., by JW Goodman. Englewood, CO: Roberts & Co. Publishers, 2005* 1 (2005).

[10] B. A. Lippmann and Julian Schwinger. "Variational Principles for Scattering Processes. I". In: *Phys. Rev.* 79 (3 Aug. 1950), pp. 469–480. DOI: 10.1103/PhysRev.79.469.

[11] M. Born and E. Wolf. *Principles of Optics: Electromagnetic Theory of Propagation, Interference and Diffraction of Light*. 7th ed. Cambridge University Press, Oct. 1999.

[12] Giang-Nam Nguyen et al. "Computationally efficient scalar nonparaxial modeling of optical wave propagation in the far-field". In: *Appl. Opt.* 53.10 (Apr. 2014), pp. 2196–2205. DOI: 10.1364/AO.53.002196.

[13] Ernst Abbe. "Beiträge zur Theorie des Mikroskops und der mikroskopischen Wahrnehmung". In: *Archiv für mikroskopische Anatomie* 9 (1873), pp. 413–468.

[14] Ichirou Yamaguchi and Tong Zhang. "Phase-shifting digital holography". In: *Opt. Lett.* 22.16 (Aug. 1997), pp. 1268–1270. DOI: 10.1364/OL.22.001268.

[15] Stefan Witte et al. "Short-coherence off-axis holographic phase microscopy of live cell dynamics". In: *Biomed. Opt. Express* 3.9 (Sept. 2012), pp. 2184–2189. DOI: 10.1364/BOE.3.002184.

[16] Michael Teague. "Deterministic phase retrieval: a Green's function solution". In: *J. Opt. Soc. Am.* 73.11 (Nov. 1983), pp. 1434–1441. DOI: 10.1364/JOSA.73.001434.

[17] L. Waller, L. Tian, and G. Barbastathis. "Transport of intensity phase-amplitude imaging with higher order intensity derivatives". In: *Opt. Express* 18.12 (May 2010), pp. 12552–12561.

[18] Zhong Jingshan et al. "Transport of Intensity phase imaging by intensity spectrum fitting of exponentially spaced defocus planes". In: *Opt. Express* 22.9 (May 2014), pp. 10661–10674. DOI: 10.1364/OE.22.010661.

[19] D. Paganin and K. A. Nugent. "Noninterferometric Phase Imaging with Partially Coherent Light". In: *Phys. Rev. Lett.* 80.12 (Mar. 1998), pp. 2586–2589.

[20] Colin J. R. Sheppard. "Defocused transfer function for a partially coherent microscope and application to phase retrieval". In: *J. Opt. Soc. Am. A* 21.5 (May 2004), pp. 828–831. DOI: 10.1364/JOSAA.21.000828.

[21] Zhuo Wang et al. "Spatial light interference microscopy (SLIM)". In: *Opt. Express* 19.2 (Jan. 2011), pp. 1016–1026. DOI: 10.1364/OE.19.001016.

[22] Jonathan C. Petruccelli, Lei Tian, and George Barbastathis. "The transport of intensity equation for optical path length recovery using partially coherent illumination". In: *Opt. Express* 21.12 (June 2013), pp. 14430–14441. DOI: 10.1364/OE.21.014430.

[23] Tomáš Slabý et al. "Off-axis setup taking full advantage of incoherent illumination in coherence-controlled holographic microscope". In: *Opt. Express* 21.12 (June 2013), pp. 14747–14762. DOI: 10.1364/OE.21.014747.

[24] José A Rodrigo Tatiana Alieva. "Rapid Quantitative Phase Imaging for Partially Coherent Light Microscopy". In: *Optics Express* 22.11 (June 2014), pp. 13472–13483.

[25] Guoan Zheng, Roarke Horstmeyer, and Changhuei Yang. "Wide-field, high-resolution Fourier Ptychographic microscopy". In: *Nature Photonics* 7.9 (2013), pp. 739–745.

[26] Xiaoze Ou, Guoan Zheng, and Changhuei Yang. "Embedded pupil function recovery for Fourier ptychographic microscopy". In: *Opt. Express* 22.5 (Mar. 2014), pp. 4960–4972. DOI: 10.1364/OE.22.004960.

[27] Regina Eckert, Zachary F. Phillips, and Laura Waller. "Efficient illumination angle self-calibration in Fourier ptychography". In: *Appl. Opt.* 57.19 (2018), pp. 5434–5442.

[28] Lei Tian et al. "Computational illumination for high-speed *in vitro* Fourier ptychographic microscopy". In: *Optica* 2.10 (2015), pp. 904–911.

[29] DK Hamilton and CJR Sheppard. "Differential phase contrast in scanning optical microscopy". In: *J. Microsc.* 133.1 (Aug. 1984), pp. 27–39.

[30] Shalin B Mehta and Colin JR Sheppard. "Quantitative phase-gradient imaging at high resolution with asymmetric illumination-based differential phase contrast". In: *Opt. Lett.* 34.13 (July 2009), pp. 1924–1926.

[31] Lei Tian, Jingyan Wang, and Laura Waller. "3D differential phase-contrast microscopy with computational illumination using an LED array". In: *Opt. Lett.* 39.5 (Mar. 2014), pp. 1326–1329. DOI: 10.1364/OL.39.001326.

[32] Lei Tian and Laura Waller. "Quantitative differential phase contrast imaging in an LED array microscope". In: *Opt. Express* 23.9 (Apr. 2015), pp. 11394–11403.

[33] Rene A. Claus et al. "Quantitative phase retrieval with arbitrary pupil and illumination". In: *Opt. Express* 23.20 (Oct. 2015), pp. 26672–26682.

[34] P. Cloetens et al. "Holotomography: Quantitative phase tomography with micrometer resolution using hard synchrotron radiation X rays". In: *Appl. Phys. Lett.* 75.19 (1999), pp. 2912–2914. DOI: 10.1063/1.125225.

[35] Yongjin Sung et al. "Optical diffraction tomography for high resolution live cell imaging". In: *Opt. Express* 17.1 (Jan. 2009), pp. 266–277. DOI: 10.1364/OE.17.000266.

[36] Yann Cotte et al. "Marker-free phase nanoscopy". In: *Nature Photon.* 7 (2013), pp. 113–117.

[37] A. Bronnikov. "Theory of quantitative phase-contrast computed tomography". In: *J. Opt. Soc. Am. A* 19.3 (Mar. 2002), pp. 472–480. DOI: 10.1364/JOSAA.19.000472.

[38] Lei Tian et al. "Compressive X-ray phase tomography based on the transport of intensity equation". In: *Opt. Lett.* 38.17 (2013), pp. 3418–3421.

[39] Emil Wolf. "Three-dimensional structure determination of semi-transparent objects from holographic data". In: *Opt. Commun.* 1 (1969), pp. 153–156. ISSN: 0030-4018. DOI: DOI:10.1016/0030-4018(69)90052-2.

[40] P. P. Ewald. "Introduction to the dynamical theory of X-ray diffraction". In: *Acta Crystallographica Section A* 25.1 (Jan. 1969), pp. 103–108.

[41] KyeoReh Lee et al. "Time-multiplexed structured illumination using a DMD for optical diffraction tomography". In: *Opt. Lett.* 42.5 (2017), pp. 999–1002.

[42] Greg Gbur et al. “Spherical-wave intensity diffraction tomography”. In: *J. Opt. Soc. Am. A* 22.2 (Feb. 2005), pp. 230–238. DOI: 10.1364/JOSAA.22.000230.

[43] Lei Tian and Laura Waller. “3D intensity and phase imaging from light field measurements in an LED array microscope”. In: *Optica* 2.2 (Feb. 2015), pp. 104–111. DOI: 10.1364/OPTICA.2.000104.

[44] S Boyd et al. “Distributed Optimization and Statistical Learning via the Alternating Direction Method of Multipliers”. In: *Foundations and Trends in Machine Learning* 3.1 (Dec. 2011), pp. 1–122.

[45] Ken Kreutz-Delgado. “The Complex Gradient Operator and the CR-Calculus”. In: (June 2009).

[46] Neal Parikh and Stephen Boyd. “Proximal Algorithms”. In: *Found. Trends Optim.* 1.3 (Jan. 2014), pp. 127–239. ISSN: 2167-3888. DOI: 10.1561/2400000003.

[47] Amir Beck and Marc Teboulle. “Fast gradient-based algorithms for constrained total variation image denoising and deblurring problems”. In: *IEEE Trans. Image Process.* 18.11 (2009), pp. 2419–2434.

[48] Amir Beck and Marc Teboulle. “A fast iterative shrinkage-thresholding algorithm for linear inverse problems”. In: *SIAM J. Imaging sciences* 2.1 (2009), pp. 183–202.

[49] Guoan Zheng, Christopher Kolner, and Changhuei Yang. “Microscopy refocusing and dark-field imaging by using a simple LED array”. In: *Opt. Lett.* 36.20 (Oct. 2011), pp. 3987–3989. DOI: 10.1364/OL.36.003987.

[50] Ziji Liu et al. “Real-time brightfield, darkfield, and phase contrast imaging in a light-emitting diode array microscope”. In: *J. Biomed. Opt.* 19.10 (Oct. 2014), pp. 106002–106002.

[51] Xiquan Cui, Matthew Lew, and Changhuei Yang. “Quantitative differential interference contrast microscopy based on structured-aperture interference”. In: *Appl. Phys. Lett.* 93 (2008), p. 091113.

[52] Taewoo Kim et al. “White-light diffraction tomography of unlabelled live cells”. In: *Nature Photon.* 8.3 (Mar. 2014), pp. 256–263.

[53] P.H Van Cittert. “Die Wahrscheinliche Schwingungsverteilung in Einer von Einer Lichtquelle Direkt Oder Mittels Einer Linse Beleuchteten Ebene”. In: *Physica* 1.1–6 (1934), pp. 201–210.

[54] Frits Zernike. “The concept of degree of coherence and its application to optical problems”. In: *Physica* 5.8 (1938), pp. 785–795.

[55] Y. Awatsuji, M. Sasada, and T. Kubota. “Parallel quasi-phase-shifting digital holography”. In: *Appl. Phys. Lett.* 85.6 (2004), pp. 1069–1071.

[56] PHASICS S.A. *QUANTITATIVE PHASE MICROSCOPY*. 2009. URL: http://www.phasicscorp.com.

[57] P. Bon et al. *Method and system for structural analysis of an object by measuring the wave front thereof*. US Patent App. 13/500,385. Nov. 2012.

[58] B.E. Allman, K. Nugent, and C. Porter. *An optical system for producing differently focused images*. WO Patent App. PCT/AU2005/000,204. Sept. 2005.

[59] Laura Waller et al. "Phase from chromatic aberrations". In: *Opt. Express* 18.22 (Oct. 2010), pp. 22817–22825. DOI: 10.1364/OE.18.022817.

[60] Vladimir Paramonov et al. "Depth Camera Based on Color-Coded Aperture". In: *2016 IEEE Conference on Computer Vision and Pattern Recognition Workshops (CVPRW)*. June 2016, pp. 910–918.

[61] Chenguang Ma et al. "Motion deblurring with temporally coded illumination in an LED array microscope". In: *Opt. Lett.* 40.10 (May 2015), pp. 2281–2284. DOI: 10.1364/OL.40.002281.

[62] Zachary F. Phillips et al. "Multi-Contrast Imaging and Digital Refocusing on a Mobile Microscope with a Domed LED Array". In: *PLoS ONE* 10.5 (May 2015), pp. 1–13. DOI: 10.1371/journal.pone.0124938.

[63] E. D. Barone-Nugent, A. Barty, and K. A. Nugent. "Quantitative phase-amplitude microscopy I: optical microscopy". In: *Journal of Microscopy* 206.3 (2002), pp. 194–203. ISSN: 1365-2818.

[64] Monson H. Hayes. *Statistical Digital Signal Processing and Modeling*. Wiley, 1996.

[65] David L. Donoho and Michael Elad. "Optimally sparse representation in general (nonorthogonal) dictionaries via ℓ^1 minimization". In: *PNAS* 100.5 (2002), pp. 2197–2202.

[66] Zhong Jingshan et al. "Nonlinear Optimization Algorithm for Partially Coherent Phase Retrieval and Source Recovery". In: *IEEE Trans. Comput. Imaging* (2016).

[67] R. Horstmeyer et al. "Standardizing the resolution claims for coherent microscopy". In: *Nature Photon.* (2016).

[68] Smith. "Microscopic interferometry". In: *Research (London)* 8 (1955), pp. 385–395.

[69] Manuel Guizar-Sicairos and James R Fienup. "Phase retrieval with transverse translation diversity: a nonlinear optimization approach". In: *Optics Express* 16.10 (2008), pp. 7264–7278.

[70] Andrew M Maiden and John M Rodenburg. "An improved ptychographical phase retrieval algorithm for diffractive imaging". In: *Ultramicroscopy* 109.10 (Sept. 2009), pp. 1256–1262.

[71] Ashish Tripathi, Ian McNulty, and Oleg G Shpyrko. "Ptychographic overlap constraint errors and the limits of their numerical recovery using conjugate gradient descent methods". In: *Opt. Express* 22.2 (2014), pp. 1452–1466.

[72] A. M. Maiden, M. J. Humphry, and J. M. Rodenburg. "Ptychographic transmission microscopy in three dimensions using a multi-slice approach". In: *J. Opt. Soc. Am. A* 29.8 (Aug. 2012), pp. 1606–1614. DOI: 10.1364/JOSAA.29.001606.

[73] Jingshan Zhong et al. "Partially coherent phase imaging with simultaneous source recovery". In: *Opt. Express* 6.1 (Dec. 2015), pp. 257–265.

[74] Jingshan Zhong et al. "Nonlinear Optimization Algorithm for Partially Coherent Phase Retrieval and Source Recovery". In: *IEEE Trans. Comput. Imag.* 2.3 (2016), pp. 310–322.

[75] Zichao Bian, Siyuan Dong, and Guoan Zheng. "Adaptive system correction for robust Fourier ptychographic imaging". In: *Opt. Express* 21.26 (Dec. 2013), pp. 32400–32410. DOI: 10.1364/OE.21.032400.

[76] Li-Hao Yeh et al. "Experimental robustness of Fourier ptychography phase retrieval algorithms". In: *Opt. Express* 23.26 (Dec. 2015), pp. 33214–33240. DOI: 10.1364/OE.23.033214.

[77] Liheng Bian et al. "Motion-corrected Fourier ptychography". In: *Biomed. Opt. Express* 7.11 (Nov. 2016), pp. 4543–4553. DOI: 10.1364/BOE.7.004543.

[78] Guy Satat et al. "Object classification through scattering media with deep learning on time resolved measurement". In: *Optics Express* 25.15 (2017), pp. 17466–17479.

[79] Guoan Zheng et al. "Characterization of spatially varying aberrations for wide field-of-view microscopy". In: *Optics express* 21.13 (2013), pp. 15131–15143.

[80] Roarke Horstmeyer et al. "Overlapped Fourier coding for optical aberration removal". In: *Optics Express* 22.20 (2014), pp. 24062–24080.

[81] Jaebum Chung et al. "Wide field-of-view fluorescence image deconvolution with aberration-estimation from Fourier ptychography". In: *Biomed. Opt. Express* 7.2 (2016), pp. 352–368.

[82] Xiaoze Ou et al. "High numerical aperture Fourier ptychography: principle, implementation and characterization". In: *Opt. Express* 23.3 (2015), pp. 3472–3491.

[83] Bechara Kachar. "Asymmetric illumination contrast: a method of image formation for video light microscopy". In: *Science* 227.4688 (1985), pp. 766–768.

[84] Hangwen Lu et al. "Quantitative phase imaging and complex field reconstruction by pupil modulation differential phase contrast". In: *Opt. Express* 24.22 (2016), pp. 25345–25361.

[85] Virendra N. Mahajan. "Zernike Circle Polynomials and Optical Aberrations of Systems with Circular Pupils". In: *Appl. Opt.* 33.34 (1994), pp. 8121–8124.

[86] Zachary F. Phillips, Michael Chen, and Laura Waller. "Single-shot quantitative phase microscopy with color-multiplexed differential phase contrast (cDPC)". In: *PLOS ONE* 12.2 (2017), e0171228.

[87] Dong C. Liu and Jorge Nocedal. "On the limited memory BFGS method for large scale optimization". In: *Mathematical Programming* 45.1 (1989), pp. 503–528.

[88] Guoan Zheng, Roarke Horstmeyer, and Changhuei Yang. "Wide-field, high-resolution Fourier ptychographic microscopy". In: *Nature Photon.* 7.9 (Sept. 2013), pp. 739–745.

[89] Lei Tian et al. "Multiplexed coded illumination for Fourier Ptychography with an LED array microscope". In: *Biomed. Opt. Express* 5.7 (July 2014), pp. 2376–2389. DOI: 10.1364/BOE.5.002376.

[90] N. Streibl. "Three-dimensional imaging by a microscope". In: *J. Opt. Soc. Am. A* 2.2 (Feb. 1985), pp. 121–127.

[91] Yongjin Sung and Colin J. R. Sheppard. "Three-dimensional imaging by partially coherent light under non-paraxial condition". In: *J. Opt. Soc. Am. A* 28.4 (Apr. 2011), pp. 554–559.

[92] Tan H Nguyen et al. "Quantitative phase imaging of weakly scattering objects using partially coherent illumination". In: *Opt. Express* 24.11 (2016), pp. 11683–11693.

[93] Micha H. Jenkins and Thomas K. Gaylord. "Three-dimensional quantitative phase imaging via tomographic deconvolution phase microscopy". In: *Appl. Opt.* 54.31 (Nov. 2015), pp. 9213–9227.

[94] JP Guigay. "Fourier transform analysis of Fresnel diffraction patterns and in-line holograms". In: *Optik* 49.1 (1977), pp. 121–125.

[95] Y. I. Nesterests and T. E. Gureyev. "Partially coherent contrast-transfer-function approximation". In: *J. Opt. Soc. Am. A* 33.4 (2016), pp. 464–474.

[96] Ulugbek S. Kamilov et al. "Learning approach to optical tomography". In: *Optica* 2.6 (June 2015), pp. 517–522.

[97] Wonshik Choi et al. "Tomographic phase microscopy". In: *Nat. Methods* 4.9 (Aug. 2007), pp. 717–719.

[98] S. Jones, M. King, and A. Ward. "Determining the unique refractive index properties of solid polystyrene aerosol using broadband Mie scattering from optically trapped beads". In: *Phys. Chem.* 15 (Oct. 2013), pp. 20735–20741.

[99] Pierre Bon, Benoit Wattellier, and Serge Monneret. "Modeling quantitative phase image formation under tilted illuminations". In: *Opt. Lett.* 37.10 (2012), pp. 1718–1720.

[100] Xichao Ma, Wen Xiao, and Feng Pan. "Optical tomographic reconstruction based on multi-slice wave propagation method". In: *Opt. Express* 25.19 (2017), pp. 22595–22607.

[101] Ulugbek S. Kamilov et al. "A Recursive Born Approach to Nonlinear Inverse Scattering". In: *IEEE Signal Processing Letters* 23.8 (2016), pp. 1052–1056.

[102] A Dubois, K Belkebir, and M Saillard. "Retrieval of inhomogeneous targets from experimental frequency diversity data". In: *Inverse Problems* 21.6 (Nov. 2005), S65–S79. DOI: 10.1088/0266-5611/21/6/s06.

[103] Patrick C Chaumet and Kamal Belkebir. "Three-dimensional reconstruction from real data using a conjugate gradient-coupled dipole method". In: *Inverse Problems* 25.2 (Feb. 2009), p. 024003. DOI: 10.1088/0266-5611/25/2/024003.

[104] Emeric Mudry et al. "Electromagnetic wave imaging of three-dimensional targets using a hybrid iterative inversion method". In: *Inverse Problems* 28.6 (Apr. 2012), p. 065007. DOI: 10.1088/0266-5611/28/6/065007.

[105] Hsiou-Yuan Liu et al. "SEAGLE: Sparsity-Driven Image Reconstruction Under Multiple Scattering". In: *IEEE Trans. Comput. Imag.* 4.1 (2018), pp. 73–86.

[106] Thanh-An Pham et al. "Versatile reconstruction framework for diffraction tomography with intensity measurements and multiple scattering". In: *Opt. Express* 26.3 (2018), pp. 2749–2763.

[107] Ting Zhang et al. "Far-field diffraction microscopy at $\lambda/10$ resolution". In: *Optica* 3.6 (2016), pp. 609–612.

[108] Henry N. Chapman et al. "High-resolution ab initio three-dimensional x-ray diffraction microscopy". In: *J. Opt. Soc. Am. A* 23.5 (2006), pp. 1179–1200.

[109] Martin Dierolf et al. "Ptychographic X-ray computed tomography at the nanoscale". In: *Nature* 467.7314 (2010), pp. 436–439.

[110] Mor Habaza et al. "Tomographic phase microscopy with 180 ° rotation of live cells in suspension by holographic optical tweezers". In: *Opt. Lett.* 40.8 (Apr. 2015), pp. 1881–1884. DOI: 10.1364/OL.40.001881.

[111] Shwetadwip Chowdhury et al. "Refractive index tomography with structured illumination". In: *Optica* 4.5 (May 2017), pp. 537–545. DOI: 10.1364/OPTICA.4.000537.

[112] Chao Zuo et al. "Lensless phase microscopy and diffraction tomography with multi-angle and multi-wavelength illuminations using a LED matrix". In: *Opt. Express* 23.11 (May 2015), pp. 14314–14328.

[113] Roarke Horstmeyer et al. "Diffraction tomography with Fourier ptychography". In: *Optica* 3.8 (2016), pp. 827–835.

[114] H Erdogan and Jeffrey A Fessler. "Ordered subsets algorithms for transmission tomography". In: *Phys. Med. Biol.* 44.11 (1999), pp. 2835–2851.

[115] Yurii Nesterov. "A method of solving a convex programming problem with convergence rate O $(1/k^2)$". In: *Soviet Mathematics Doklady* 27 (1983), pp. 372–376.

[116] Brendan O'Donoghue and Emmanuel Candes. "Adaptive Restart for Accelerated Gradient Schemes". In: *Found. Comput. Math.* 15 (2015), pp. 715–732.

[117] Shwetadwip Chowdhury et al. "High-resolution 3D refractive index reconstruction of multiple-scattering objects from intensity-only measurements". In: *SPIE Photonics West*. 10887–6. 2019.

[118] Shan Shan Kou and Colin J. R. Sheppard. "Imaging in digital holographic microscopy". In: *Opt. Express* 15.21 (Oct. 2007), pp. 13640–13648. DOI: 10.1364/OE.15.013640.

[119] Di Jin et al. "Tomographic phase microscopy: principles and applications in bioimaging". In: *J. Opt. Soc. Am. B* 34.5 (May 2017), B64–B77. DOI: 10.1364/JOSAB.34.000B64.

[120] Yongsoo Yang et al. "Deciphering chemical order/disorder and material properties at the single-atom level". In: *Nature* 542 (Feb. 2017), pp. 75–79.

[121] David Ren et al. *A Practical Reconstruction Method for Three-Dimensional Phase Contrast Atomic Electron Tomography*. 2018. eprint: arXiv:1807.03886.

[122] M. Kellman et al. "Physics-based Learned Design: Optimized Coded-Illumination for Quantitative Phase Imaging". In: *IEEE Transactions on Computational Imaging* (2019), pp. 1–1. ISSN: 2333-9403. DOI: 10.1109/TCI.2019.2905434.

[123] Steven Diamond et al. "Unrolled Optimization with Deep Priors". In: *arXiv:1705.08041 [cs.CV]* (2017), pp. 1–11.

[124] E. Bostan, U. S. Kamilov, and L. Waller. "Learning-Based Image Reconstruction via Parallel Proximal Algorithm". In: *IEEE Signal Processing Letters* 25.7 (July 2018), pp. 989–993. ISSN: 1070-9908. DOI: 10.1109/LSP.2018.2833812.

Appendix

A.1 Derivation of DPC forward model

Any 2D optical field at the sample plane can be written as $\exp(\boldsymbol{\Phi})$. Therefore, the output field passed through the imaging system becomes a convolution between $\exp(\boldsymbol{\Phi})$ and $\boldsymbol{h}$, where $\boldsymbol{h}$ is the point spread function or the inverse Fourier transform of a shifted pupil $\boldsymbol{P}(\boldsymbol{u}+\boldsymbol{u}')$, which depends on illumination angle ($\boldsymbol{u}'$) on 2D spatial frequency coordinate ($\boldsymbol{u}$). Hence, intensity $\boldsymbol{I}$ at the image plane can be expressed as:

$$\boldsymbol{I}(\boldsymbol{\rho},\boldsymbol{u}') = \boldsymbol{S}(\boldsymbol{u}')|e^{\Phi(\boldsymbol{\rho},\boldsymbol{u}')} \otimes_{\mathrm{2D}} h(\boldsymbol{\rho},\boldsymbol{u}')|^2 \ . \tag{7.1}$$

Here, $\otimes_{\mathrm{2D}}$ is 2D convolution operator and $\boldsymbol{S}$ is the intensity of the incident plane wave. Eq. (7.1) can also be represented in an integral form:

$$\boldsymbol{I}(\boldsymbol{\rho},\boldsymbol{u}') = \boldsymbol{S}(\boldsymbol{u}') \iiint e^{\boldsymbol{\Phi}(\boldsymbol{\rho}_1,\boldsymbol{u}')+\boldsymbol{\Phi}^*(\boldsymbol{\rho}_2,\boldsymbol{u}')} \boldsymbol{h}(\boldsymbol{\rho}-\boldsymbol{\rho}_1,\boldsymbol{u}')\boldsymbol{h}^*(\boldsymbol{\rho}-\boldsymbol{\rho}_2,\boldsymbol{u}')\mathrm{d}^2\boldsymbol{\rho}_1\mathrm{d}^2\boldsymbol{\rho}_2 \ . \tag{7.2}$$

When the absorption and phase gradient are small enough, the exponential term in Eq. (7.2) is approximately the same as its first order Taylor series expansion, *i.e.* $\exp(\boldsymbol{x}) \approx 1+\boldsymbol{x}$. As a result, Eq. (7.2) becomes a combination of convolutions and multiplications:

$$\begin{aligned}\boldsymbol{I}(\boldsymbol{\rho},\boldsymbol{u}') =& \boldsymbol{S}(\boldsymbol{u}')\,(1 \otimes_{\mathrm{2D}} \boldsymbol{h}(\boldsymbol{\rho},\boldsymbol{u}'))\,(1 \otimes_{\mathrm{2D}} \boldsymbol{h}^*(\boldsymbol{\rho},\boldsymbol{u}')) + \\ & \boldsymbol{S}(\boldsymbol{u}')\,(\boldsymbol{\Phi}(\boldsymbol{\rho},\boldsymbol{u}') \otimes_{\mathrm{2D}} \boldsymbol{h}(\boldsymbol{\rho},\boldsymbol{u}'))\,(1 \otimes_{\mathrm{2D}} \boldsymbol{h}^*(\boldsymbol{\rho},\boldsymbol{u}')) + \\ & \boldsymbol{S}(\boldsymbol{u}')\,(\boldsymbol{\Phi}^*(\boldsymbol{\rho},\boldsymbol{u}') \otimes_{\mathrm{2D}} \boldsymbol{h}^*(\boldsymbol{\rho},\boldsymbol{u}'))\,(1 \otimes_{\mathrm{2D}} \boldsymbol{h}(\boldsymbol{\rho},\boldsymbol{u}'))\ .\end{aligned} \tag{7.3}$$

Assuming Köhler illumination, the output intensity under partially coherent illumination is an incoherent sum of coherent intensity, *i.e.* an integration of Eq. (7.3) over $\boldsymbol{u}'$. By taking

Fourier transform ($\tilde{\cdot}$) of the final intensity, the spatial frequency spectrum becomes:

$$\begin{aligned}\tilde{\boldsymbol{I}}(\boldsymbol{u}) = &\iint \boldsymbol{S}(\boldsymbol{u}')|\boldsymbol{P}(\boldsymbol{u}')|^2 \mathrm{d}^2\boldsymbol{u}'\boldsymbol{\delta}(\boldsymbol{u})+ \\ &\iint \boldsymbol{S}(\boldsymbol{u}')\left[\tilde{\boldsymbol{\Phi}}(\boldsymbol{u},\boldsymbol{u}')\boldsymbol{P}(\boldsymbol{u}+\boldsymbol{u}') \otimes_{\mathrm{2D}} \boldsymbol{P}^*(-\boldsymbol{u}+\boldsymbol{u}')\boldsymbol{\delta}(\boldsymbol{u})\right]\mathrm{d}^2\boldsymbol{u}'+ \\ &\iint \boldsymbol{S}(\boldsymbol{u}')\left[\tilde{\boldsymbol{\Phi}}^*(-\boldsymbol{u},\boldsymbol{u}')\boldsymbol{P}^*(-\boldsymbol{u}+\boldsymbol{u}') \otimes_{\mathrm{2D}} \boldsymbol{P}(\boldsymbol{u}+\boldsymbol{u}')\boldsymbol{\delta}(\boldsymbol{u})\right]\mathrm{d}^2\boldsymbol{u}' \ .\end{aligned} \tag{7.4}$$

Since Eq. (7.4) satisfies slowly varying phase, $\tilde{\boldsymbol{\Phi}}(\boldsymbol{u},\boldsymbol{u}')$ of 2D samples can be expressed as $-\mathrm{i}\tilde{\boldsymbol{V}}(\boldsymbol{u})/(4\pi(\lambda^{-2}-\|\boldsymbol{u}+\boldsymbol{u}'\|_2^2)^{0.5})$ based on Rytov approximation [11], where $\boldsymbol{V}$ is the scattering potential and λ is the wavelength of light. Let $\tilde{\boldsymbol{\Phi}}(\boldsymbol{u},0) = \tilde{\boldsymbol{\mu}}(\boldsymbol{u}) + \mathrm{i}\tilde{\boldsymbol{\phi}}(\boldsymbol{u})$, and express the spatial frequency of complex phase under different illumination as $\tilde{\boldsymbol{\Phi}}(\boldsymbol{u},\boldsymbol{u}') = \tilde{\boldsymbol{\Phi}}(\boldsymbol{u},0)((\lambda^{-2}-\|\boldsymbol{u}\|_2^2)/(\lambda^{-2}-\|\boldsymbol{u}+\boldsymbol{u}'\|_2^2))^{0.5}$. By substituting this expression of $\boldsymbol{\Phi}(\boldsymbol{u},\boldsymbol{u}')$ into Eq. (7.4), subtracting and divided by the DC term I_{o} (first term in Eq. (7.4)), the spectrum of the normalized intensity $\tilde{\boldsymbol{I}}_{\mathrm{n}}$ is related to the absorption ($\tilde{\boldsymbol{\mu}}$) and phase ($\tilde{\boldsymbol{\phi}}$) by:

$$\begin{aligned}\tilde{\boldsymbol{I}}_{\mathrm{n}}(\boldsymbol{u}) =& \frac{\sqrt{\lambda^{-2}-\|\boldsymbol{u}\|_2^2}}{I_{\mathrm{o}}} \iint \boldsymbol{S}(\boldsymbol{u}')\left[\frac{\boldsymbol{P}(\boldsymbol{u}+\boldsymbol{u}')\boldsymbol{P}^*(\boldsymbol{u}')}{\sqrt{\lambda^{-2}-\|\boldsymbol{u}+\boldsymbol{u}'\|_2^2}} + \frac{\boldsymbol{P}(\boldsymbol{u}')\boldsymbol{P}^*(-\boldsymbol{u}+\boldsymbol{u}')}{\sqrt{\lambda^{-2}-\|-\boldsymbol{u}+\boldsymbol{u}'\|_2^2}}\right]\mathrm{d}^2\boldsymbol{u}'\tilde{\boldsymbol{\mu}}(\boldsymbol{u})+ \\ &\frac{\mathrm{i}\sqrt{\lambda^{-2}-\|\boldsymbol{u}\|_2^2}}{I_{\mathrm{o}}} \iint \boldsymbol{S}(\boldsymbol{u}')\left[\frac{\boldsymbol{P}(\boldsymbol{u}+\boldsymbol{u}')\boldsymbol{P}^*(\boldsymbol{u}')}{\sqrt{\lambda^{-2}-\|\boldsymbol{u}+\boldsymbol{u}'\|_2^2}} - \frac{\boldsymbol{P}(\boldsymbol{u}')\boldsymbol{P}^*(-\boldsymbol{u}+\boldsymbol{u}')}{\sqrt{\lambda^{-2}-\|-\boldsymbol{u}+\boldsymbol{u}'\|_2^2}}\right]\mathrm{d}^2\boldsymbol{u}'\tilde{\boldsymbol{\phi}}(\boldsymbol{u}) \ .\end{aligned} \tag{7.5}$$

If the NA of the objective lens is small, the oblique factors $(\lambda^{-2}-\|\boldsymbol{u}\|_2^2)^{0.5}$, $(\lambda^{-2}-\|-\boldsymbol{u}+\boldsymbol{u}'\|_2^2)^{0.5}$, and $(\lambda^{-2}-\|\boldsymbol{u}+\boldsymbol{u}'\|_2^2)^{0.5}$ in Eq. (7.5) become $1/\lambda$, and the DPC forward model using partially coherent illumination can be written as Eqs. (1.17)-(1.18).

A.2 Modelling backward scattering using MLB

Recall the 1^{st} born approximation in Eq. (5.2), the total field at a given coordinate is the sum of incident field and the scattered field. Similarly, in the MLB model, the back incident field $\boldsymbol{U}_{\mathrm{bi}}^n$ at the n^{th} layer can be expressed in (7.6) as:

$$\boldsymbol{U}_{\mathrm{bi}}^{n-1}(\boldsymbol{\rho},(n-1)\Delta z) = \boldsymbol{U}_{\mathrm{bi}}^{n}(\boldsymbol{\rho},(n-1)\Delta z) + \boldsymbol{U}_{\mathrm{bi,scattered}}^{n}(\boldsymbol{\rho},(n-1)\Delta z) \ . \tag{7.6}$$

When a 3D object is treated as multiple connected layers, the backward scattering field, second term in (7.6), within each layer has two components, as shown in Fig. A.2.1. One comes from the "*forward*" scattering of back incident field in $-z$ direction, denoted by $\boldsymbol{U}_{\mathrm{bi,fs}}^n$, due to the back-scattered light from layers behind. And the other is a portion of incident

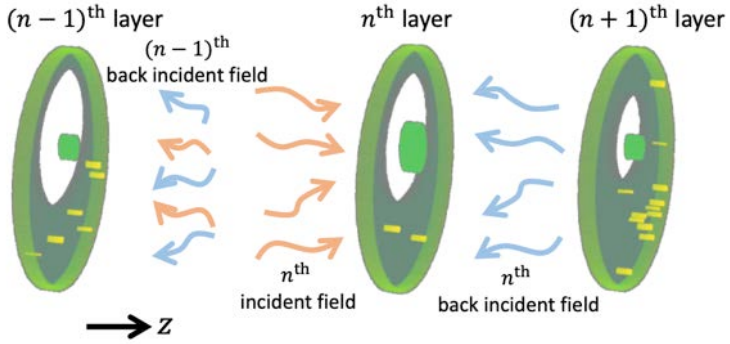

Figure A.2.1: MLB backward scattering model. In each layer, the scattered light from both forward incident field and backward incident field in $-z$ direction serves as the backward incident light to the previous layer.

field reflected, denoted by $\boldsymbol{U}_{\text{bs}}^{n}$, because of the inhomogeneous refractive index (RI) in the layer. In this case, the 1^{st} Born scattering model can be applied in each layer to achieve the backward scattering version of MLB. Then, the recursive relationship of backward scattering field between the layers shown in (7.6) can be expanded to be:

$$\boldsymbol{U}_{\text{bi}}^{n-1}(\boldsymbol{\rho},(n-1)\Delta z)=\boldsymbol{U}_{\text{bi}}^{n}(\boldsymbol{\rho},(n-1)\Delta z)+\boldsymbol{U}_{\text{bi,fs}}^{n}(\boldsymbol{\rho},(n-1)\Delta z)+\boldsymbol{U}_{\text{bs}}^{n}(\boldsymbol{\rho},(n-1)\Delta z), \quad (7.7)$$

Notice that the first two terms on the right hand side of Eq. (7.7) is identical to the forward scattering process described in Eq. (5.3), except with the propagating direction negated. Therefore, only the back-scattered light, $\boldsymbol{U}_{\text{bs}}^{n}$, need to be figured out to complete the backward scattering model of MLB. Based on the 1^{st} Born approximation, the back-scattered field follows the following expression

$$\boldsymbol{U}_{\text{bs}}^{n}(\boldsymbol{\rho},(n-1)\Delta z)=\int_{\frac{-\Delta z}{2}}^{\frac{\Delta z}{2}}\iint \boldsymbol{G}(\boldsymbol{\rho}-\boldsymbol{\rho}',-\Delta z-\zeta)\boldsymbol{U}^{n}(\boldsymbol{\rho}',n\Delta z+\zeta)\boldsymbol{V}(\boldsymbol{\rho}',n\Delta z+\zeta)\mathrm{d}^{2}\boldsymbol{\rho}'\mathrm{d}\zeta\ . \quad (7.8)$$

Note that the only difference between the back-scattered field and the forward-scattered field (Eq. (5.4)) of the incident field is the sign of Δz in Green's function's coordinate. Hence, b using Eq. (7.8) and following the same derivation in Eqs. (1.21)-(5.8), the Fourier transform of $\boldsymbol{U}_{\text{bs}}^{n}$ is obtained

$$\tilde{\boldsymbol{U}}_{\text{bs}}^{n}(\boldsymbol{u})=\tilde{\boldsymbol{G}}(\boldsymbol{u},\Delta z)\iint \operatorname{sinc}\Big(\Big(\boldsymbol{\Gamma}(\boldsymbol{u}')+\boldsymbol{\Gamma}(\boldsymbol{u})\Big)\Delta z\Big)\tilde{\boldsymbol{U}}^{n}(\boldsymbol{u}')\tilde{\boldsymbol{V}}^{n}(\boldsymbol{u}-\boldsymbol{u}')\Delta z\mathrm{d}^{2}\boldsymbol{u}'\ . \quad (7.9)$$

As expected, the difference between Eq. (7.9) and Eq. (5.8) is only a sign change in argument of the sinc function. However, this makes the $\operatorname{sinc}(\boldsymbol{x})\approx 1$ assumption invalid in

Algorithm 4 Multi-Layer Born Backward Scattering

Input: Spectra of incident fields at each layer $\{\tilde{\boldsymbol{U}}^n(\boldsymbol{u})\}_{n=1}^N$ from Algorithm 1, N layers of 3D scattering potential $\{\boldsymbol{V}^n(\boldsymbol{\rho})\}_{n=1}^N$, layer thickness Δz, the refocusing distance Δf, and highest order of Taylor expansion t.

Initialization: Back incident field at N^{th} layer $\boldsymbol{U}_{\text{bi}}^N(\boldsymbol{\rho}, N\Delta z) = 0$

for $n \leftarrow N$ to 1 **do** ▷ MLB scattering

  $\tilde{\boldsymbol{U}}_{\text{bi}}^n(\boldsymbol{\rho}, (n-1)\Delta z) \leftarrow \boldsymbol{K}(\boldsymbol{u}, \Delta z)\mathcal{F}\left\{\boldsymbol{U}_{\text{bi}}^n(\boldsymbol{\rho}, n\Delta z)\right\}$

  $\tilde{\boldsymbol{U}}_{\text{bi,fs}}^n(\boldsymbol{\rho}, (n-1)\Delta z) \leftarrow \tilde{\boldsymbol{G}}(\boldsymbol{u}, \Delta z)\mathcal{F}\left\{\boldsymbol{U}_{\text{bi}}^n(\boldsymbol{\rho}, n\Delta z)\boldsymbol{V}^n(\boldsymbol{\rho})\Delta z\right\}$

  $\tilde{\boldsymbol{U}}_{\text{bs}}^n(\boldsymbol{\rho}, (n-1)\Delta z) \leftarrow 0$

  for $j \leftarrow 0$ to t **do** ▷ Taylor expansion

    $\tilde{\boldsymbol{U}}_{\text{bs}}^n(\boldsymbol{\rho}, (n-1)\Delta z) \leftarrow \tilde{\boldsymbol{U}}_{\text{bs}}^n(\boldsymbol{\rho}, (n-1)\Delta z) + \tilde{\boldsymbol{G}}(\boldsymbol{u}, \Delta z) f_t^j\Big(\boldsymbol{Q}(\boldsymbol{u})\Big)\mathcal{F}\left\{\mathcal{F}^{-1}\left\{\boldsymbol{Q}^j(\boldsymbol{u})\tilde{\boldsymbol{U}}^n(\boldsymbol{u})\right\}\boldsymbol{V}^n(\boldsymbol{\rho})\Delta z\right\}$

  end for

  $\boldsymbol{U}_{\text{bi}}^{n-1}(\boldsymbol{\rho}, (n-1)\Delta z) \leftarrow \mathcal{F}^{-1}\Big\{\tilde{\boldsymbol{U}}_{\text{bi}}^n(\boldsymbol{\rho}, (n-1)\Delta z) + \tilde{\boldsymbol{U}}_{\text{bi,fs}}^n(\boldsymbol{\rho}, (n-1)\Delta z) + \tilde{\boldsymbol{U}}_{\text{bs}}^n(\boldsymbol{\rho}, (n-1)\Delta z)\Big\}$

end for

$\boldsymbol{U}_{\text{image}}(\boldsymbol{\rho}) \leftarrow \mathcal{F}^{-1}\left\{\boldsymbol{P}(\boldsymbol{u})\boldsymbol{K}(\boldsymbol{u}, \Delta f)\mathcal{F}\left\{\boldsymbol{U}_{\text{bi}}^0(\boldsymbol{\rho}, 0)\right\}\right\}$ ▷ refocus and image

Return: Total back-scattered field on the image plane $\boldsymbol{U}_{\text{image}}$.

back scattering evaluation. And the integration in Eq. (7.9) cannot be treated as a convolution, and thus computationally expensive. One way to save the computation burden of MLB backward scattering calculation is approximating the sinc function with polynomials of $\boldsymbol{Q}(\boldsymbol{u}') = \pi\Delta z\boldsymbol{\Gamma}(\boldsymbol{u}')$ and $\boldsymbol{Q}(\boldsymbol{u}) = \pi\Delta z\boldsymbol{\Gamma}(\boldsymbol{u})$ using Taylor expansion up to some order t. Take $t = 2$ as an example, the second order expansion is $\text{sinc}(\boldsymbol{x}) \approx 1 + (\pi\boldsymbol{x})^2/6$, hence,

$$\text{sinc}\Big(\Big(\boldsymbol{Q}(\boldsymbol{u}') + \boldsymbol{Q}(\boldsymbol{u})\Big)/\pi\Big) = 1 + \frac{1}{6}\boldsymbol{Q}^2(\boldsymbol{u}) + \frac{1}{3}\boldsymbol{Q}(\boldsymbol{u})\boldsymbol{Q}(\boldsymbol{u}') + \frac{1}{6}\boldsymbol{Q}^2(\boldsymbol{u}'), \tag{7.10}$$

which can be written in the form

$$\text{sinc}\Big(\Big(\boldsymbol{Q}(\boldsymbol{u}') + \boldsymbol{Q}(\boldsymbol{u})\Big)/\pi\Big) = \sum_{j=0}^{t} f_t^j\Big(\boldsymbol{Q}(\boldsymbol{u})\Big)\boldsymbol{Q}^j(\boldsymbol{u}'), \tag{7.11}$$

where $f_t^j\Big(\boldsymbol{Q}(\boldsymbol{u})\Big)$ is a polynomial in terms of $\boldsymbol{Q}(\boldsymbol{u})$ associated with $\boldsymbol{Q}(\boldsymbol{u}')$ to the j^{th} power in order t Taylor expansion of a sinc function. By substituting Eq. (7.11) into Eq. (7.9), the frequency spectrum of $\boldsymbol{U}_{\text{bs}}^n$ becomes

$$\tilde{\boldsymbol{U}}_{\text{bs}}^n(\boldsymbol{u}) = \sum_{j=0}^{t} \tilde{\boldsymbol{G}}(\boldsymbol{u}, \Delta z) f_t^j\Big(\boldsymbol{Q}(\boldsymbol{u})\Big) \iint \boldsymbol{Q}^j(\boldsymbol{u}')\tilde{\boldsymbol{U}}^n(\boldsymbol{u}')\tilde{\boldsymbol{V}}^n(\boldsymbol{u} - \boldsymbol{u}')\Delta z \mathrm{d}^2\boldsymbol{u}' \ . \tag{7.12}$$

As a result, the backward scattering term can be viewed as a weighted sum of convolutions and be efficiently computed using Fast Fourier Transform (FFT). Starting from the last layer of the object, the back scattering field is accumulated at each layer when light traveling in $-z$ direction. At the end of the recursive process, $\boldsymbol{U}_{\text{bi}}^0(\boldsymbol{\rho}, 0)$ is the total back-scattered field that one is able to measure via an reflective imaging system. Similar to imaging in the forward scattering case, $\boldsymbol{U}_{\text{bi}}^0(\boldsymbol{\rho}, 0)$ is refocused to the imaging plane and passes through the imaging optics with an aperture $\boldsymbol{P}(\boldsymbol{u}) = \text{Circ}(\boldsymbol{u}\lambda/\text{NA})$ in the pupil plane. Based on Eqs. (5.3), (5.8), (7.7) and (7.12), the detailed implementation of backward scattering using MLB is summarized in Algorithm 4. For all backward scattering simulation shown in section 5.3, the order of Taylor expansion is set to be 8, *i.e.* $t = 8$, so that the model is accurate enough compared to the ground truth. Although it is not demonstrated here, implementation of intensity-based phase tomography with backward scattering measurements requires the gradient of $\boldsymbol{U}_{\text{image}}$ with respect to $\{\boldsymbol{V}^n(\boldsymbol{\rho})\}_{n=1}^N$. The analytic gradient can be derived with the same procedure as in the forward scattering case and written in a similar form as Algorithm 2, or it can be evaluated using auto-differentiation packages embedded in machine learning tools, such as TensorFlow and PyTorch.